Atmos. Chem. Phys., 19, 8591–8617, 2019
https://doi.org/10.5194/acp-19-8591-2019


Atmospheric Chemistry and Physics
Open Access
EGU

# Evaluation of global simulations of aerosol particle and cloud condensation nuclei number, with implications for cloud droplet formation

**George S. Fanourgakis[1], Maria Kanakidou[1], Athanasios Nenes[2,3], Susanne E. Bauer[4,5], Tommi Bergman[6], Ken S. Carslaw[7], Alf Grini[8], Douglas S. Hamilton[9], Jill S. Johnson[7], Vlassis A. Karydis[10,11], Alf Kirkevåg[12], John K. Kodros[13], Ulrike Lohmann[14], Gan Luo[15], Risto Makkonen[16,17], Hitoshi Matsui[18], David Neubauer[14], Jeffrey R. Pierce[13], Julia Schmale[19], Philip Stier[20], Kostas Tsigaridis[5,4], Twan van Noije[6], Hailong Wang[21], Duncan Watson-Parris[20], Daniel M. Westervelt[22,4], Yang Yang[21], Masaru Yoshioka[7], Nikos Daskalakis[23], Stefano Decesari[24], Martin Gysel-Beer[19], Nikos Kalivitis[1], Xiaohong Liu[25], Natalie M. Mahowald[9], Stelios Myriokefalitakis[26], Roland Schrödner[27], Maria Sfakianaki[1], Alexandra P. Tsimpidi[10], Mingxuan Wu[25], and Fangqun Yu[15]**

[1]Environmental Chemical Processes Laboratory, Department of Chemistry, University of Crete, Heraklion, 70013, Greece
[2]Laboratory of Atmospheric Processes and their Impacts, School of Architecture, Civil & Environmental Engineering, École Polytechnique Federale de Lausanne, Lausanne, 1015, Switzerland
[3]Institute of Chemical Engineering Sciences, Foundation for Research and Technology (FORTH/ICE-HT), Hellas, 26504, Patras, Greece
[4]NASA Goddard Institute for Space Studies, New York, NY, USA
[5]Center for Climate Systems Research, Columbia University, New York, NY, USA
[6]Royal Netherlands Meteorological Institute (KNMI), De Bilt, the Netherlands
[7]School of Earth and Environment, University of Leeds, UK
[8]independent researcher
[9]Department of Earth and Atmospheric Sciences, Atkinson Center for a Sustainable Future, Cornell University, Ithaca, NY, USA
[10]Department of Atmospheric Chemistry, Max Planck Institute for Chemistry, Mainz, Germany
[11]Forschungszentrum Jülich, Inst Energy & Climate Res IEK-8, 52425 Jülich, Germany
[12]Norwegian Meteorological Institute, Oslo, Norway
[13]Department of Atmospheric Science, Colorado State University, Fort Collins, Colorado, USA
[14]Institute for Atmospheric and Climate Science, ETH Zurich, Zurich, Switzerland
[15]Climate Atmospheric Sciences Research Center , of the State University of New York at Albany, Albany, 12203, New York, USA
[16]Climate System Research, Finnish Meteorological Institute, P.O. Box 503, 00101 Helsinki, Finland
[17]Institute for Atmospheric and Earth System Research/Physics, University of Helsinki, P.O. Box 64, 00014 Helsinki, Finland
[18]Graduate School of Environmental Studies, Nagoya University, Nagoya, Japan
[19]Laboratory of Atmospheric Chemistry, Paul Scherrer Institute, Villigen, Switzerland
[20]Atmospheric, Oceanic & Planetary Physics, Department of Physics, University of Oxford, Oxford OX1 2JD, UK
[21]Atmospheric Sciences and Global Change Division, Pacific Northwest National Laboratory, Richland, Washington, USA
[22]Lamont-Doherty Earth Observatory, Columbia University, Palisades, NY 10964, USA
[23]Laboratory for Modeling and Observation of the Earth System (LAMOS) Institute of Environmental Physics (IUP), University of Bremen, Bremen, Germany
[24]Institute of Atmospheric Sciences and Climate, National Research Council of Italy, Via Piero Gobetti, 101, 40129 Bologna, Italy
[25]Department of Atmospheric Science, University of Wyoming, Laramie, Wyoming, USA

**Published by Copernicus Publications on behalf of the European Geosciences Union.**

[26]Institute for Environmental Research and Sustainable Development (IERSD), National Observatory of Athens, Penteli, Greece
[27]Centre for Environmental and Climate Research, Lund University, Lund, Sweden

**Correspondence:** Maria Kanakidou (mariak@uoc.gr) and Athanasios Nenes (athanasios.nenes@epfl.ch)

Received: 22 December 2018 – Discussion started: 18 January 2019
Revised: 27 April 2019 – Accepted: 24 May 2019 – Published: 8 July 2019

**Abstract.** A total of 16 global chemistry transport models and general circulation models have participated in this study; 14 models have been evaluated with regard to their ability to reproduce the near-surface observed number concentration of aerosol particles and cloud condensation nuclei (CCN), as well as derived cloud droplet number concentration (CDNC). Model results for the period 2011–2015 are compared with aerosol measurements (aerosol particle number, CCN and aerosol particle composition in the submicron fraction) from nine surface stations located in Europe and Japan. The evaluation focuses on the ability of models to simulate the average across time state in diverse environments and on the seasonal and short-term variability in the aerosol properties.

There is no single model that systematically performs best across all environments represented by the observations. Models tend to underestimate the observed aerosol particle and CCN number concentrations, with average normalized mean bias (NMB) of all models and for all stations, where data are available, of $-24\,\%$ and $-35\,\%$ for particles with dry diameters $> 50$ and $> 120$ nm, as well as $-36\,\%$ and $-34\,\%$ for CCN at supersaturations of $0.2\,\%$ and $1.0\,\%$, respectively. However, they seem to behave differently for particles activating at very low supersaturations ($< 0.1\,\%$) than at higher ones. A total of 15 models have been used to produce ensemble annual median distributions of relevant parameters. The model diversity (defined as the ratio of standard deviation to mean) is up to about 3 for simulated $N_3$ (number concentration of particles with dry diameters larger than 3 nm) and up to about 1 for simulated CCN in the extra-polar regions. A global mean reduction of a factor of about 2 is found in the model diversity for CCN at a supersaturation of $0.2\,\%$ ($CCN_{0.2}$) compared to that for $N_3$, maximizing over regions where new particle formation is important.

An additional model has been used to investigate potential causes of model diversity in CCN and bias compared to the observations by performing a perturbed parameter ensemble (PPE) accounting for uncertainties in 26 aerosol-related model input parameters. This PPE suggests that biogenic secondary organic aerosol formation and the hygroscopic properties of the organic material are likely to be the major sources of CCN uncertainty in summer, with dry deposition and cloud processing being dominant in winter.

Models capture the relative amplitude of the seasonal variability of the aerosol particle number concentration for all studied particle sizes with available observations (dry diameters larger than 50, 80 and 120 nm). The short-term persistence time (on the order of a few days) of CCN concentrations, which is a measure of aerosol dynamic behavior in the models, is underestimated on average by the models by 40 % during winter and 20 % in summer.

In contrast to the large spread in simulated aerosol particle and CCN number concentrations, the CDNC derived from simulated CCN spectra is less diverse and in better agreement with CDNC estimates consistently derived from the observations (average NMB $-13\,\%$ and $-22\,\%$ for updraft velocities 0.3 and $0.6\,\mathrm{m\,s^{-1}}$, respectively). In addition, simulated CDNC is in slightly better agreement with observationally derived values at lower than at higher updraft velocities (index of agreement 0.64 vs. 0.65). The reduced spread of CDNC compared to that of CCN is attributed to the sublinear response of CDNC to aerosol particle number variations and the negative correlation between the sensitivities of CDNC to aerosol particle number concentration ($\partial N_\mathrm{d}/\partial N_\mathrm{a}$) and to updraft velocity ($\partial N_\mathrm{d}/\partial w$). Overall, we find that while CCN is controlled by both aerosol particle number and composition, CDNC is sensitive to CCN at low and moderate CCN concentrations and to the updraft velocity when CCN levels are high. Discrepancies are found in sensitivities $\partial N_\mathrm{d}/\partial N_\mathrm{a}$ and $\partial N_\mathrm{d}/\partial w$; models may be predisposed to be too "aerosol sensitive" or "aerosol insensitive" in aerosol–cloud–climate interaction studies, even if they may capture average droplet numbers well. This is a subtle but profound finding that only the sensitivities can clearly reveal and may explain inter-model biases on the aerosol indirect effect.

## 1 Introduction

Aerosol particles absorb and scatter radiation, thereby modulating the planetary radiative balance (Boucher et al., 2013; Myhre et al., 2013). They also provide the nuclei upon which cloud droplets and ice crystals form; variations thereof can profoundly impact cloud formation and precipitation. Both the direct radiative effects of aerosols and their impacts on clouds are thought to be important for climate at global and regional scales, although they are highly uncertain and

confound projections of anthropogenic climate change (e.g., Boucher et al., 2013; Seinfeld et al., 2016). The impacts of aerosols on clouds in particular introduce considerable uncertainty in our estimates of equilibrium climate sensitivity and transient climate response to the combined changes in aerosol and greenhouse gas concentrations (e.g., Seinfeld et al., 2016; Fan et al., 2016).

Aerosols can be either directly emitted from a variety of sources (primary aerosols) or formed by nucleation from precursor compounds (secondary aerosols), which afterwards can grow by condensation and coagulation from a few nanometers to a few hundred nanometers (Kerminen et al., 2012). Note that secondary aerosol also includes the condensed material upon primary emitted aerosol. Aerosols that have the potential to create cloud droplets at atmospherically relevant conditions are termed cloud condensation nuclei (CCN). The CCN number concentration depends on the particle size distribution, chemical composition and mixing state, as well as the level of water vapor supersaturation that develops in rising air parcels (Köhler, 1936; Seinfeld and Pandis, 2006). It is now established that primary emissions of particulate matter and particle formation from anthropogenic precursor gases have strongly modulated clouds and climate at the global scale since the industrial revolution (Boucher et al., 2013). Much work remains, however, to reduce the uncertainty associated with anthropogenic aerosol–cloud–climate interactions.

Among the main sources of uncertainty in simulating aerosol microphysics at regional to global scales are the amounts of particle and precursor vapor mass emitted by anthropogenic activities or natural sources, as well as the size distribution of the emitted particles and their representation in models. However, Mann et al. (2012) showed that a careful choice of the aerosol parameters describing the aerosol distribution can reduce differences between the sectional and the modal description of aerosol microphysics in most parts of the atmosphere. Furthermore, carbonaceous combustion aerosol, although assumed hydrophobic upon emission, was found to contribute up to 64 % of global surface CCN concentrations (Spracklen et al., 2011). Although less important than particle size for CCN formation, particle chemical composition determines aerosol hygroscopicity (Twomey, 1977; Dusek et al., 2006; Petters and Kreidenweis, 2007; Cubison et al., 2008; Bougiatioti et al., 2009). An adequate description of aerosol hygroscopicity is required to accurately describe CCN and cloud droplet number variability. In this respect, uncertainties are partially related to organic aerosol (OA), which can be composed of thousands of compounds with different physical and chemical properties. OA contributes to the fine aerosol mass by up to 30 %–70 % depending on location and season (Kanakidou et al., 2005; Jimenez et al., 2009), while source estimates of OA span 1 order of magnitude (see the AEROCOM phase II intercomparison study of 31 models by Tsigaridis et al., 2014). Regionally, sea salt (SS) and mineral dust (DU) are also significant contributors to the total aerosol particle mass and number concentration. Atmospheric mass loads during the first phase of AEROCOM showed a high diversity among 15 models of 54 % for SS and 40 % for DU (Textor et al., 2006). This diversity arises from the different parameterizations used to calculate the size-resolved fluxes and their dependence on wind speed but also from the consideration, or not, of the supercoarse aerosol fraction (Huneeus et al., 2011; Tsigaridis et al., 2013). Although nitrate ($NO_3^-$) and ammonium ($NH_4^+$) are not explicitly studied here, differences of up to a factor of 13 in the atmospheric burden of $NO_3^-$ and 17 and 4 for $NH_3$ and $NH_4^+$, respectively, have been found between AEROCOM models (Bian et al., 2017).

Formation of new particles by nucleation in the atmosphere is a frequent phenomenon in the free troposphere and in the continental boundary layer (e.g., Kerminen et al., 2010; Kulmala and Kerminen, 2008), and it is an important source of aerosol particle number on a global scale (Kerminen et al., 2012; Kalivitis et al., 2015; Gordon et al., 2017). Although it is well established that sulfuric acid, due to its low volatility, plays a central role in new particle formation and growth, it cannot explain the observed substantial growth of small particles in many environments where organics and $NH_3$ are abundant. This is due to the low concentration of sulfuric acid and is evidenced by the observed poor correlation of its concentration with very small particles (e.g., Pierce et al., 2011). Recently, the involvement of organics from early stages of nucleation and growth of particles has been established (e.g., D'Andrea et al., 2013; Spracklen et al., 2008; Makkonen et al., 2009; Tröstl et al., 2016). Several approaches for modeling particle growth in large-scale models have been developed, which are very sensitive to the volatility of organic vapor (e.g., Laaksonen et al., 2008; Yu, 2011; D'Andrea et al., 2013) and are being implemented in global models.

The number concentration and the size of cloud droplets depend on both the concentrations of CCN and on the cloud updraft velocity (Pruppacher and Klett, 1997; Seinfeld and Pandis, 2006). However, the spatial scale of updrafts governing droplet formation is several orders of magnitude smaller than the size of the grid boxes of global models. Therefore, parameterized aerosol–cloud interactions in climate models require sub-grid-scale vertical velocity distributions to calculate grid-scale relevant cloud droplet number concentration (CDNC) (Morales and Nenes, 2010). Karydis et al. (2012) and Moore et al. (2013) have shown that in regions with low particle number concentrations, such as the Arctic and remote oceans, CDNC is more sensitive to CCN uncertainty than in continental regions where particle number concentrations exceed $10^4\,cm^{-3}$. In contrast, Ervens et al. (2010) pointed out that at high updraft velocities, supersaturation is controlled by adiabatic cooling, and CDNC is not very sensitive to errors in simulated CCN number concentration. They estimated that uncertainties in the chemical composition of aerosol particles that could lead to a doubling of CCN concentration would affect CDNC by only about 10 %–

20 %. Therefore, there are two distinct regimes with regard to CDNC sensitivity: aerosol limited and updraft velocity limited (Reutter et al., 2009).

Totally different cloud radiative (indirect) effects could be computed by climate models depending on the dominance of CDNC sensitivity to either aerosol number or updraft velocity (Sullivan et al., 2016). Therefore, capturing the balance between the two is critical in understanding where and when aerosol emissions are governing the variability of cloud properties and where the updraft velocity is the controlling factor. The failure of state-of-the-art models to capture such sensitivity implies that even if models exhibit a similar magnitude of aerosol indirect effects, it may be for completely different reasons (Sullivan et al., 2016). In this case models would show limited skills and their predictions would be associated with low confidence.

The aims of this work are to (i) assess the accuracy of state-of-the-art global aerosol models in simulating the chemical composition and number concentration of aerosol particles, with a focus on CCN concentrations at various water vapor supersaturation ratios, (ii) document the diversity of the global models in simulating these aerosol properties, (iii) produce an ensemble view of the global distribution of aerosol particle and CCN number concentrations, together with the most important particle chemical components at the Earth's surface, (iv) evaluate the agreement of inferred CDNC from modeled and from observed CCN spectra and their sensitivity to aerosol number concentrations and updraft velocities, (v) evaluate the potential causes of model diversity and bias versus observations using model uncertainty analysis, and (vi) provide recommendations for future model improvements.

A total of 16 global models contributed to this study, and multiyear observations of CCN, size-resolved particle number concentration distributions, and particle chemical composition obtained from eight atmospheric monitoring stations in Europe and one in Japan were used as an observational reference, representing distinct atmospheric environments (Schmale et al., 2017, 2018).

## 2 Methodology

### 2.1 Contributing models and model description

Model setup, such as spatial resolution, meteorological conditions and emission inventories, differs significantly among models (Tables S1 to S4 in the Supplement). The spatial resolution varies among the models from 0.94° by 1.3° to 4° by 5.0° (latitude by longitude) and from 25 to 56 vertical layers up to 10 and even 0.1 hPa. Nine of the models are general circulation models (GCMs) and six are chemical transport models (CTMs). The CTMs use prescribed (and different) meteorological datasets, while the GCMs (with the exception of GISS-E2-TOMAS) are nudged to various reanalysis products. Atmospheric transport, secondary aerosol formation and removal of aerosols are driven by wind, temperature, radiation, precipitation and relative humidity, as well as cloud fraction and liquid water content. In addition, most of the models use wind-driven dust, sea salt and marine organic aerosol emissions as well as calculated online biogenic emissions of non-methane volatile organic compounds (NMVOCs) (Table S3). Therefore, meteorology significantly affects number concentration, composition and other metrics of aerosol particles.

Despite the recognized importance of organic compounds in nucleation (Tröstl et al., 2016), several global models that participated in the present study use the binary homogeneous nucleation of sulfuric acid and water (referred to later as BHN; e.g., Kulmala et al., 1998; Vehkamäki, 2002) and the contribution of organics to particle growth (see Sect. S1 and Table S2 and references therein). GEOS-Chem-TOMAS assumes a ternary nucleation mechanism when $NH_3$ is present and a binary one when $NH_3$ is absent. GEOS-Chem-APM and CAM5-Chem-APM employ a ternary ion-mediated nucleation (TIMN) scheme that considers both binary and ternary as well as ion-mediated and neutral nucleation (Yu et al., 2018). New particle formation in TM5 is calculated as a combination of BHN and organic–sulfuric acid nucleation (Riccobono et al., 2014).

Once in the atmosphere, aerosols undergo transformations through chemical and physical processes, such as coagulation, condensation and evaporation, that modify their size and physical and chemical properties. These aerosol microphysical processes are parameterized differently in models. Eight of the models use modal schemes in which the evolution of particle number and mass concentrations is described by lognormal distributions, and the remaining models use the sectional approach with various numbers of monodisperse size bins describing aerosol particle number concentration and chemical composition (Table S2).

Regarding the eight modal models, six of them (the three ECHAM models, EMAC, TM4-ECPL and TM5) are based on the M7 aerosol module developed by Vignati et al. (2004) for the description of aerosol microphysics or improved versions of M7 to account for $SO_2$ oxidation to sulfuric acid, the contribution of organics to growth and additional aerosol species. Other aerosol microphysics modules used in models participating in this study are the Modal Aerosol Modules (MAM3 and MAM4; Liu et al., 2012, 2016), the Advanced Particle Microphysics (APM) package (Yu and Luo, 2009; Yu, 2011; Yu et al., 2018), the TwO-Moment Aerosol Sectional (TOMAS) microphysics package (Adams and Seinfeld, 2002), the Multiconfiguration Aerosol Tracker of mIXing state (MATRIX) module (e.g., Bauer et al., 2008), the Aerosol Two-dimensional bin module for formation and Aging Simulation version 2 (ATRAS2; Matsui, 2017) and a production-tagged module OsloAero5.3 used in combination with the offline microphysics scheme AeroTab5.3 (Kirkevåg et al., 2018). Tables S1, S2, S3 and S4 provide a summary of

the main features of the participating models and appropriate references.

Relevant to this study are also differences in the aerosol components that are taken into consideration in the models for the CCN calculations. Nine models (CAM5-MAM3, CAM5-MAM4, CAM5.3-Oslo, the three ECHAM models, GEOS-Chem-TOMAS, GISS-E2-TOMAS models and TM4-ECPL) do not account for particulate nitrate at all or in the CCN calculations (Table S2). TM4-ECPL, however, computes the $NO_3^-$ and $NH_4^+$ mass distribution in fine and coarse modes with the ISORROPIA II module (Fountoukis and Nenes, 2007). Similarly, TM5 uses EQSAM (Metzger et al., 2002b, a) to calculate, using a bulk aerosol approach, the partitioning of ammonium nitrate between the gaseous and particulate phase with the particulate mass assumed to reside in the soluble accumulation mode.

Both dry deposition and wet deposition of aerosol particles are taken into account in the participating models as shown in Table S4. For dry deposition, models account for gravitational settling and for turbulence, and thus these processes depend on the aerosol particle size. The omission of super-coarse particle sources associated with dust and sea-salt particles results in discrepancies between models and between model results and observations (Myriokefalitakis et al., 2016). Wet deposition parameterizations account for both in-cloud scavenging, which is sensitive to the solubility of aerosol particles, and below-cloud scavenging by convective and large-scale precipitation (Seinfeld and Pandis, 2006). In addition, while all models account for in-cloud scavenging of aerosols and for aerosol release from the evaporation of droplets, a few models also account for melting and sublimation of ice crystals. For the calculation of CCN concentrations from the aerosol number and mass distributions, models need to specify their hygroscopicity from the volume-weighted hygroscopicities of each constituent (Table 1) following the approach of Petters and Kreidenweis (2007).

Furthermore, most of the participating models (Table S4) follow the AEROCOM recommendation of biomass burning emission heights, which in the boreal regions extend above 2 km and up to 6 km for the Canadian boreal fires (Dentener et al., 2006). ECHAM6-HAM2 and ECHAM6-HAM2-AP use a slightly different vertical distribution of biomass burning emissions, with 75 % within the planetary boundary layer (PBL), 17 % in the first and 8 % in the second level above the PBL (Tegen et al., 2019). EMAC assumes biomass burning emissions at 140 m and GEOS-Chem-APM well mixed in the boundary layer.

In addition to these 15 models, we include the results from perturbed parameter ensemble (PPE) simulations using HadGEM3-UKCA (Yoshioka et al., 2019; see details in Sect. S1). The PPE consists of 235 atmosphere-only simulations for the year 2008 with 26 parameters controlling aerosol emissions and processes perturbed simultaneously. Simulations were nudged to ERA-Interim wind and temperature and all aerosol feedbacks to atmospheric dynamics are turned off. Therefore, all simulations share the same meteorology. CCN number concentrations were calculated globally for all member simulations and taken at geographical locations and elevations of observation stations. These simulations were then used to create Gaussian process emulators at each station location from which 260 000 "model variants" were generated that densely sample the 26-dimension parameter space. The emulator was validated against additional model simulations to show that the emulator uncertainty is much smaller than the model parametric uncertainty.

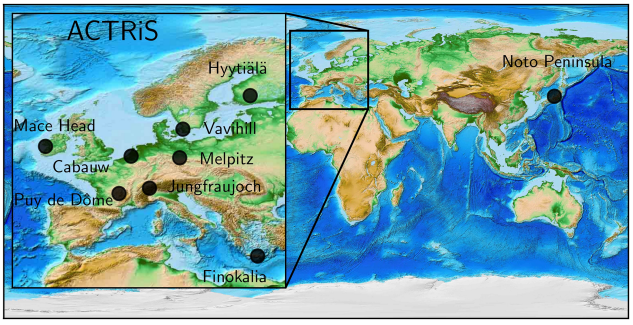


**Figure 1.** Map showing the location of the measurement sites used in this study.

## 2.2 Observational data for model evaluation

Datasets for CCN at various supersaturations, particle number concentrations, size distributions and particle chemical compositions measured at one atmospheric monitoring station in Japan and eight Aerosols, Clouds, and Trace gases Research InfraStructure (ACTRIS) atmospheric monitoring stations in Europe (Schmale et al., 2017) were used in the present study (Fig. 1) for the evaluation of model results. The observatories are representative of different environments (Pacific, Atlantic and Mediterranean marine atmospheres, high alpine and boreal forest continental atmospheres). A brief site description of the observatories is provided in Table S5, while more technical details are given by Schmale et al. (2017). While in general measurement data are available from the period 2011 to 2015, each station covered only a subperiod of those 5 years but at least one entire year (Schmale et al., 2017). Despite using point measurements, the long period of observations allows for the evaluation of global models without biases associated with the model resolution (Schutgens et al., 2016). Six out of the nine stations provided non-refractory chemical composition data on submicron particles (based on aerosol mass spectrometry), while all stations recorded submicron particle number size distributions and CCN number concentrations over a variety of supersaturations. A detailed discussion of the observational results can be found in Schmale et al. (2018).

For this study, the observations of CCN concentrations at supersaturations spanning between 0.1 % and 1.0 %, the

**Table 1.** Hygroscopicity parameters used by the participating models for water uptake calculations.

| Model | SO4 | OA | SS | DU | BC | $NO_3$ |
|---|---|---|---|---|---|---|
| CAM5-Chem-APM | 0.9 | 0.1 | 1.28 | 0 | 0 | 0.9 |
| CAM5-Chem-ATRAS2 | 0.61 | 0.1 | 1.16 | 0.001 | $1 \times 10^{-6}$ | 0.61 |
| CAM5_MAM3 | 0.507 | 0.1 | 1.16 | 0.068 | 0 | N/A |
| CAM5_MAM4 | 0.507 | 0 | 1.16 | 0.068 | | N/A |
| CAM5.3-Oslo | 0.507(1) | 0.14 | 1.2 | 0.069 | $5 \times 10^{-7}$ | N/A |
| ECHAM5.5-HAM2-ELVOC_UH | 0.6 | 0.06 | 1.12 | 0 | | |
| ECHAM6-HAM2(2) | 0.7 | 0 | 1.3 | 0 | 0 | N/A |
| ECHAM6-HAM2-AP(2) | 0.7 | 0 | 1.3 | 0 | 0 | N/A |
| EMAC(3) | | 0.1 | 1.12 | 0 | 0 | N/A |
| GEOS-Chem-APM | 0.9 | 0.1 | 1.28 | 0 | 0 | 0.9 |
| GEOS-Chem-TOMAS | 1.0 | 0.1(4) | 1.2 | 0.01 | 0 | N/A |
| GISS-E2.1-MATRIX | 0.507 | 0.141 | 1.335 | 0.14 | $5 \times 10^{-7}$ | 0.507 |
| GISS-E2-TOMAS | 0.7 | 0.15(5) | 1.3 | 0 | 0 | N/A |
| TM4-ECPL | 0.6 | 0.1 | 1.0 | 0 | 0 | N/A |
| TM5 | 0.6 | 0.1 | 1.0(6) | 0 | 0 | 0.6 |

[1] In CAM5.3-Oslo the hygroscopicity parameters $\kappa$ for pure ammonium sulfate or sulfuric acid are 0.507 and 0.534, respectively. For internal mixtures, $\kappa$ is a mass-weighted average of the aerosol components, except for particles coated (> 2 nm) with SO4, OA and/or SS, where $\kappa$ is a mass-weighted average of the components of the coating (Kirkevåg et al., 2018). [2] ECHAM6-HAM2 and ECHAM6-HAM2-AP use the Abdul-Razzak and Ghan (AR-G) activation scheme (Abdul Razzak and Ghan, 2000). The reported values are approximated using the number of ions and osmotic coefficients used in the AR-G scheme. (3) EMAC model simulates the effective hygroscopicity parameter $\kappa$ of each aerosol size mode in order to describe the influence of chemical composition on the CCN activity of aerosol particles (Pringle et al., 2010). These values are the internally mixed $\kappa$ calculated across the nucleation, Aitken, accumulation and coarse modes. The effective aerosol hygroscopicity parameter $\kappa$ is calculated according to the simple mixing rule proposed by Petters and Kreideweis (2007) using the volume fraction and hygroscopicity parameter of each chemical component (23 salts from ISORROPIA-II and 4 bulk species) taken from Petters et al. (2007) and Sullivan et al. (2009) (4) for hydrophilic OA $\kappa = 0.1$, for hydrophobic OA $\kappa = 0.01$ and (5) for hydrophilic ORG (Lee et al., 2015). For hydrophobic, $\kappa = 0$. (6) for NaCl $\kappa = 1$, for $Na_2SO_4$ $\kappa = 0.95$. N/A: not considered in this study.

number concentrations of aerosols with dry diameters larger than 50, 80 and 120 nm (denoted hereafter as $N_{50}$, $N_{80}$ and $N_{120}$, respectively), and $PM_1$ (particles with dry diameters less than 1 µm) chemical composition (mainly sulfate ($SO_4^{2-}$, hereafter SO4) and organic aerosol – OA) from the nine stations are used. The CCN data for these stations cover at least 75 % of each year (Schmale et al., 2017). Observational data have been further filtered so that there is a minimum data requirement, which means that daily averages are calculated from hourly data only for days with at least six hourly measurements. Monthly averages follow a similar method, whereby the average is calculated only for months with at least 10 daily averages. When fewer data are available, the data are not considered representative of this quantity and are not included in the comparisons with the model results.

### 2.3 Design of the experiment

This model experiment has been designed within the BACCHUS EU project and has been opened for participation to the entire AEROCOM global modeling community. Global simulations have been performed for the years 2010–2015 (2010 is used as a spin-up). SO4, BC, OA, SS and DU are the aerosol components that are considered here. Models provided hourly values for $N_{50}$, $N_{80}$, $N_{120}$ and CCN number concentrations for 13 supersaturations ranging from 0.05 % up to 1.0 % (these are 0.05 %, 0.075 %, 0.1 %, 0.15 % and from 0.2 % to 1.0 % in increments of 0.1 %, denoted hereafter as $CCN_i$, where $i$ is the supersaturation value), as well as the chemical composition of $PM_1$ particles at the station locations (Table S5). The large number of different supersaturations at which CCN are computed allows for direct comparisons with all available observations of CCN for the nine stations as well as for the calculation of CDNC (Sect. 2.4). Among the models that participated in the present study GISS-E2-TOMAS and HadGEM3-UKCA did not provide any results for the stations due to meteorology not corresponding to the measurement time period (free running for the first one and 2008 for the second); therefore, all multimodel medians (MMMs) for the stations presented below have been computed excluding these models.

Beyond station data, the global annual mean surface distribution of $CCN_{0.2}$, the particle numbers $N_3$, $N_{50}$ and $N_{120}$, and the mass composition of the $PM_1$ particles for the year 2011 are provided by 15 models (HadGEM3-UKCA did not provide such results). The MMM has been computed as the median of the contributing models.

In addition to the data provided by the 15 global models, the results of the PPE using HadGEM3-UKCA (Yoshioka et al., 2019) are used in this study to quantify the model parametric uncertainty in CCN and to perform a sensitivity analy-

sis to quantify how each parameter contributes to the overall uncertainty.

### 2.4 Data interpretation methodology

#### 2.4.1 CCN persistence

To investigate the duration for which the CCN number concentration remains similar to its earlier concentration, the so-called persistence, the autocorrelation function (ACF) of the CCN time series, has been calculated as in Schmale et al. (2018) (see also Sect. S2). This ACF may provide valuable information about the drivers of the variability of the CCN number concentration in the atmosphere. In the present study, we chose to compute the ACF based on model results of $CCN_{0.2}$ at the nine sampling sites and compare them with the corresponding ACF obtained from observations (Schmale et al., 2018). For a direct comparison, we use the same time periods as for the observations, which vary among the sampling sites. For all ACF calculations, hourly data on $CCN_{0.2}$ were used for both the observations and model results.

#### 2.4.2 CDNC calculations

While GCMs calculate CDNC using a variety of approaches, for the present study CDNC is calculated offline using a common parameterization for CCN spectra derived from the models or from the observations. This approach allows for an understanding of the importance of differences in modeled and observed CCN spectra by expressing them as differences in CDNC that would form in a given type of cloud. We have calculated CDNC for two different updraft velocities: one characteristic for stratiform clouds ($w = 0.3\,\mathrm{m\,s^{-1}}$) and the second characteristic for cumulus clouds ($w = 0.6\,\mathrm{m\,s^{-1}}$), where $w$ is the width of the vertical velocity distribution assuming a zero mean Gaussian. Similar calculations have been performed using the observed CCN spectra at the stations where such information is available to enable comparison of model results with observations. The ability of the modeled CCN spectra to reproduce the observed sensitivity of CDNC to aerosol or to updraft velocity is also evaluated. Note that evaluation of the differences in CDNC calculations by the different models that are derived from both the parameterizations used and from their input variables would require a different model intercomparison design than here and is planned for the future. Morales Betancourt and Nenes (2014a) provide a good example in which the source of CDNC prediction discrepancy for two state-of-the-art parameterizations in the CAM5 global model was unraveled using adjoint sensitivity analysis. That study pointed to exactly which aspects of the parameterization (i.e., water uptake from large CCN) were not captured adequately, leading to the highly improved droplet parameterizations (Morales-Betancourt and Nenes, 2014b) that were used in the current study.

The calculation of CDNC is based on the parameterization of Nenes and Seinfeld (2003) with the mass transfer augmentations proposed by Fountoukis and Nenes (2005), Barahona and Nenes (2007), and Morales Betancourt and Nenes (2014b). Using the CCN at different supersaturations (Sect. 2.3) allows us to consistently construct the CCN spectrum function $F(s)$ from each simulation, which provides the CCN number as a function of supersaturation, $s$ (Sotiropoulou et al., 2006):

$$F(s) = \frac{N}{1 + \left(\frac{s}{b}\right)^a}, \tag{1}$$

where $N$ is the total number of particles, and $a$ and $b$ are parameters determined using a nonlinear fitting procedure for each of the participating models. $F(s)$ is then computed for each station's grid point and time step of the model outputs (with $b$ and $a$ being fitting parameters), and CDNC, denoted in the figures by $N_\mathrm{d}$, is computed from the parameterization for prescribed values of the vertical velocity. This fitting approach has also been applied to the CCN observations since they are available only for a limited number of supersaturations and thus cannot be directly used for accurate calculation of CDNC. A well-constrained CCN spectrum requires concentrations for at least five different supersaturations at the same time instance (Sotiropoulou et al., 2006). Such information was available only at five stations (Cabauw, Finokalia, Jungfraujoch, Mace Head and Vavihill), which is subsequently used for deriving CDNC based on observations and compared against model-derived CDNC.

The CDNC parameterization uses as input $F(s)$, cloud-base pressure and temperature, and the vertical velocity characterizing the cloud updraft (either as a single updraft or a "characteristic" value that provides a distribution-averaged value; Morales and Nenes, 2010). It determines the value of maximum supersaturation, $s_\mathrm{max}$, that develops in the cloudy updrafts using the concept of "population splitting" (Nenes and Seinfeld, 2003). $s_\mathrm{max}$ is achieved during the cloud parcel ascent and is calculated considering the water vapor balance between its availability from cooling and its loss from condensational growth of the CCN (Fountoukis and Nenes, 2005). CDNC is then obtained from the CCN spectrum as $N_\mathrm{d} = F(s_\mathrm{max})$. This approach works well for stratus and stratocumulus clouds (Morales and Nenes, 2010). CDNC calculated here is from primary activation and does not consider the influence of preexisting droplets, although modifications to the parameterization can account for this as well (e.g., Barahona et al., 2014).

#### 2.4.3 Ensemble modeling computation

The modeled hourly aerosol particle number concentrations, mass composition, CCN and CDNC at the nine stations have been used to calculate daily and monthly averages. Comparison of individual model results with observations is provided in Figs. S2 and S3 because it can be used to iden-

tify the strengths and weaknesses of each specific model and can serve as a guide for model improvements in the future. In Sect. 3, the multi-model median (MMM) is compared to observations. The diversity of the model results (defined as the ratio of standard deviation to mean) and the mean of the models, which in several cases significantly differs from the MMM, are also reported in these comparisons.

Annual averages of the global surface distributions of $N_3$, $N_{50}$, $N_{120}$, $CCN_{0.2}$ and $PM_1$ mass concentrations of the major aerosol components have been provided by a total of 15 models. Global fields have first been re-gridded to a $5^\circ \times 5^\circ$ grid for all models, which is close to the coarsest-resolved participating models ($4^\circ \times 5^\circ$). Then the MMM and diversity are calculated, as described above, for the stations. Note that $5^\circ \times 5^\circ$ is a very coarse grid size, which no doubt affects the model-to-observation comparison, particularly when comparing to sites within small heavily polluted areas where a large rural background is now also being added in and vice versa. Therefore, it is worth mentioning that the surface stations used for model comparison are representative of the larger area in which they are located and justify our choice for a relatively large grid to re-grid all model results. For the mountain stations, the appropriate model level has been considered that corresponds to the station's altitude above sea level. Annual means of the individual models are also presented in Figs. S6–S14.

#### 2.4.4 Performance indexes

For the comparison of model results with observations, a number of statistics variables have been calculated and defined as shown in Sect. S3.2. Hereafter we discuss the following:

the index of agreement

$$\left(\mathrm{IoA} = 1 - \frac{\sum_{i=1}^{N}(P_i - O_i)^2}{\sum_{i=1}^{N}\left(\left|O_i - \overline{O}\right| + \left|P_i - \overline{O}\right|\right)^2}\right),$$

the normalized mean bias

$$\left(\mathrm{NMB} = \frac{\sum_{i=1}^{N}(P_i - O_i)}{\sum_{i=1}^{N} O_i} \times 100\,\%\right)$$

and the normalized mean error

$$\left(\mathrm{NME} = \frac{\sum_{i=1}^{N}|P_i - O_i|}{\sum_{i=1}^{N} O_i} \times 100\,\%\right),$$

where $M$ represents model results, $O$ represents observations, $\overline{O}$ stands for the mean of the observations, and normalized mean bias (NMB), normalized mean error (NME) and the index of agreement (IoA) are used to quantify the performance of the models to reproduce observations. The IoA is a measure of the agreement of model results with the observations. In this study we use all three for the evaluation of the capability of the models to reproduce the observations.

We calculate also

the Pearson linear regression coefficient,

$$\left(r = \left[\frac{\sum_{i=1}^{N}\left(P_i - \overline{P}\right)\left(O_i - \overline{O}\right)}{\sqrt{\sum_{i=1}^{N}\left(P_i - \overline{P}\right)^2}\sqrt{\sum_{i=1}^{N}\left(O_i - \overline{O}\right)^2}}\right]\right),$$

as a measure of the ability of the model results to represent the variability in the observations.

## 3 Evaluation against station observations

### 3.1 CCN number concentration comparisons with multi-model median

The models tend to underestimate the monthly $CCN_{0.2}$ number concentration in the lowest model level at all sites (Figs. 2 and S2) for the years 2011–2015: the average NMB of all models and for the nine sites is as low as −36 %, and the NME is 69 %, while among individual models and stations NMB and NME vary from −88 % to 145 % and from 40 % to 159 %, respectively (see Sect. S3.2 for definitions and Table S6 for results). The Finokalia station is an exception, where most models overestimate $CCN_{0.2}$ (average NMB around 47 %) with eight models showing significant overestimation (NMB > 10 %) and six models smaller deviations from observations (−10 % < NMB < 10 %). Among the studied locations, Finokalia is the station with the highest observed critical diameter (∼ 200 nm at a supersaturation of 0.2 % according to Schmale et al., 2018); therefore, potential inaccuracies in the model determination of the critical size may be responsible for the model overestimate of $CCN_{0.2}$ at this station.

Such a hypothesis is supported by earlier studies that have observed a large size dependence of sensitivity in the activation fraction at low supersaturations and in the size ranges between 60 and 100 nm (Bougiatioti et al., 2011). Deng et al. (2013) reported inferred critical diameters varying by factors of 2–3 for low supersaturations from 0.06 % to 0.2 % and suggested the use of size-resolved particle number concentrations with inferred critical diameters or size-resolved activation ratios to predict CCN. Errors in CCN predictions have been shown to exceed 50 % only at very low supersaturations (Reutter et al., 2009), reaching a factor of 2.4, while at high supersaturations CCN overestimates can be less than 5 % (Ervens et al., 2007). The global near-surface mean CCN prediction error has been estimated at about 9 %, and regionally the maximum error can reach 40 % (Sotiropoulou et al., 2007). The largest CCN prediction error was found in regions with low in-cloud $s_{max}$, like those affected by long-range transport of pollution or industrial pollution plumes. Lower CCN prediction error was found in regions where in-cloud $s_{max}$ is high, which is typical for pristine areas. Sotiropoulou et al. (2007) also found that the assumption of a size-invariant

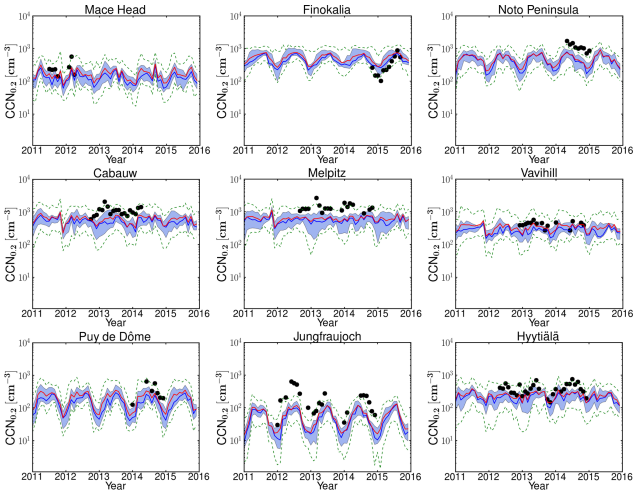


**Figure 2.** Monthly ensembles for the years 2011–2015 of the CCN number concentration for supersaturation 0.2 % ($CCN_{0.2}$). The $CCN_{0.2}$ obtained from observational data is shown with symbols. The continuous bold blue and red lines show the monthly median and mean of all models, respectively. The shaded area shows 25 % and 75 % of the model results, while the green dashed lines show the minimum and maximum values of all models.

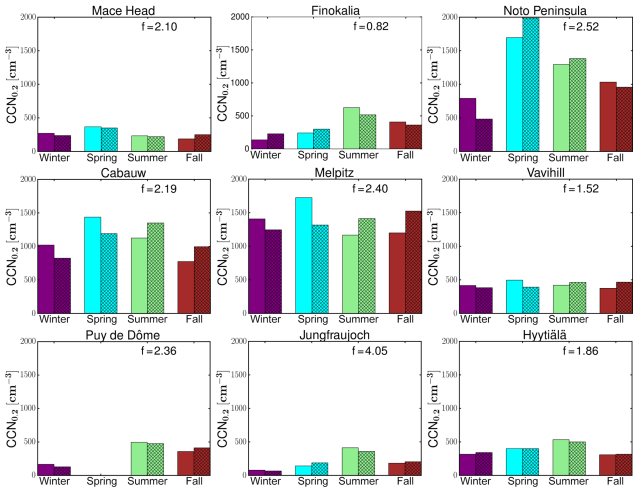


**Figure 3.** Comparison of the seasonal variations of the observed and model median computed $CCN_{0.2}$. The solid bars show the average of the observed $CCN_{0.2}$ during each season and the shaded bars the corresponding averages of the model results. The simulated $CCN_{0.2}$ concentrations have been scaled by a factor, $f$ (denoted in each graph), so that the four-season mean is the same as the observed one. For Puy de Dôme the normalization is based on the mean of three seasons (winter, summer and fall) due to data availability.

chemical composition of internally mixed aerosol increases the error by a factor of 2.

The underestimation of the observed $CCN_{0.2}$ by the models is largest at the high alpine site of Jungfraujoch (mean NMB of all models: −73 %), where none of the models are able to capture the maximum observed values of $CCN_{0.2}$ ($\sim$ 300–600 $cm^{-3}$) during summer. Deficiencies in the models' representation of the boundary layer and mixing of air between the boundary layer and the free troposphere in complex terrain like the Alps, as well as the sampling of the models based on the station's altitude, might be reasons for this systematic underestimation by the models (D'Andrea et al., 2016). Despite the quantitative differences in the estimation of the $CCN_{0.2}$ concentrations, models are able to qualitatively capture the relative differences in $CCN_{0.2}$ concentrations between stations and their seasonal variations. Comparing the $CCN_{0.2}$ as calculated from the observations and as computed from the daily MMM for the days with available observations for the stations, we find a Pearson linear correlation coefficient ($r$) that varies between 0.44 (for Melpitz) and 0.83 (for Mace Head), showing significant covariation of model results with observations. Furthermore, ranking the stations based on the observed mean $CCN_{0.2}$ levels (Fig. S17) we find that the corresponding MMM mean follows this station ranking with the exception of Finokalia where, as further discussed, the models overestimate the observed $CCN_{0.2}$, although they capture ($r = 0.76$) the observed temporal variability well. The MMM index of agreement (IoA) varies between 0.44 and 0.82 for the different stations, with the best for the Finokalia remote coastal station and the worst for the Jungfraujoch alpine station. The largest difference in performance among models is found for the Mace Head station with an IoA varying between 0.20 and 0.89 for the individual models (Table S6).

To compare the calculated MMM and the observed seasonal variability of $CCN_{0.2}$ for each station (Fig. 3), the monthly model results have been temporally co-located with monthly mean observations. Furthermore, to increase clarity in Fig. 3, for each station, the MMM $CCN_{0.2}$ has been multiplied by a scaling factor, $f$, so that the four-season mean of the simulated MMM $CCN_{0.2}$ concentrations becomes equal to the corresponding observed value. The factor $f$ is denoted for each station inside the frame. Overall, the seasonal pattern is nicely captured by the models, although the absolute values are underestimated everywhere ($f > 1.50$) except at Finokalia ($f = 0.82$) as discussed earlier.

For the high-altitude continental background sites (Puy de Dôme, Jungfraujoch) low number concentrations with high seasonal variability are observed (winter (DJF) minimum and summer (JJA) maximum with observed summer-to-winter ratios of 2.17 and 5.37, respectively, while the simulated MMM ratios are 3.19 and 5.58). This strong seasonality is attributed to changes in the height of the boundary layer that can affect these sites during summer but not during winter when the sites are mostly in the free troposphere (Schmale et al., 2018; Jurányi et al., 2011). At Jungfraujoch the boundary layer virtually never reaches up to the site. Instead, increased concentrations are caused by injections of boundary layer air into the lower free troposphere over the mountainous terrain.

The free tropospheric background concentration of CCN is very low such that increases in the number concentration of CCN-sized particles (90 nm in diameter) are a good indicator for boundary layer influence (Herrmann et al., 2015).

On the other hand, high $CCN_{0.2}$ number concentrations but low seasonal variability are found for the rural background stations of Cabauw and Melpitz, indicative of the elevated air pollution background in these regions. At these stations the highest $CCN_{0.2}$ number concentrations are observed during spring, which are underestimated by the MMM. Furthermore, observations show a monotonous decrease from spring to summer and fall, while models calculated higher summertime values than in spring and fall at Cabauw and a monotonous increase from spring to fall at Melpitz. This could indicate that the models are not following the observed changes in the aerosol particle number concentration and/or the critical diameter at these stations (Schmale et al., 2018), possibly also associated with the adopted sizes in the primary aerosol emissions at these locations. At the other rural background station (Vavihill), both models and observations show lower $CCN_{0.2}$ concentrations and seasonal variability than at Cabauw or Melpitz. In addition, observations indicate a higher critical diameter at Vavihill (around 120 nm) than at the other two stations (around 90 nm) (Schmale et al., 2018).

Different seasonal cycles are also observed among the three coastal sites Mace Head, Finokalia and the Noto Peninsula: at the Mace Head site, due to the clean marine conditions over the Atlantic Ocean (Ovadnevaite et al., 2014), low $CCN_{0.2}$ concentrations are observed through the year. There, the highest concentrations are observed and simulated during spring. Both Finokalia and the Noto Peninsula are impacted by long-range transport that occurs through the free troposphere and affects the surface by mixing down into the boundary layer, and the models qualitatively reproduce the observed seasonal cycles, simulating a high variation in the number concentration over the year. At Finokalia the observed and simulated summer seasonal maximum is also attributed to biomass burning plumes from northeastern Europe (Bougiatioti et al., 2016), while high $CCN_{0.2}$ concentrations peaking in spring (observations available only for May) over the Noto Peninsula are due to pollutants originating from East Asia (Iwamoto et al., 2016; Schmale et al., 2018). However, the observed sharp decline of $CCN_{0.2}$ during the spring (May) to summer transition over the Noto Peninsula is also reproduced by the models. At Finokalia the models qualitatively follow the observed seasonality, although the observed summer-to-winter ratio (4.6) is underestimated by the models (2.3; Fig. 3). This can be due to the CCN sensitivity to loss by deposition during winter and to OA formation and hygroscopicity during summer that combined weaken the simulated seasonality (further discussion in Sect. 5).

Finally, at Hyytiälä, on average the models calculate relatively small $CCN_{0.2}$ number concentrations and a low seasonal variability with a maximum in concentrations in summer, in agreement with observations, although they slightly underestimate the observed summer-to-winter ratio (1.5 modeled versus 1.7 observed). As discussed further in Sect. 5, at Hyytiälä the modeled $CCN_{0.2}$ is very sensitive to errors in OA hygroscopicity and in secondary organic aerosol (SOA) formation from biogenic organic precursors during summer. Therefore, uncertainties in OA in the models and in particular underestimates of OA are expected to affect the summer-to-winter ratio.

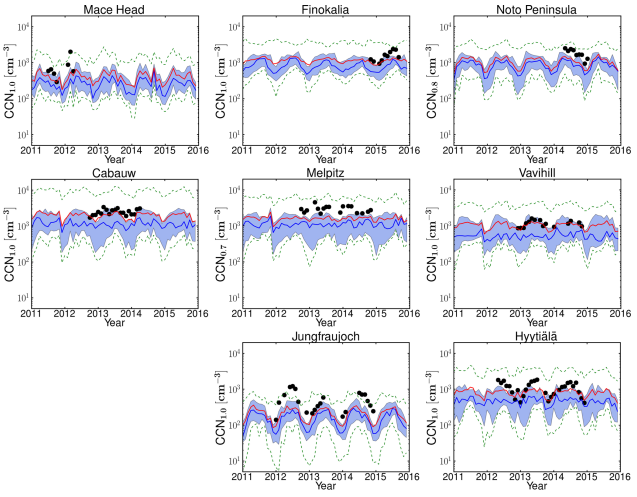


**Figure 4.** Same as Fig. 2 for the CCN at the maximum supersaturation with available measurements at each station. For Puy de Dôme only $CCN_{0.2}$ data are available and are shown in Fig. 2.

Observed CCN number concentrations at the maximum supersaturation ratios measured at each station (which vary among stations, ranging from 0.7 % to 1.0 %) are compared to model results in Fig. 4. CCN at various supersaturation ratios provides insights into the size distribution and the chemical composition in the models, since at high supersaturations smaller and less hygroscopic particles also activate. Most models underestimate CCN at high supersaturation at all stations with available observations (Fig. 4), indicating that an insufficient number of small particles are predicted to activate in the model. However, observations are captured by the maximum and minimum of the 14 models (dashed green line) except for the alpine Jungfraujoch station. Overall, the average NMB and NME of all models and for all stations with available observations are −34 % and 78 %, respectively, while among individual models and stations NMB varies from about −89 % to about 253 % (Table S6).

Comparing model performance for CCN at low supersaturation ($CCN_{0.2}$; Fig. 2) and at high supersaturation ($CCN_{1.0}$; Fig. 4), $CCN_{1.0}$ is systematically underestimated by the models across all stations. The NME of MMM for $CCN_{0.2}$ ranges from 45 % (Finokalia) to 81 % (Jungfraujoch) for the different stations with significant correlation coefficients between 0.44 (Melpitz) and 0.86 (Mace Head), indicating that the MMM model is able to simulate the temporal variability

in the observations. For CCN at the highest supersaturation with available observations the NME varies from 50 % (Finokalia) to 74 % (Mace Head) and the correlation coefficients from 0.37 (Melpitz) to 0.78 (Mace Head) (see also Table S6). These results indicate that $CCN_{0.2}$ is in general better captured than CCN at higher supersaturations, both in absolute values and in temporal variability. Since the number concentration of CCN depends on both the chemical composition and the number of aerosol particles, it is worth investigating the role of these two factors separately.

### 3.2 CCN number concentration comparisons with PPE

$CCN_{0.2}$ concentrations in perturbed parameter ensemble (PPE) simulations using HadGEM3-UKCA (Yoshioka et al., 2019) for 2008 at these stations are shown in Fig. 5, together with observations. The solid blue line shows the mean of the sample of 260 000 model variants that cover the multidimensional uncertainty of the PPE (sampled using an emulator). The blue shading shows the range of 1 standard deviation around the mean, and the dotted lines show the minimum and maximum sampled values. The range of 1 standard deviation either side of the mean value represents approximately 68 % of all samples, and therefore the blue shading shows approximately the same relative range as for the multi-model comparison in Fig. 2 (25 % and 75 % quartiles). The MMM averaged for the years 2011–2015 is also plotted in this figure for comparison purposes together with the 25 % and 75 % quartile shaded area. The means of the available observations from the different years are shown by symbols. Since the interannual variability of simulated MMM $CCN_{0.2}$ concentrations shown in Fig. 2 is generally small compared to inter-model variability, the difference in years between simulations and observations is not considered to undermine the model–data comparisons.

Except for Mace Head, the uncertainty ranges in the PPE are somewhat smaller than the 25 % and 75 % quartiles of the models shown in Fig. 2. This suggests that model structural differences and the emission inventories used in different models are more important sources of diversity of estimated $CCN_{0.2}$ concentrations for the central 70 % range than the fully sampled parametric uncertainty in a single model. However, the maximum–minimum ranges are much larger in the PPE than in the MMM at many locations. Therefore, the values of the sampled model variants from the PPE are more concentrated near the mean but have longer tails on their distribution compared to values from MMM. This is to be expected from such a relatively small sample of models in the MMM.

Model–data comparisons are qualitatively similar to the case with MMM. The PPE simulations underestimate the observed $CCN_{0.2}$ concentrations at many stations and in many months. Exceptions are Puy de Dôme and Hyytiälä where PPE simulations reproduce the observations well for most of the months and Finokalia where, just like MMM, the PPE

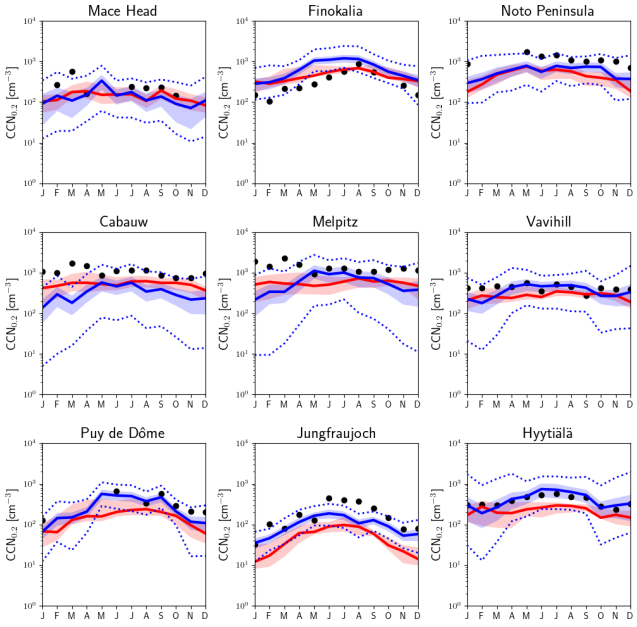


**Figure 5.** Monthly average $CCN_{0.2}$ based on HadGEM3-UKCA perturbed parameter ensemble simulations for the year 2008. The solid blue line shows the mean of the sample of 260 000 model variants from the emulator for each month and station. The shaded blue area shows the range of this mean plus and minus 1 standard deviation, while the blue dashed lines show the minimum and maximum sampled values. The red line shows the MMM results (mean of the years 2011–2015 shown in Fig. 2), and the shaded red area corresponds to the 25 % and 75 % quartiles. The $CCN_{0.2}$ values obtained from observational data are shown by symbols (mean of the available data).

overestimates the observations. At Melpitz and Vavihill simulations capture the observed values in summer but underestimate them in winter and early spring. The PPE simulations fail to capture the observed peaks in winter and early spring at Mace Head and Cabauw as well. This is unlike the case with MMM, which does not show a distinct wintertime underestimate (Fig. 3). The qualitative agreement between PPE and MMM indicates that the perturbed parameters are those with significant control on aerosol processes and emissions and can be used for CCN uncertainty attribution in Sect. 5.

### 3.3 Particle number concentration and $PM_1$ aerosol chemical composition

The observed critical diameter for particle activation into CCN at 0.2 % supersaturation at most of the locations in this study is around 100 nm or larger, reaching about 200 nm in spring and summer at Finokalia (Schmale et al., 2018). Therefore, in Fig. 6, the MMMs of the simulated $N_{50}$ and $N_{120}$ are depicted together with the 25 % and 75 % quartiles of all models that provided station data and are compared with observations. $N_{120}$ is expected to represent a significant portion of the activated particles at 0.2 % or higher super-

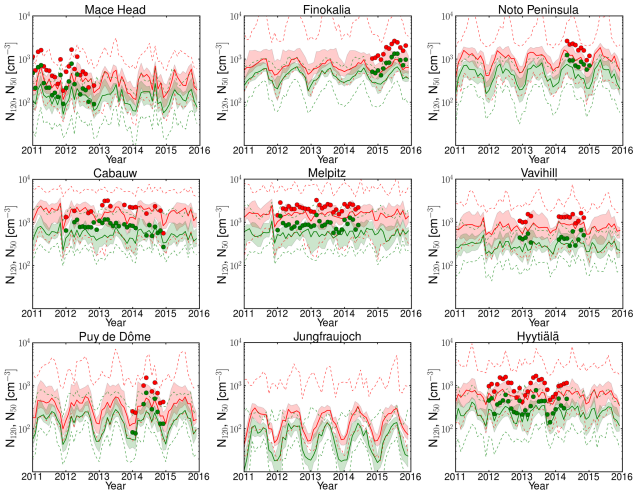


**Figure 6.** Monthly ensembles for the period 2011–2015 of the number concentration of particles with diameters larger than 50 nm ($N_{50}$ – in red) and 120 nm ($N_{120}$ – in green). The continuous lines correspond to the median of the models for each month; the shaded areas show the 25 % and 75 % quartiles and the dashed lines the minimum and maximum of all models for the $N_{50}$ (red area) and $N_{120}$ (green area). Observational data are available for all stations except Jungfraujoch and are shown with symbols of the corresponding color.

saturation. The MMM underestimates $N_{50}$, and on average NMB is −51 % and NME is 55 % for all stations. $N_{80}$ is not shown in this figure but follows a similar behavior as $N_{50}$ and $N_{120}$. It is not surprising that in almost all cases both the $N_{50}$ and the $N_{120}$ concentrations are underestimated (the average NMB for MMM for all stations is −50 % and the NME is 54 %) by a factor that is only slightly lower than the underestimation of the $CCN_{0.2}$ concentration (−50 % NMB and 60 % NME). It may therefore be concluded that the quantitative differences of the models in the prediction of CCN originate from the underestimation of the number concentration of aerosol particles in the relevant size ranges. Note, however, that the aerosol number concentration cannot be used as a proxy for CCN levels since activation of aerosols to CCN depends not only on the size distribution but also on the chemical composition of the aerosols as well as on the supersaturation that develops in clouds (e.g., Seinfeld and Pandis, 2006; Kalkavouras et al., 2019).

Figure S1 is similar to Figs. 2 and 4 but shows particulate SO4, OA mass in $PM_1$ particles at the nine stations, and model results for DU and SS. Strong seasonal variations of the SO4 mass of about 1 order of magnitude are observed and simulated at the alpine site, Jungfraujoch, and at the coastal background stations, Mace Head and Finokalia, although winter minima are overestimated by the models at these coastal sites. Smaller variation or no clear seasonal variation of SO4 is observed at the boreal forest environment of Hyytiälä, the rural background station Cabauw and at the highly polluted Melpitz station during the year. At these three stations, the MMM underestimates the observed annual mean concentration of SO4. Strong seasonal variations of the OA mass are observed and simulated at Mace Head, Finokalia, Jungfraujoch and Hyytiälä, while no distinct seasonal cycle in organic mass is seen at Cabauw and Melpitz. The MMM is underestimating OA concentrations at all sites. The IoA between the MMM and the observations is between 0.28 and 0.62 for all stations. A detailed analysis of each model separately (Table S6) shows that the OA mass concentration is underestimated (mean NMB is −37 %) by nine of the models and overestimated by six of them (range of NMB −97 % to 216 %). Because different models are appearing as outliers at each station, it is difficult to conclude whether the parameterizations in one model are better than another. This, however, is consistent with the findings of a recent OA intercomparison study that considered 31 models (Tsigaridis et al., 2014) and several modeling studies that suggest a missing source of OA needed to reconcile observations with model results (Spracklen et al., 2011; Heald et al., 2011). It appears therefore that in addition to the aerosol number concentration discussed earlier, a possible source of error in the simulation of aerosol and CCN number concentrations in the present study originates from the underestimation of the submicron OA mass at the stations where a significant contribution of the submicron OA mass to the $CCN_{0.2}$ levels has been observed (Schmale et al., 2018). The importance of the contribution of OA to the uncertainty of CCN is also supported by the PPE simulations further discussed in Sect. 5.

### 3.4 CCN persistence

The above analysis of CCN and aerosol number concentrations shows that on average the models are able to simulate the seasonal variations in CCN concentrations, while the model-to-observation differences in the CCN concentrations can be attributed mainly to a systematic underestimation of the number of aerosol particles that are large enough to act as CCN. The ability of models to simulate short-term variations (order of days) of the CCN number concentration is examined based on the calculated persistence of $CCN_{0.2}$ number concentrations during summer and winter (see Sect. 2.4) for all stations and for each model. The average persistence times for all models are compared in Fig. 7 with those derived from the observations (Schmale et al., 2018). Depending on the season and the station, the persistence time varies from a few hours (e.g., summer in Mace Head) to several days (e.g., winter in Melpitz).

Depending on the station, the persistence time is longer during winter (five stations) than during summer (four stations). The average persistence of the $CCN_{0.2}$ number concentrations simulated by the individual models is consistent with the observed change between winter and summer at six among the nine stations. At all stations, the simulations display a much smaller change from winter to summer than indi-

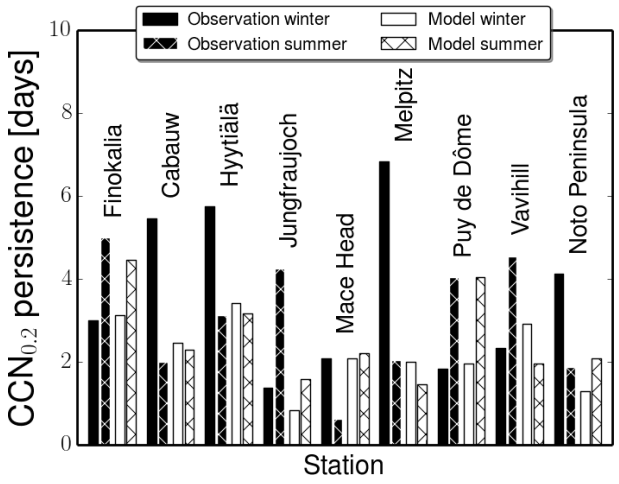


**Figure 7.** Comparison between the observed and the mean of the model-derived persistence (days) of $CCN_{0.2}$ during winter (left bar) and summer (right shaded bar) for each station. The observed persistence times are shown in black for each station and the mean of the model-derived persistence times in white. The persistence times obtained from model simulations have been computed at the same time periods as the observed ones.

cated by the observations. Furthermore, the modeled change at Mace Head, the Noto Peninsula and Vavihill is opposite to the observed one. For the high-altitude stations, Puy de Dôme and Jungfraujoch, the models calculate longer persistence times during summer than during winter, in agreement with the observations. For these two high-altitude stations, a significant increase in the number concentration of $CCN_{0.2}$ is observed during summer because the stations are subjected to the boundary layer air mass influence during that season, while during winter they are largely in the free troposphere. Therefore, despite the fact that the number concentration of $CCN_{0.2}$ is overall underestimated, the models are able to reproduce the dynamical behavior of these continental background stations, most probably because they are able to simulate the local meteorological changes that drive CCN persistence (Fig. S4 and further discussion in Sect. S3.1).

Analyzing the factors that affect the persistence and then attributing the differences between the observed and the model-derived values to the underlying physical and/or chemical process parameterizations in each model is a demanding task, which is also likely to be model and case dependent. In addition to atmospheric transport patterns, dry and wet deposition processes are presumably affecting the persistence time. Because the present exercise was not focused on the deposition of aerosols, it does not have the necessary elements to elaborate on differences in the results associated with differences in the deposition parameterizations. However, earlier global model comparisons provide insight into such differences. The Tsigaridis et al. (2014) comparison of 31 global models, among which are those participating in the present study, has shown that the representation of aerosol microphysics in the models was important for dry deposition. In particular, they have shown that the use of the M7 aerosol microphysics module was associated with low dry deposition fluxes of organic aerosol, which is mainly fine aerosol in the models, and the dry deposition rate coefficient ranged from 0.005 to $0.13\,d^{-1}$, i.e., with a max/min ratio of 26. They also found that the effective wet deposition rate coefficient in the 31 participating models ranged from 0.09 to $0.24\,d^{-1}$, i.e., with a max/min ratio of 2.6 that is 10 times lower than for dry deposition, and found virtually no change between AEROCOM phase I and AEROCOM phase II models. Kim et al. (2014) compared the deposition of dust, which is mainly coarse aerosol, calculated by a smaller subset (five) of AEROCOM models. They pointed out that the size distribution of dust differs among these models and found a 30 % difference in the effective dry deposition rate coefficient and about the same in the total deposition rate varying from 0.28 to $0.37\,d^{-1}$. The Kim et al. (2014) analysis also revealed differences in the annual precipitation rate and in its seasonal distribution in the models, as well as factor of 2 differences in the fraction of wet to total deposition of dust among the models (ranging between 0.36 and 0.63). In addition, the PPE results (see Sect. 5) clearly show that dry deposition is one of the major factors of uncertainty in the calculations of CCN in 0.2 % supersaturation. Kristiansen et al. (2016) investigated the causes of differences in aerosol lifetimes within 19 global models by making use of an observational constraint from radionuclide measurements and found largely underestimated accumulation-mode aerosol lifetimes due to removal in most models that is too fast. In particular, they found that the way aerosols are transported and scavenged in convective updrafts makes a large difference in aerosol vertical distribution and lifetimes, as revealed in their simulations from the same model (CAM5) but with different convective transport and wet removal treatments (Wang et al., 2013) .

Furthermore, the size of the emitted OA and BC particles has been shown to be an important parameter to which the persistence time and in particular the summer-to-winter ratio of the persistence time of CCN is sensitive (see sensitivity runs performed with one (TM4-ECPL) among the participating models in Sect. S3.1 and Fig. S5). Section 5 further attributes $CCN_{0.2}$ uncertainty to various parameters.

### 3.5 Cloud droplet number concentration from CCN spectra

Inside a cloudy updraft, $s_{max}$ is reached when supersaturation generation from expansion cooling becomes equal to its depletion by the condensation of water vapor onto the growing droplets (Nenes and Seinfeld, 2003). Increasing updraft velocity enhances the cooling rate of the cloudy air parcels, which in turn allows for higher supersaturation and eventually increases $s_{max}$ and CDNC ($N_d$ in the following text and figures). Increases in CCN concentrations tend to increase $N_d$

and associated water vapor depletion in the early stages of cloud formation; this in turn hinders the development of supersaturation and implies an eventual decrease in $s_{max}$. This water vapor "competition effect" is especially strong when clouds form in the presence of large, hygroscopic particles such as sea-salt aerosol or large amounts of accumulation aerosol (Morales Betancourt and Nenes, 2014a; Ghan et al., 1998). Competition effects in turn explain why droplet number responses exhibit a sublinear response to modulations in CCN; only when CCN concentrations are very low (or updraft velocities very high) does $s_{max}$ become high enough so that the sensitivity of $N_d$ to CCN approaches unity.

Based on the behavior described above, one can understand the $N_d$ predicted from simulated and observed CCN spectra. This is straightforward for the Jungfraujoch and Mace Head stations. For Cabauw and Vavihill the observed-to-simulated ratio turns from a substantial overestimation in $CCN_{0.2}$ to an underestimation in $N_d$, and the opposite is found for Finokalia. This can be explained as follows. At both Cabauw and Finokalia, $s_{max}$ derived from observations is very low (approaching in the summer 0.07 % at Finokalia and 0.04 % at Cabauw; Fig. 8). The models overestimate these low values of $s_{max}$, and such values are indicative of the presence of large particles (> 250 nm) with sufficient hygroscopicity at these stations that are not captured by the models. Indeed, at Cabauw the available observations of CCN at 0.1 % supersaturation show a larger underestimate by the models than for $CCN_{1.0}$ and $CCN_{0.2}$ (Fig. S16), also pointing to a model underestimate of the largest particles (> 250 nm) that induce the very low $s_{max}$. The overestimate in $s_{max}$ leads to an underestimate in $N_d$ by the models for all seasons except winter at Cabauw when the models at high updraft velocity capture the observationally derived $N_d$ levels. Furthermore, at Finokalia, $CCN_{1.0}$ is underestimated year-round, indicating that, in addition to the largest particles, the very small particles (smaller than 50 nm) that activate at 1.0 % supersaturation and/or their hygroscopicity are also underestimated by the models there. On the other hand, particles larger than 120 nm that activate at 0.2 % supersaturation are overestimated, especially in winter, and slightly underestimated in summer. Therefore, the global models have significant difficulties in capturing the aerosol size distribution and hygroscopicity at Finokalia, which in turn translate into counterintuitive discrepancies in $N_d$.

At Vavihill a somewhat different behavior is found; the underestimate of CCN at supersaturations of 0.2 % and 0.7 % changes to an overestimate at supersaturation 0.1 % mainly in summer (Fig. S16), indicating an underestimate of fine particles and/or their hygroscopicity and an overestimate of the largest particles and/or their hygroscopicity, in particular during summer. This agreement of model results with observations during winter and the overestimate of CCN at 0.1 % supersaturation during summer can explain the similar behavior of modeled $N_d$.

The difference between model and observationally derived $\partial N_d/\partial w$ clearly supports the above statements. Since observations predict a suppressed $s_{max}$ compared to model distributions (Fig. 8), water vapor competition effects in the observations are much more severe than in the model, indicating that observations are much more (positively) sensitive to updraft velocity. The opposite trends are seen for activation fraction ($\partial N_d/\partial N_a$), given that reductions in aerosol reduce competition effects. The reduced water vapor competition effects at higher updraft velocities and the trend in CCN error also generally explain why the sensitivities are smaller for the highest updraft velocity.

As expected, both $s_{max}$ values and $N_d$ for all observations and simulations are higher for $w = 0.6\,ms^{-1}$ than for $w = 0.3\,ms^{-1}$. The response of $s_{max}$ and $N_d$ to increasing $w$ also depends on the activated fraction (Fig. 8 third row). The calculated $N_d$ increases progressively from the low values seen for the clean marine conditions at Mace Head and the high alpine atmospheric conditions of Jungfraujoch to the rural background conditions at Cabauw and Vavihill, while at Finokalia the observationally derived $N_d$ values are the largest among the five stations (Fig. 9a). At Jungfraujoch, Finokalia and Mace Head, the seasonal variability of $N_d$ is captured, despite the fact that the multi-model median tends to underestimate the observationally derived $N_d$. However, the individual models show both overpredictions and underpredictions of the observations (Fig. S3). Owing to the water vapor competition effect, $s_{max}$ decreases for increasing $N_d$, meaning that clouds at a given location do not have a "characteristic $s_{max}$", but rather depend on the given set of aerosol and dynamical conditions that develop during the cloud formation.

For all stations except Finokalia, the agreement between the model and observationally derived $N_d$ (Fig. 8) tends to be better than for CCN (Figs. 2, 4) and aerosol number concentrations (Fig. 6) (as expressed by the MMM's NMB and NME for all stations provided in Table S6). Indeed, for all stations except Finokalia, NMB and NME of the MMM for $N_d$ vary from −7 % to −17 % and 41 % to 42 %, respectively, with the lowest values calculated for the low updraft velocity. For $CCN_{0.2}$ NMB is −59 % and NME 63 %, averaged over the same stations. This trend is a result of the competition effect of CCN on $s_{max}$; if observed CCN concentrations are higher than predicted, then the "observed" $s_{max}$ tends to be less than the "predicted" $s_{max}$, which means the discrepancy in observed and predicted $N_d$ is reduced compared to the CCN errors. The error reduction is substantial, especially under lower updraft velocity conditions. As a qualitative example we present here the ratio of the observed to the simulated average values of $CCN_{0.2}$ number concentrations: 4.0 at Jungfraujoch, 2.2 at Cabauw, 2.1 at Mace Head, 1.5 at Vavihill and 0.8 at Finokalia (Fig. 3). In the case of $N_d$ the corresponding ratios for $w = 0.6\,m\,s^{-1}$ are ∼ 1.8 at Jungfraujoch, ∼ 0.9 at Cabauw, ∼ 1.5 at Mace Head, ∼ 0.9 at Vavihill and ∼ 1.8 at Finokalia (Fig. 9). All these ratios are inversely cor-

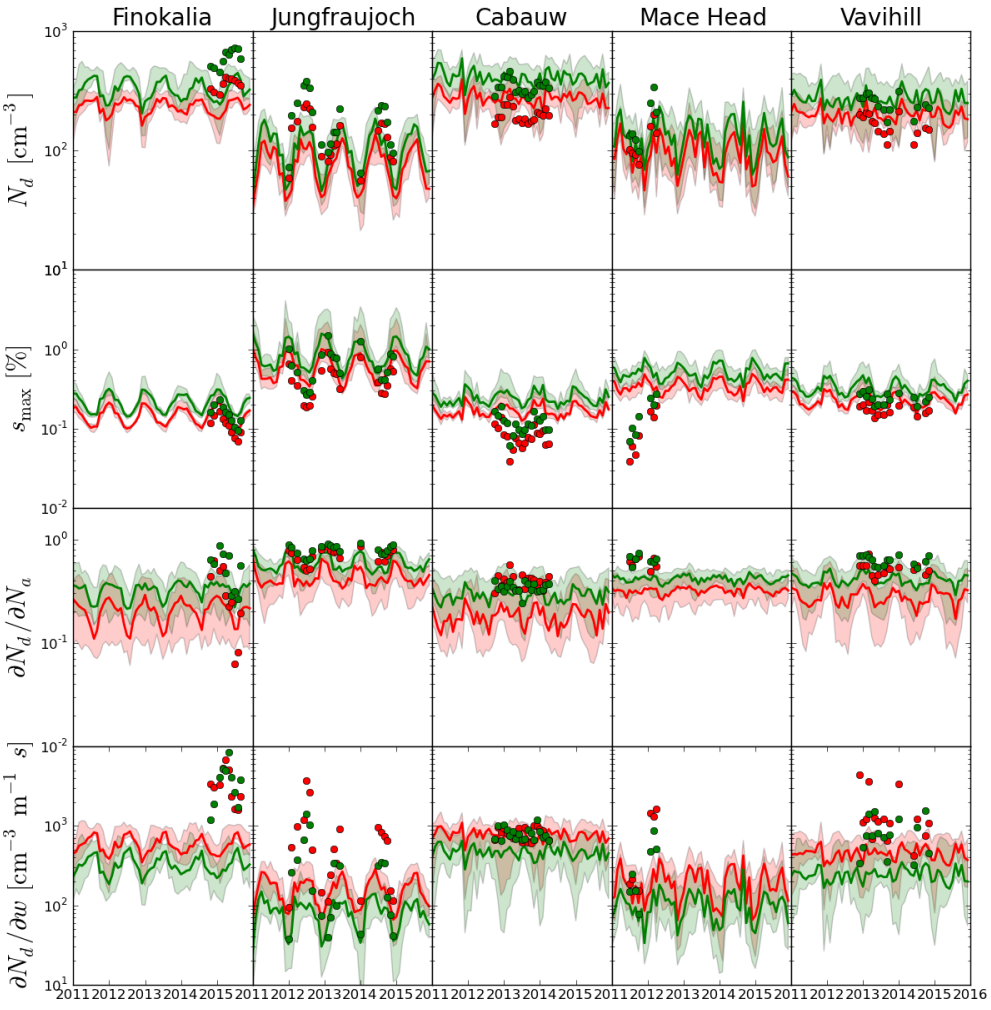


**Figure 8.** Comparison between the observed (symbols) and the monthly averages of all models (continuous lines) of the cloud droplet properties: in red for updraft velocity $w = 0.3\,\mathrm{ms}^{-1}$ and in green for updraft velocity $w = 0.6\,\mathrm{ms}^{-1}$. For each station from top to bottom the four graphs show (as indicated in the $y$ axis label) the number of cloud droplets, $N_\mathrm{d}$, the maximum supersaturation, $s_\mathrm{max}$, the sensitivity of the $N_\mathrm{d}$ to the total number of aerosol particles, $(\partial N_\mathrm{d}/\partial N_\mathrm{a})$, and the sensitivity of the $N_\mathrm{d}$ to the updraft velocity $(\partial N_\mathrm{d}/\partial w)$.

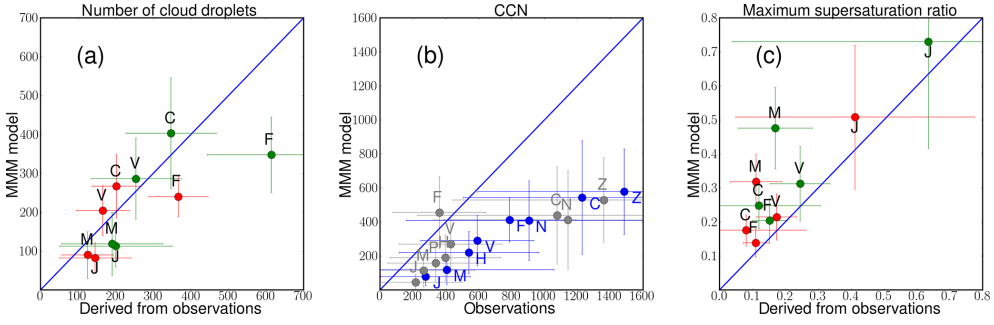


**Figure 9.** Scatter plot of the average of multi-model median results ($y$ axis) versus observationally derived results ($x$ axis) for **(a)** CDNC ($N_\mathrm{d}$) (cm$^{-3}$; in red for updraft velocity $w = 0.3\,\mathrm{ms}^{-1}$ and in green for updraft velocity $w = 0.6\,\mathrm{ms}^{-1}$); **(b)** CCN at supersaturation 0.2 % (gray) and CCN at maximum supersaturation (blue) with available data (cm$^{-3}$). To fit the scale all CCN number concentrations at maximum supersaturation (blue symbols) have been divided by 2. Panel **(c)** is as panel **(a)** but for $s_\mathrm{max}$ (%). The letters close to the symbols indicate the station names (C – Cabauw, F – Finokalia, H – Hyytiälä, J – Jungfraujoch, M – Mace Head, N – Noto Peninsula, P – Puy de Dôme, V – Vavihill, Z – Melpitz).

related with the observed to the simulated average values of $s_{max}$ (Fig. 9), a clear indication of competition effects on $N_d$ and prediction error mitigation.

In agreement with our finding, Sotiropoulou et al. (2006) used a similar approach applied to observations from the ICARTT field campaign and estimated that a 20 %–50 % error in CCN closure results in a 10 %–25 % error in $N_d$, while global simulations suggest global average CCN prediction error between 10 % and 20 % and a smaller corresponding $N_d$ error between 7 % and 14 % (Sotiropoulou et al., 2007). Such a reduction in error can be explained by self-regulation by $N_d$ since $s_{max}$ decreases with increasing aerosol number concentration, as discussed by many studies published to date (e.g., Twomey et al., 1959; Charlson et al., 2001; Nenes and Seinfeld, 2003; Feingold and Siebert, 2009), giving rise to regions where $N_d$ is relatively insensitive to changes in CCN or updraft velocity (e.g., Rissman et al., 2004; Reutter et al., 2017). At very high CCN levels and in the presence of sufficiently large hygroscopic CCN, $N_d$ may actually decrease with increases in aerosol amount (Ghan and Abdul-Razzak, 1998; Feingold, 2001; McFiggans et al., 2006; Reutter et al., 2017); parameterizations that do not fully capture these important aspects of the aerosol–droplet relationship may also give rise to biases in aerosol indirect forcing assessments (e.g., Morales-Betancourt et al., 2014a).

These results clearly indicate that the number of CCN at a prescribed supersaturation cannot be used as an indicator for the number of activated droplets. The maximum supersaturation that develops inside the cloud (hence droplet number) responds to changes in aerosol and vertical velocity levels and is thus dynamically determined and can vary considerably for a given site. This is even further complicated by the potential for model biases to change sign at cloud-relevant supersaturations. CCN-derived comparisons cannot even be used qualitatively, as the supersaturation levels can be so different from a prescribed value that even the error trend in $N_d$ may not be reflected. For example, according to observationally derived data, $CCN_{0.2}$ at Cabauw is significantly higher than at Finokalia, although at Finokalia $N_d$ is larger for the observations but not for the model results. Our analysis, however, clearly shows that the models examined here do not exhibit the same level of $N_d$ prediction error as CCN error – a robust trend that is a result of the physics of cloud droplet formation. Because of the discrepancy in the sensitivities $\partial N_d/\partial N_a$ and $\partial N_d/\partial w$, models may be predisposed to be too "aerosol sensitive" or "aerosol insensitive" in aerosol–cloud–climate interaction studies, even if they may capture average droplet numbers well. This is a subtle but profound finding that only the sensitivities can clearly reveal and may explain inter-model biases on the aerosol indirect effect. Few published efforts (apart from Morales Betancourt and Nenes, 2014a, and Sullivan et al., 2016) can demonstrate this, none over a range of models and using a considerable aerosol dataset for evaluation as performed here.

## 4 Global distributions of surface $CCN_{0.2}$ and particle number concentrations

The global near-surface annual mean MMM distributions of the $N_3$, $N_{50}$ and $CCN_{0.2}$ number concentrations for the year 2011 (Fig. 10) show similar patterns, i.e., larger concentrations over the continents due to the primary anthropogenic emissions over industrialized areas in the USA, Europe and Asia, as well as dust and biomass burning emissions in the tropics.

Multi-model median near-surface $N_3$ number concentrations over continental regions vary between 1000 and 10 600 $cm^{-3}$, while over the marine boundary layer (MBL) they vary between 100 and 2000 $cm^{-3}$, rarely exceeding 300 $cm^{-3}$ (Fig. 10a). The MMM $N_3$ surface distribution is similar to the results by Spracklen et al. (2010) and Gordon et al. (2017), who computed maximum $N_3$ concentrations of $\sim 10\,000\,cm^{-3}$. The concentration of $N_3$ is directly related to new particle formation and growth as well as to primary emitted particles. Since models use different nucleation mechanisms and emission inventories it is expected that the diversity of the model results is higher for $N_3$ than for particle number concentrations with a larger (low-end) cutoff diameter. The largest diversities in the model results (Fig. 10b) are found in the polar regions, where concentrations are relatively low, and in the continental boundary layer with high values (about 2) observed in the tropics and particularly in South America and over the boreal regions in Asia. Diversities of up to 1.5 are computed for the Mediterranean, Arabian Peninsula, Central Africa, Indonesia and Southeast Asia, indicating differences between models in the representation of primary and secondary aerosol sources in these regions. Over the oceans the diversity is lower ($< 1$) except in the high latitudes of the Northern Hemisphere where it exceeds 1.5. Even lower model diversity (around 0.8) is found in highly polluted areas over North America and Europe, indicating consistency between models in the representation of aerosols in these regions. In addition to new particle formation, our results point mainly to biomass burning emissions as a major source of uncertainty in the model calculations, resulting in high model divergence in areas like southern Europe, tropical Africa and America, southern Asia and Indonesia. Assumption of emission injection height is also a source of discrepancy between models, leading to differences in the calculated lifetimes (up to 30 %) and in the tropospheric columns (up to 25 %) of pollutants (Daskalakis et al., 2015), while differences of an order of magnitude in their concentrations are computed for the middle troposphere (Jian and Fu, 2014). Thus, differences in the emission injection heights in the participating models, as outlined in Sect. 2.1 and Table S4, contribute to the model result divergence. The highest maximum $N_3$ concentrations in a $5° \times 5°$ grid box (Fig. S6) were computed by the GISS-E2.1-MATRIX model ($\sim 176\,000\,cm^{-3}$) and the TM4-ECPL model ($\sim 102\,000\,cm^{-3}$), while the lowest were from the

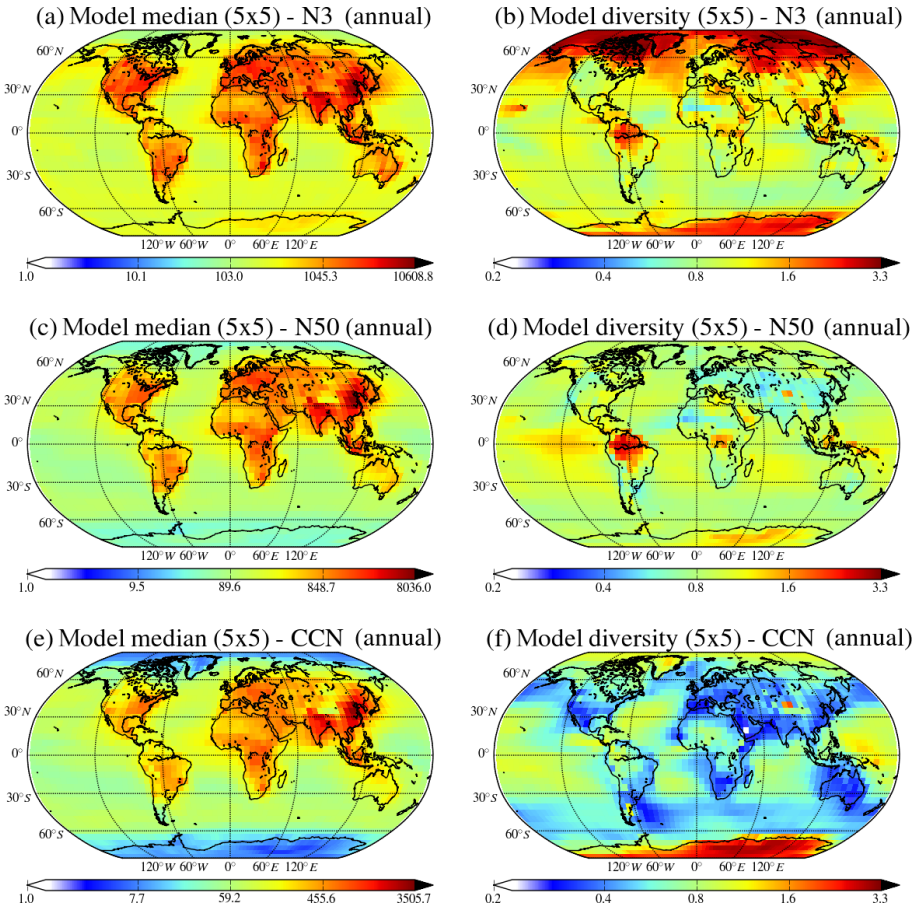


**Figure 10.** Global distributions of the annual multi-model median concentrations of $N_3$, $N_{50}$ and $CCN_{0.2}$ ($cm^{-3}$) for the year 2011 (**a, c, e**, respectively) and the corresponding diversities (**b, d, f**, respectively; calculated as the ratio of standard deviation to the mean of the models).

ECHAM6_HAM2-AP model ($\sim 6400\,cm^{-3}$). A sensitivity simulation was performed by a single model (TM4-ECPL; discussed in Sects. 3.3 and S3.1 and Fig. S5) assuming the same primary emissions of carbonaceous aerosol in terms of mass to be emitted at larger particle sizes. This additional simulation shows the importance of the assumptions on size distribution of the emissions in the models since the results of this simulation are very close to the average of the other models. In agreement with these findings, Spracklen et al. (2010) concluded that the sensitivity of $N_3$ to the size of emitted particles originating from anthropogenic activities is significantly higher in regions close to anthropogenic sources and significantly lower at remote boundary layer sites.

The annual global mean distribution of near-surface $N_{50}$ particle number concentrations (Fig. 10c) is similar to that of the $N_3$ particles, but the number concentrations are lower for these larger particle sizes that are more relevant for CCN. The spatial distributions of $N_{50}$ are similar, but their concentrations are reduced by about a factor of 2.5 compared to $N_3$. The highest values of $N_{50}$ are found over or close to industrialized regions due to anthropogenic emissions and over Central Africa and South America due to strong biomass burning emissions. Over marine regions, $N_{50}$ is higher in the Northern Hemisphere than in the Southern Hemisphere due to the outflow from continental anthropogenic sources. Despite the similarities of the global MMM distributions, the models' diversity and spatial pattern of $N_{50}$ (Fig. 10d) differ significantly from that of $N_3$. Excluding polar regions as for $N_3$, the highest model diversities for $N_{50}$ ($\sim 2$) are observed in regions with strong biomass burning emissions (southern America, Central Africa and Indonesia), and high diversities are also found over the tropical Pacific, which might be associated with marine emission representation in the models. In all other regions the diversity of $N_{50}$ simulations does not exceed 1, even over the remaining tropical and southern oceans where sea salt is important.

The near-surface MMM concentrations of $CCN_{0.2}$ do not exceed $3500\,cm^{-3}$ over polluted areas in Europe, Asia and the United States, as shown in Fig. 10e. This value is in the range of the 3162–$10\,000\,cm^{-3}$ $CCN_{0.2}$ concentrations simulated by Spracklen et al. (2011) over China and attributed to carbonaceous aerosols acting as CCN. In the present study, only one model (EMAC) computes $CCN_{0.2}$ levels that exceed $10\,000\,cm^{-3}$ over the Taklimakan Desert

in Asia, while the remaining 14 models show maximum surface $CCN_{0.2}$ concentrations $< 5000\,cm^{-3}$ (see Fig. S9). The surface distribution and magnitude of $CCN_{0.2}$ are similar to $N_{120}$ (Fig. S8), with the maximum $CCN_{0.2}$ concentrations only slightly lower than the $N_{120}$ values for most models, indicating that most of the $N_{120}$ particles activate, implying a global mean kappa of $\sim 0.2$ for 120 nm particles. However, analysis of the individual model results over the polluted areas shows that the number concentration of $N_{120}$ can, in most cases, be either 50 % lower or higher than that of $CCN_{0.2}$. The modeled $CCN_{0.2}$ diversity is lower than the diversity for $N_{50}$ with values $< 0.5$ for midlatitude continental regions and around 1 over the tropical oceans, where the $CCN_{0.2}$ number concentration is usually lower than $60\,cm^{-3}$, but also over tropical southern Africa and Central Africa where $CCN_{0.2}$ number concentration is a few hundred cubic centimeters. $CCN_{0.2}$ model diversity is also lower than that of $N_3$ simulations. The maximum reduction of the model diversity in $CCN_{0.2}$ simulations compared to that in $N_3$ simulations is found to exceed a factor of 9 and maximizes over the high latitudes of the Northern Hemisphere and the south Arabian Peninsula where new particle formation is high. Overall, a global mean reduction of a factor of about 2 is found, as shown in Fig. S18, that provides the ratio of $N_3$ model diversity (Fig. 10b) over $CCN_{0.2}$ model diversity (Fig. 10f).

Some of the differences in global near-surface distributions of CCN (Fig. S9) can be associated with the corresponding differences in the computed SO4 and OA surface distributions (Figs. S10 and S11, respectively). For instance, in China and South America, models that are biased low in SO4 and high in OA are also biased low in CCN. Significant differences are also found for black carbon, sea salt and dust $PM_1$ components (Figs. S12–S14). In particular, for all models near-surface BC distributions maximize over China, while individual models differ by a factor of 3 to 4. Simulated SS distributions maximize over the southern oceans where the models show the largest differences of up to 2 orders of magnitude, reflecting large differences in the parameterized emissions of SS (see also Table S3). Finally, DU distributions show the largest spread among models with near-surface values that differ by up to a factor of 40. The global surface distributions of the MMM of the chemical compound (SO4, BC, OA, SS and DU) concentrations that contribute to $PM_1$ are shown in Fig. S15 (left column) together with the corresponding model diversities (right column). For all simulated $PM_1$ components diversities maximize south of 60° S and north of 60° N, similarly to $N_3$, which reflects the challenges of the models in simulating atmospheric transport, deposition and chemistry close to the poles.

## 5 Causes of uncertainty in CCN

In this section we use the HadGEM-UKCA perturbed parameter ensemble (PPE) to identify some potential causes of model diversity and bias compared to the observations. We performed a variance-based sensitivity analysis at each measurement site using the 260 000 HadGEM-UKCA model variants sampled from the emulator following the methodology described in previous studies (Lee et al., 2013; Johnson et al., 2018).

Figure 11 shows the fraction of variance in $CCN_{0.2}$ that can be attributed to each of the perturbed parameters. Here we draw attention to the main parameter effects and refer to Yoshioka et al. (2019) for a full description of all parameters. The list of these parameters is provided in the caption of Fig. 11. In the summer, the largest contributions to uncertainty in $CCN_{0.2}$ at most sites come from the biogenic volatile organic compound (BVOC) emission flux and the assumed hygroscopicity of the organic matter in the particles ($\kappa_{OA}$). The BVOC emissions in this model are assumed to be $\alpha$-pinene and to have an uncertainty range of 12–225 Tg SOA production per year. The $\kappa_{OA}$ is assumed to have a range of 0.1–0.6 and to be fixed during the simulation time (i.e., the hygroscopicity does not change due to within-particle oxidation). Together, these two mostly biogenic-related parameters account for up to 90 % of the CCN variance in summer, ranging from about 0 % at Mace Head, 20 % at Cabauw, 40 % at Finokalia and 70 % at Melpitz to 90 % at Hyytiälä. These results show that at Hyytiälä the organic fraction of CCN-active aerosol is highest, while at other locations, like Mace Head, the inorganic fraction dominates the total hygroscopicity. Except at the Mace Head coastal site, the other important parameters in summer are dry deposition of aerosol, anthropogenic $SO_2$ emissions (at Finokalia, Puy de Dôme and Jungfraujoch), the fossil fuel emission flux (at the Noto Peninsula, Cabauw and Melpitz) and the assumed width of the accumulation mode (at Jungfraujoch and Puy de Dôme).

In winter, aerosol dry deposition is an important cause of uncertainty in $CCN_{0.2}$ at all sites except Jungfraujoch and Puy de Dôme. At most sites (except Mace Head and the Noto Peninsula) the emissions fluxes (and the assumed particle sizes) of carbonaceous aerosol from fossil fuel and residential combustion sources account for 10 %–20 % of the uncertainty. Aging of aerosol through the uptake of sulfuric acid and SOA is also important at these sites. Finally, the production of sulfate through in-cloud oxidation by ozone (perturbed parameter marked as "Cloud pH") accounts for 30 %–40 % of the uncertainty at Finokalia, Puy de Dôme and Jungfraujoch.

In summary, the PPE results suggest that the production of SOA from biogenic emissions combined with the hygroscopic properties of the OA should be investigated as a source of differences in predicted CCN between models in summer. In winter, dry deposition, aging and in-cloud sulfate production are the dominant sources of CCN uncertainty. Given that the importance of CCN prediction uncertainty may not always translate to CDNC uncertainty – especially if cloud formation occurs in a velocity-limited regime – any

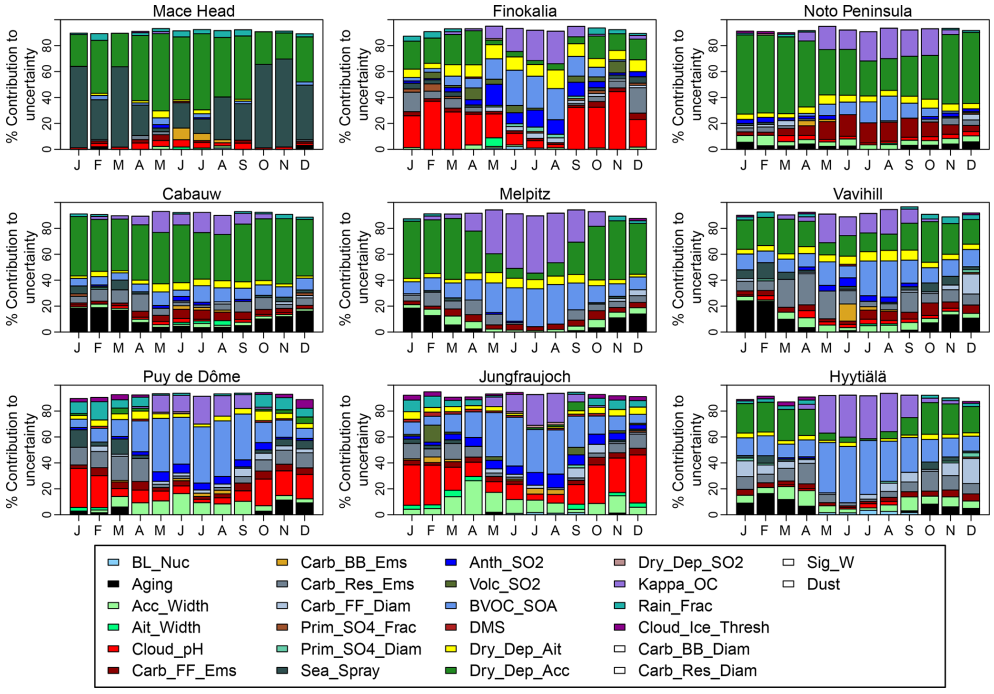


**Figure 11.** Contribution to the uncertainty in monthly average $CCN_{0.2}$ based on HadGEM3-UKCA perturbed parameter ensemble simulations for the year 2008. Each color refers to 1 of the 26 perturbed parameters as indicated in the legend of the figure. The uncertainty is shown as the percentage contribution of the parameter to the $CCN_{0.2}$ variance. The assumed parameter uncertainty ranges are given in Yoshioka et al. (2019). All contributions smaller than 1 % are not shown. Abbreviations are as follows. BL_Nuc: boundary layer nucleation; Aging: aging "rate" from insoluble to soluble; Acc_Width: modal width (accumulation soluble–insoluble); Ait_Width: modal width (Aitken soluble–insoluble); Cloud_pH: pH of cloud drops; Carb_FF_Ems: particle mass emission rate for BC and OC (fossil fuel); Carb_BB_Ems: particle mass emission rate for BC and OC (biomass burning); Carb_Res_Ems: particle mass emission rate for BC and OC (biofuel); Carb_FF_Diam: particle emitted mode diameter for BC and OC (fossil fuel); Carb_BB_Diam: particle emitted mode diameter for BC and OC (biomass burning); Carb_Res_Diam: particle emitted mode diameter for BC and OC (biofuel); Prim_SO4_Frac: mass fraction of $SO_2$ converted to new $SO_4^{-2}$ particles in sub-grid power plant plumes; Prim_SO4_Diam: mode diameter of new sub-grid $SO_4^{-2}$ particles; Sea_Spray: sea spray mass flux (coarse / accumulation); Anth_SO2: $SO_2$ emission flux (anthropogenic); Volc_SO2: $SO_2$ emission flux (volcanic); BVOC_SOA: biogenic monoterpene production of SOA; DMS: DMS emission flux; Dry_Dep_Ait: dry deposition velocity of Aitken mode aerosol; Dry_Dep_Acc: dry deposition velocity of accumulation-mode aerosol; Dry_Dep_SO2: dry deposition velocity of $SO_2$; Kappa_OC: hygroscopicity parameter kappa for organic aerosols. Default value in UKCA is 0.06; see Petters and Kreidenweis (2007). Sig_W: standard deviation of updraft velocity (this affects the activation of aerosol particles to form cloud droplets). Dust: dust emission flux; Rain_Frac: the fraction of the cloudy part of the grid box in which rain is forming and hence scavenging takes place; Cloud_Ice_Thresh: scavenging (by both cloud liquid and ice water) is suppressed in dynamic clouds when cloud ice fraction is higher than this value. The parameters with no color in the legend do not contribute to the uncertainty in $CCN_{0.2}$ (less than 1 %) at any station in any month.

future analysis should place CCN uncertainty within the context of CDNC uncertainty.

## 6 Summary and conclusions

Within the BACCHUS–AEROCOM multi-model CCN intercomparison initiative, a total of 16 global aerosol–climate and chemistry transport models were compared to each other and to observations. Among them 14 provided results for particle and CCN number concentrations and $PM_1$ component mass concentrations, which have been compared to surface observations at eight sites in Europe and one in Japan to evaluate the skill of the simulations.

In this inter-model comparison, models used different meteorology and emissions (e.g., CMIP5 and 6), as well as datasets and parameterizations. Most models (including the multi-model median) tend to underestimate the observed aerosol number concentrations $N_{50}$, $N_{80}$ and $N_{120}$, as well as the CCN concentrations, suggesting an incomplete understanding of the underlying processes. In particular, emissions and the size distribution of emitted particles, injection heights of biomass burning emissions, atmospheric aging and particularly aqueous-phase chemistry, the hygroscopicity of organic aerosol, and dry and wet deposition have been pointed out as main sources of uncertainties in model simulations. Models are, however, reproducing between 45 % and 86 % of the seasonal variability of $N_{50}$, $N_{80}$, $N_{120}$ and

$CCN_{0.2}$ number concentrations, as well as SO4 and OA $PM_1$ component mass concentrations, with the exception of Hyytiälä where only 36 % of the SO4 variability is captured by the MMM, as indicated by the correlation coefficient of the MMM with the observations (Table S6). While models have improved since the 2014 AEROCOM organic aerosol intercomparison (Tsigaridis et al., 2014), most continue to underestimate the organic submicron aerosol mass concentrations. Thus, the MMM underestimates observed OA $PM_1$ mass concentrations by 36 % (for Hyytiälä) to 77 % (for Jungfraujoch).

The simulated $N_3$ number concentrations, which are generally higher over land, show high diversity among models over the Northern Hemisphere continents, while the simulated CCN are less diverse. Overall, a global mean reduction of a factor of about 2 is found in the model diversity in $CCN_{0.2}$ simulations compared to that in $N_3$ simulations, maximizing over regions where new particle formation is important. This finding points to differences in the size distribution of primary emissions and/or in the formation and growth of new particles as important sources of the inter-model diversity in CCN.

CCN number concentrations are generally underestimated at all supersaturations by the MMM by at least 34 % (Fig. 9, Table S6), with the exception of very low supersaturations, indicating that models have most difficulty in capturing the largest particles ($> 250$ nm) that activate at very low supersaturations. There is no model that performs best at all stations. The models on average qualitatively capture the strong seasonal variabilities of CCN observed at Finokalia, the Noto Peninsula, Puy de Dôme and Jungfraujoch, as well as the very weak seasonality observed at the other stations. The production of SOA from biogenic emissions combined with the hygroscopic properties of the OA in summer and dry deposition, aging and in-cloud sulfate production in winter have been identified by PPE simulations as dominant sources of CCN uncertainty and should be investigated in the future.

The short-term variability of $CCN_{0.2}$ at the measurement sites has been examined by comparing the $CCN_{0.2}$ persistence time computed from the observed data and the model results. Because persistence time is a normalized timescale driven by the processes that "set" the CCN concentrations, it is more sensitive to air mass changes and the formation–removal rates of atmospheric particles than to the exact number concentration of CCN. With the exception of two models that estimate very large persistence times (about 16 d) during summertime at Finokalia, the modeled persistence times of near-surface $CCN_{0.2}$ are between 0.5 and 9 d depending on the model, location and season (Fig. S4), a range similar to that derived from observations that vary between about 0.5 and 7 d. At six out of nine stations the average relative change in modeled persistence time between winter and summer is in agreement with observations. These persistence times of $CCN_{0.2}$ are sensitive to assumptions on the size of the emitted particles, as shown by a sensitivity simulation with the TM4-ECPL model.

A novel aspect of this study is the comparison of ensemble global aerosol climate model near-surface results with experimentally derived CDNC from surface measurements of CCN at different levels of supersaturation. Note that CDNC is not calculated by each participating model, but a common methodology has been followed to derive the CDNC from the modeled and observed CCN spectra. Despite the large differences between models and observations found in the number concentration of aerosol particles and CCN, the CDNC estimates based on the CCN spectra are in significantly better agreement than the CCN for the stations examined here. In addition, the inter-model spread of CDNC is smaller than that of particle and CCN number concentrations. These trends are robust and a result of the physics of cloud droplet response to aerosol perturbations and show self-regulation by CDNC.

As for CCN number concentrations, in several cases models underestimate CDNC when compared to the observationally derived CDNC (Sect. 3.5). At high aerosol number concentrations, the maximum supersaturation is computed to be low, limiting the fraction of particles that can activate and form CDNC. As a result, the sensitivity of CDNC to updraft velocity prevails. In contrast, at high updraft velocities, CDNC is controlled by the variability in the aerosol number concentration. An anticorrelation is found between the sensitivity of CDNC to the number of aerosols and that to the updraft velocity, showing that the variability of these two parameters can explain the variability in CDNC and limit CDNC formation.

Our results are in agreement with previous studies showing that CDNCs are sensitive to the uncertainties in the CCN number concentrations, mainly in regions where aerosol number concentrations are low and support the concept of the existence of two distinct regimes ("aerosol limited" and "updraft limited"). Unlike previous studies, however, we show that for a large number of models, persistent and substantial CCN prediction biases are considerably reduced when expressed as droplet number concentrations for boundary-layer-type clouds. Biases in CDNC are found to be qualitatively different from the biases in $CCN_{0.2}$ and are attributed to the ability of models to capture the levels of the largest particles that activate at very low cloud-relevant supersaturations. These results point to the need for observations that cover the CCN spectra down to very low supersaturation levels and demonstrate that model–observation comparisons of CCN at a prescribed supersaturation may be misleading in the error evaluation for CDNC, since supersaturation is dynamically determined and can vary considerably for a given site. The methodology proposed here, however, overcomes this limitation and considers the dynamic nature of supersaturation adjustment to CCN variations, thus determining appropriate supersaturation levels for model–observation comparison. Such a methodology can help better guide modeling efforts to focus on regions where CDNC predictions are most

biased and sensitive to CCN perturbations (e.g., in the southern oceans).

*Data availability.* The data used for this study are available online at https://doi.org/10.5281/zenodo.3265866 (Fanourgakis et al., 2019) (contact: Maria Kanakidou at mariak@uoc.gr). CDNC analysis tools for model and observational data can be obtained from athanasios.nenes@epfl.ch upon request.

*Supplement.* The supplement related to this article is available online at: https://doi.org/10.5194/acp-19-8591-2019-supplement.

*Author contributions.* GF performed TM4-ECPL model simulations, developed codes and drew all figures for the multi-model data analysis. MK initiated and coordinated the exercise. AN developed the codes to interpret the CCN spectra from all models and from the observations and to calculate CDNC. MK and AN defined the experimental protocol. GF, MK and AN analyzed data and wrote the paper. All coauthors contributed data and to the writing of the paper.

*Competing interests.* The authors declare that they have no conflict of interest.

*Special issue statement.* This article is part of the special issue "BACCHUS – Impact of Biogenic versus Anthropogenic emissions on Clouds and Climate: towards a Holistic UnderStanding (ACP/AMT/GMD inter-journal SI)". It is not associated with a conference.

*Acknowledgements.* This work has been initiated and conducted within the European Union's Seventh Framework Programme (FP7/2007-2013) collaborative project BACCHUS (Impact of Biogenic versus Anthropogenic emissions on Clouds and Climate: towards a Holistic UnderStanding). Dirk Olivie has contributed with coding and information about the emission heights used in CAM5.3-Oslo. Yunha Lee developed the GISS-E2-TOMAS model used in this study. The ECHAM-HAMMOZ model is developed by a consortium composed of ETH Zurich, the Max Planck Institut für Meteorologie, Forschungszentrum Jülich, the University of Oxford, the Finnish Meteorological Institute and the Leibniz Institute for Tropospheric Research; it is managed by the Center for Climate Systems Modeling (C2SM) at ETH Zurich. Hailong Wang and Yang Yang acknowledge support from the U.S. Department of Energy (DOE) Biological and Environmental Research and the ACTIVATE project (a NASA Earth Venture Suborbital-3 investigation) funded by NASA's Earth Science Division and managed through the Earth System Science Pathfinder Program Office. The Pacific Northwest National Laboratory (PNNL) is operated for the DOE by the Battelle Memorial Institute under contract DE-AC05-76RLO1830. The CAM5_MAM3 simulation was performed using PNNL institutional computing resources. Resources supporting this work were also provided by the NASA High-End Computing (HEC) program through the NASA Center for Climate Simulation (NCCS) at Goddard Space Flight Center. Martin Gysel-Beer acknowledges support from MeteoSwiss in the framework of the Swiss contributions (GAW-CH and GAW-CH-Plus) to the Global Atmosphere Watch program of the World Meteorological Organization (WMO). This work was finalized when Maria Kanakidou was visiting L. Gallardo at the Center for Climate and Resilience Research (CR2) at the Geophysics Department of the University of Chile where Maria Kanakidou profited from fruitful discussions.

*Financial support.* This research has been supported by the FP7 Environment (grant no. BACCHUS (603445)), the H2020 Environment (grant nos. CRESCENDO (641816) and ACTRIS2 (654109)), and the H2020 European Research Council (grant nos. PyroTRACH (726165) and RECAP (724602)). The contributing authors were also supported by the following: the Norwegian Research Council (grant nos. 207711/E10, 229771, nn2345k and ns2345k); the Nordic Centre of Excellence eSTICC (grant no. 57001); the Natural Environment Research Council project (grant no. NE/L01355X/1); the Japan Society for the Promotion of Science, the Ministry of Education, Culture, Sports, Science, and Technology and the Japan Society for the Promotion of Science (grant nos. JP26740014, JP17H04709, JP26241003 and JP16H01770); the MEXT Green Network of Excellence and Arctic Challenge for Sustainability projects and the Environment Research and Technology Development Fund of the Environmental Restoration and Conservation Agency (grant nos. 2-1403, 2-1703); the U.S. National Science Foundation Atmospheric Chemistry Program (grant nos. AGS-1559607 and 1550816); the U.S. National Oceanic and Atmospheric Administration, an Office of Science, Office of Atmospheric Chemistry, Carbon Cycle, and Climate Program (grant no. NA17OAR430001); NASA (grant nos. NNX13AK20G and NNX15AE36G); the Swiss State Secretariat for Education, Research and Innovation (SERI) (grant no. 15.0159-1); and the Swiss National Supercomputing Centre (grant no. s652).

*Review statement.* This paper was edited by Joachim Curtius and reviewed by two anonymous referees.

## References

Abdul Razzak, H. and Ghan, S. J.: A parameterization of aerosol activation: 2. Multiple aerosol types, J. Geophys. Res.-Atmos., 105, 6837–6844, https://doi.org/10.1029/1999JD901161, 2000.

Adams, P. J. and Seinfeld, J. H.: Predicting global aerosol size distributions in general circulation models, J. Geophys. Res.-Atmos., 107, 1–23, https://doi.org/10.1029/2001JD001010, 2002.

Barahona, D. and Nenes, A.: Parameterization of cloud droplet formation in large-scale models: Including effects of entrainment, J. Geophys. Res.-Atmos., 112, 1–14, https://doi.org/10.1029/2007JD008473, 2007.

Barahona, D., Molod, A., Bacmeister, J., Nenes, A., Gettelman, A., Morrison, H., Phillips, V., and Eichmann, A.: Development of two-moment cloud microphysics for liquid and ice within the NASA Goddard Earth Observing System Model (GEOS-5),

Geosci. Model Dev., 7, 1733–1766, https://doi.org/10.5194/gmd-7-1733-2014, 2014.

Bauer, S. E., Wright, D. L., Koch, D., Lewis, E. R., McGraw, R., Chang, L.-S., Schwartz, S. E., and Ruedy, R.: MATRIX (Multiconfiguration Aerosol TRacker of mIXing state): an aerosol microphysical module for global atmospheric models, Atmos. Chem. Phys., 8, 6003–6035, https://doi.org/10.5194/acp-8-6003-2008, 2008.

Bian, H., Chin, M., Hauglustaine, D. A., Schulz, M., Myhre, G., Bauer, S. E., Lund, M. T., Karydis, V. A., Kucsera, T. L., Pan, X., Pozzer, A., Skeie, R. B., Steenrod, S. D., Sudo, K., Tsigaridis, K., Tsimpidi, A. P., and Tsyro, S. G.: Investigation of global particulate nitrate from the AeroCom phase III experiment, Atmos. Chem. Phys., 17, 12911–12940, https://doi.org/10.5194/acp-17-12911-2017, 2017.

Boucher, O., Randall, D., Artaxo, P., Bretherton, C., Feingold, G., Forster, P., Kerminen, V.-M., Kondo, Y., Liao, H., Lohmann, U., Rasch, P., Satheesh, S. K., Sherwood, S., Stevens, B., and Zhang, X. Y.: Clouds and Aerosols, in: Climate Change 2013 – The Physical Science Basis, edited by: Intergovernmental Panel on Climate Change, 571–658, Cambridge University Press, Cambridge, 2013.

Bougiatioti, A., Fountoukis, C., Kalivitis, N., Pandis, S. N., Nenes, A., and Mihalopoulos, N.: Cloud condensation nuclei measurements in the marine boundary layer of the Eastern Mediterranean: CCN closure and droplet growth kinetics, Atmos. Chem. Phys., 9, 7053–7066, https://doi.org/10.5194/acp-9-7053-2009, 2009.

Bougiatioti, A., Nenes, A., Fountoukis, C., Kalivitis, N., Pandis, S. N., and Mihalopoulos, N.: Size-resolved CCN distributions and activation kinetics of aged continental and marine aerosol, Atmos. Chem. Phys., 11, 8791–8808, https://doi.org/10.5194/acp-11-8791-2011, 2011.

Bougiatioti, A., Bezantakos, S., Stavroulas, I., Kalivitis, N., Kokkalis, P., Biskos, G., Mihalopoulos, N., Papayannis, A., and Nenes, A.: Biomass-burning impact on CCN number, hygroscopicity and cloud formation during summertime in the eastern Mediterranean, Atmos. Chem. Phys., 16, 7389–7409, https://doi.org/10.5194/acp-16-7389-2016, 2016.

Charlson, R. J., Seinfeld, J. H., Nenes, A., Kulmala, M., Laaksonen, A., and Facchini, M. C.: Reshaping the Theory of Cloud Formation, Science, 292, 2025–2026, 2001.

Cubison, M. J., Ervens, B., Feingold, G., Docherty, K. S., Ulbrich, I. M., Shields, L., Prather, K., Hering, S., and Jimenez, J. L.: The influence of chemical composition and mixing state of Los Angeles urban aerosol on CCN number and cloud properties, Atmos. Chem. Phys., 8, 5649–5667, https://doi.org/10.5194/acp-8-5649-2008, 2008.

D'Andrea, S. D., Häkkinen, S. A. K., Westervelt, D. M., Kuang, C., Levin, E. J. T., Kanawade, V. P., Leaitch, W. R., Spracklen, D. V., Riipinen, I., and Pierce, J. R.: Understanding global secondary organic aerosol amount and size-resolved condensational behavior, Atmos. Chem. Phys., 13, 11519–11534, https://doi.org/10.5194/acp-13-11519-2013, 2013.

D'Andrea, S. D., Ng, J. Y., Kodros, J. K., Atwood, S. A., Wheeler, M. J., Macdonald, A. M., Leaitch, W. R., and Pierce, J. R.: Source attribution of aerosol size distributions and model evaluation using Whistler Mountain measurements and GEOS-Chem-TOMAS simulations, Atmos. Chem. Phys., 16, 383–396, https://doi.org/10.5194/acp-16-383-2016, 2016.

Daskalakis, N., Myriokefalitakis, S., and Kanakidou, M.: Sensitivity of tropospheric loads and lifetimes of short lived pollutants to fire emissions, Atmos. Chem. Phys., 15, 3543–3563, https://doi.org/10.5194/acp-15-3543-2015, 2015.

Deng, Z. Z., Zhao, C. S., Ma, N., Ran, L., Zhou, G. Q., Lu, D. R., and Zhou, X. J.: An examination of parameterizations for the CCN number concentration based on in situ measurements of aerosol activation properties in the North China Plain, Atmos. Chem. Phys., 13, 6227–6237, https://doi.org/10.5194/acp-13-6227-2013, 2013.

Dentener, F., Kinne, S., Bond, T., Boucher, O., Cofala, J., Generoso, S., Ginoux, P., Gong, S., Hoelzemann, J. J., Ito, A., Marelli, L., Penner, J. E., Putaud, J.-P., Textor, C., Schulz, M., van der Werf, G. R., and Wilson, J.: Emissions of primary aerosol and precursor gases in the years 2000 and 1750 prescribed data-sets for AeroCom, Atmos. Chem. Phys., 6, 4321–4344, https://doi.org/10.5194/acp-6-4321-2006, 2006.

Dusek, U., Frank, G. P., Hildebrandt, L., Curtius, J., Schneider, J., Walter, S., Chand, D., Drewnick, F., Hings, S., Jung, D., Borrmann, S., and Andreae, M. O.: Size Matters More Than Chemistry Aerosol Particles, Science, 80, 1375–1378, https://doi.org/10.1126/science.1125261, 2006.

Ervens, B., Cubison, M., Andrews, E., Feingold, G., Ogren, J. A., Jimenez, J. L., DeCarlo, P., and Nenes, A.: Prediction of cloud condensation nucleus number concentration using measurements of aerosol size distributions and composition and light scattering enhancement due to humidity, J. Geophys. Res., 112, D10S32, https://doi.org/10.1029/2006JD007426, 2007.

Ervens, B., Cubison, M. J., Andrews, E., Feingold, G., Ogren, J. A., Jimenez, J. L., Quinn, P. K., Bates, T. S., Wang, J., Zhang, Q., Coe, H., Flynn, M., and Allan, J. D.: CCN predictions using simplified assumptions of organic aerosol composition and mixing state: a synthesis from six different locations, Atmos. Chem. Phys., 10, 4795–4807, https://doi.org/10.5194/acp-10-4795-2010, 2010.

Fan, J., Wang, Y., Rosenfeld, D., Liu, X., Fan, J., Wang, Y., Rosenfeld, D., and Liu, X.: Review of Aerosol – Cloud Interactions: Mechanisms, Significance, and Challenges, J. Atmos. Sci., 73, 4221–4252, https://doi.org/10.1175/JAS-D-16-0037.1, 2016.

Fanourgakis, G., Kanakidou, M., Nenes, A., Bauer, S. E., Bergman, T., Carslaw, K. S., Grini, A., Hamilton, D. S., Johnson, J. S., Karydis, V. A., Kirkevåg, A., Kodros, J. K., Lohmann, U., Luo, G., Makkonen, R., Matsui, H., Neubauer, D., Pierce, J. R., Schmale, J., Stier, P., Tsigaridis, K., van Noije, T., Wang, H., Watson-Parris, D., Westervelt, D. M., Yang, Y., Yoshioka, M., Daskalakis, N., Decesari, S., Gysel-Beer, M., Kalivitis, N., Liu, X., Mahowald, N. M., Myriokefalitakis, S., Schrödner, R., Sfakianaki, M., Tsimpidi, A. P., Wu, M., and Yu, F.: Data for the "Evaluation of global simulations of aerosol particle and cloud condensation nuclei number, with implications for cloud droplet formation", Zenodo, Version v1, Data set, https://doi.org/10.5281/zenodo.3265866, 2019.

Feingold, G.: Analysis of smoke impact on clouds in Brazilian biomass burning regions: An extension of Twomey's approach, J. Geophys. Res., 106, 22907–22922, 2001.

Feingold, G. and Siebert, H.: Cloud–Aerosol Interactions from the Micro to the Cloud Scale, in: Clouds in the Perturbed Climate

System: Their Relationship to Energy Balance, Atmospheric Dynamics, and Precipitation, edited by: Heintzenberg, J. and Charlson,, R. J., MIT Press, 2009.

Fountoukis, C. and Nenes, A.: Continued development of a cloud droplet formation parameterization for global climate models, J. Geophys. Res.-Atmos., 110, 1–10, https://doi.org/10.1029/2004JD005591, 2005.

Fountoukis, C. and Nenes, A.: ISORROPIA II: a computationally efficient thermodynamic equilibrium model for $K^+-Ca^{2+}-Mg^{2+}-NH_4^+-Na^+-SO_4^{2-}-NO_3^--Cl^--H_2O$ aerosols, Atmos. Chem. Phys., 7, 4639–4659, https://doi.org/10.5194/acp-7-4639-2007, 2007.

Ghan, S. J., Gutzman, G. and Abdul-Razzak, H.: Competition between Sea Salt and Sulfate Particles as Cloud Condensation Nuclei, J. Atmos. Sci., 55, 3340–3347, 1998.

Gordon, H., Kirkby, J., Baltensperger, U., Bianchi, F., Breitenlechner, M., Curtius, J., Dias, A., Dommen, J., Donahue, N. M., Dunne, E. M., Duplissy, J., Ehrhart, S., Flagan, R. C., Frege, C., Fuchs, C., Hansel, A., Hoyle, C. R., Kulmala, M., Kürten, A., Lehtipalo, K., Makhmutov, V., Molteni, U., Rissanen, M. P., Stozkhov, Y., Tröstl, J., Tsagkogeorgas, G., Wagner, R., Williamson, C., Wimmer, D., Winkler, P. M., Yan, C., and Carslaw, K. S.: Causes and importance of new particle formation in the present-day and preindustrial atmospheres, J. Geophys. Res.-Atmos., 122, 8739–8760, https://doi.org/10.1002/2017JD026844, 2017.

Heald, C. L., Coe, H., Jimenez, J. L., Weber, R. J., Bahreini, R., Middlebrook, A. M., Russell, L. M., Jolleys, M., Fu, T.-M., Allan, J. D., Bower, K. N., Capes, G., Crosier, J., Morgan, W. T., Robinson, N. H., Williams, P. I., Cubison, M. J., DeCarlo, P. F., and Dunlea, E. J.: Exploring the vertical profile of atmospheric organic aerosol: comparing 17 aircraft field campaigns with a global model, Atmos. Chem. Phys., 11, 12673—12696, https://doi.org/10.5194/acp-11-12673-2011, 2011.

Herrmann, E., Weingartner, E., Henne, S., L., V., Bukowiecki, N., Steinbacher, M., Conen, F., Collaud Coen, M., Hammer, E., Jurányi, Z., Baltensperger, U., and Gysel, M.: Analysis of long-term aerosol size distribution data from Jungfraujoch with emphasis on free tropospheric conditions, cloud influence, and air mass transport. J. Geophys. Res., 120, 9459–9480, https://doi.org/10.1002/2015JD023660, 2015.

Huneeus, N., Schulz, M., Balkanski, Y., Griesfeller, J., Prospero, J., Kinne, S., Bauer, S., Boucher, O., Chin, M., Dentener, F., Diehl, T., Easter, R., Fillmore, D., Ghan, S., Ginoux, P., Grini, A., Horowitz, L., Koch, D., Krol, M. C., Landing, W., Liu, X., Mahowald, N., Miller, R., Morcrette, J.-J., Myhre, G., Penner, J., Perlwitz, J., Stier, P., Takemura, T., and Zender, C. S.: Global dust model intercomparison in AeroCom phase I, Atmos. Chem. Phys., 11, 7781–7816, https://doi.org/10.5194/acp-11-7781-2011, 2011.

Iwamoto, Y., Kinouchi, K., Watanabe, K., Yamazaki, N., and Matsuki, A.: Simultaneous measurement of CCN activity and chemical composition of fine-mode aerosols at Noto peninsula, Japan, in autumn 2012, Aerosol Air Qual. Res., 16, 2107–2118, 2016.

Jian, Y. and Fu, T.-M.: Injection heights of springtime biomass-burning plumes over peninsular Southeast Asia and their impacts on long-range pollutant transport, Atmos. Chem. Phys., 14, 3977–3989, https://doi.org/10.5194/acp-14-3977-2014, 2014.

Jimenez, J. L., Canagaratna, M. R., Donahue, N. M., Prevot, A. S. H., Zhang, Q., Kroll, J. H., DeCarlo, P. F., Allan, J. D., Coe, H., Ng, N. L., Aiken, A. C., Docherty, K. S., Ulbrich, I. M., Grieshop, A. P., Robinson, A. L., Duplissy, J., Smith, J. D., Wilson, K. R., Lanz, V. A., Hueglin, C., Sun, Y. L., Tian, J., Laaksonen, A., Raatikainen, T., Rautiainen, J., Vaattovaara, P., Ehn, M., Kulmala, M., Tomlinson, J. M., Collins, D. R., Cubison, M. J., Dunlea, E. J., Huffman, J. A., Onasch, T. B., Alfarra, M. R., Williams, P. I., Bower, K., Kondo, Y., Schneider, J., Drewnick, F., Borrmann, S., Weimer, S., Demerjian, K., Salcedo, D., Cottrell, L., Griffin, R., Takami, A., Miyoshi, T., Hatakeyama, S., Shimono, A., Sun, J. Y., Zhang, Y. M., Dzepina, K., Kimmel, J. R., Sueper, D., Jayne, J. T., Herndon, S. C., Trimborn, A. M., Williams, L. R., Wood, E. C., Middlebrook, A. M., Kolb, C. E., Baltensperger, U., and Worsnop, D. R.: Evolution of organic aerosols in the atmosphere, Science, 80, 1525–1529, https://doi.org/10.1126/science.1180353, 2009.

Johnson, J. S., Regayre, L. A., Yoshioka, M., Pringle, K. J., Lee, L. A., Sexton, D. M. H., Rostron, J. W., Booth, B. B. B., and Carslaw, K. S.: The importance of comprehensive parameter sampling and multiple observations for robust constraint of aerosol radiative forcing, Atmos. Chem. Phys., 18, 13031–13053, https://doi.org/10.5194/acp-18-13031-2018, 2018.

Jurányi, Z., Gysel, M., Weingartner, E., Bukowiecki, N., Kammermann, L., and Baltensperger, U.: A 17 month climatology of the cloud condensation nuclei number concentration at the high alpine site Jungfraujoch, J. Geophys. Res., 116, D10204, https://doi.org/10.1029/2010JD015199, 2011.

Kalivitis, N., Kerminen, V.-M., Kouvarakis, G., Stavroulas, I., Bougiatioti, A., Nenes, A., Manninen, H. E., Petäjä, T., Kulmala, M., and Mihalopoulos, N.: Atmospheric new particle formation as a source of CCN in the eastern Mediterranean marine boundary layer, Atmos. Chem. Phys., 15, 9203–9215, https://doi.org/10.5194/acp-15-9203-2015, 2015.

Kalkavouras, P., Bougiatioti, A., Kalivitis, N., Stavroulas, I., Tombrou, M., Nenes, A., and Mihalopoulos, N.: Regional new particle formation as modulators of cloud condensation nuclei and cloud droplet number in the eastern Mediterranean, Atmos. Chem. Phys., 19, 6185–6203, https://doi.org/10.5194/acp-19-6185-2019, 2019.

Kanakidou, M., Seinfeld, J. H., Pandis, S. N., Barnes, I., Dentener, F. J., Facchini, M. C., Van Dingenen, R., Ervens, B., Nenes, A., Nielsen, C. J., Swietlicki, E., Putaud, J. P., Balkanski, Y., Fuzzi, S., Horth, J., Moortgat, G. K., Winterhalter, R., Myhre, C. E. L., Tsigaridis, K., Vignati, E., Stephanou, E. G., and Wilson, J.: Organic aerosol and global climate modelling: a review, Atmos. Chem. Phys., 5, 1053–1123, https://doi.org/10.5194/acp-5-1053-2005, 2005.

Karydis, V. A., Capps, S. L., Russell, A. G., and Nenes, A.: Adjoint sensitivity of global cloud droplet number to aerosol and dynamical parameters, Atmos. Chem. Phys., 12, 9041–9055, https://doi.org/10.5194/acp-12-9041-2012, 2012.

Kerminen, V.-M., Petäjä, T., Manninen, H. E., Paasonen, P., Nieminen, T., Sipilä, M., Junninen, H., Ehn, M., Gagné, S., Laakso, L., Riipinen, I., Vehkamäki, H., Kurten, T., Ortega, I. K., Dal Maso, M., Brus, D., Hyvärinen, A., Lihavainen, H., Leppä, J., Lehtinen, K. E. J., Mirme, A., Mirme, S., Hõrrak, U., Berndt, T., Stratmann, F., Birmili, W., Wiedensohler, A., Metzger, A., Dommen, J., Baltensperger, U., Kiendler-Scharr, A., Mentel, T.

F., Wildt, J., Winkler, P. M., Wagner, P. E., Petzold, A., Minikin, A., Plass-Dülmer, C., Pöschl, U., Laaksonen, A., and Kulmala, M.: Atmospheric nucleation: highlights of the EUCAARI project and future directions, Atmos. Chem. Phys., 10, 10829–10848, https://doi.org/10.5194/acp-10-10829-2010, 2010.

Kerminen, V.-M., Paramonov, M., Anttila, T., Riipinen, I., Fountoukis, C., Korhonen, H., Asmi, E., Laakso, L., Lihavainen, H., Swietlicki, E., Svenningsson, B., Asmi, A., Pandis, S. N., Kulmala, M., and Petäjä, T.: Cloud condensation nuclei production associated with atmospheric nucleation: a synthesis based on existing literature and new results, Atmos. Chem. Phys., 12, 12037–12059, https://doi.org/10.5194/acp-12-12037-2012, 2012.

Kim, D., Chin, M., Yu, H., Diehl, T., Tan, Q., Kahn, R. A., Tsigaridis, K., Bauer, S. E., Takemura, T., Pozzoli, L., Bellouin, N., Schulz, M., Peyridieu, S., Chédin, A., and Koffi, B.: Sources, sinks, and transatlantic transport of North African dust aerosol: A multimodel analysis and comparison with remote sensing data, J. Geophys. Res.-Atmos., 119, 6259–6277, https://doi.org/10.1002/2013JD021099. 2014.

Kirkevåg, A., Grini, A., Olivié, D., Seland, Ø., Alterskjær, K., Hummel, M., Karset, I. H. H., Lewinschal, A., Liu, X., Makkonen, R., Bethke, I., Griesfeller, J., Schulz, M., and Iversen, T.: A production-tagged aerosol module for Earth system models, OsloAero5.3 – extensions and updates for CAM5.3-Oslo, Geosci. Model Dev., 11, 3945–3982, https://doi.org/10.5194/gmd-11-3945-2018, 2018.

Köhler, H.: The nucleus in and the growth of hygroscopic droplets, Trans. Faraday Soc., 32, 1152–1161, https://doi.org/10.1039/TF9363201152, 1936.

Kristiansen, N. I., Stohl, A., Olivié, D. J. L., Croft, B., Søvde, O. A., Klein, H., Christoudias, T., Kunkel, D., Leadbetter, S. J., Lee, Y. H., Zhang, K., Tsigaridis, K., Bergman, T., Evangeliou, N., Wang, H., Ma, P.-L., Easter, R. C., Rasch, P. J., Liu, X., Pitari, G., Di Genova, G., Zhao, S. Y., Balkanski, Y., Bauer, S. E., Faluvegi, G. S., Kokkola, H., Martin, R. V., Pierce, J. R., Schulz, M., Shindell, D., Tost, H., and Zhang, H.: Evaluation of observed and modelled aerosol lifetimes using radioactive tracers of opportunity and an ensemble of 19 global models, Atmos. Chem. Phys., 16, 3525–3561, https://doi.org/10.5194/acp-16-3525-2016, 2016.

Kulmala, M. and Kerminen, V. M.: On the formation and growth of atmospheric nanoparticles, Atmos. Res., 90, 132–150, https://doi.org/10.1016/j.atmosres.2008.01.005, 2008.

Kulmala, M., Laaksonen, A., and Pirjola, L.: Parameterizations for sulfuric acid/water nucleation rates, J. Geophys. Res., 103, 8301, https://doi.org/10.1029/97JD03718, 1998.

Laaksonen, A., Kulmala, M., O'Dowd, C. D., Joutsensaari, J., Vaattovaara, P., Mikkonen, S., Lehtinen, K. E. J., Sogacheva, L., Dal Maso, M., Aalto, P., Petäjä, T., Sogachev, A., Yoon, Y. J., Lihavainen, H., Nilsson, D., Facchini, M. C., Cavalli, F., Fuzzi, S., Hoffmann, T., Arnold, F., Hanke, M., Sellegri, K., Umann, B., Junkermann, W., Coe, H., Allan, J. D., Alfarra, M. R., Worsnop, D. R., Riekkola, M.-L., Hyötyläinen, T., and Viisanen, Y.: The role of VOC oxidation products in continental new particle formation, Atmos. Chem. Phys., 8, 2657–2665, https://doi.org/10.5194/acp-8-2657-2008, 2008.

Lee, L. A., Pringle, K. J., Reddington, C. L., Mann, G. W., Stier, P., Spracklen, D. V., Pierce, J. R., and Carslaw, K. S.: The magnitude and causes of uncertainty in global model simulations of cloud condensation nuclei, Atmos. Chem. Phys., 13, 8879–8914, https://doi.org/10.5194/acp-13-8879-2013, 2013.

Lee, Y. H., Adams, P. J., and Shindell, D. T.: Evaluation of the global aerosol microphysical ModelE2-TOMAS model against satellite and ground-based observations, Geosci. Model Dev., 8, 631–667, https://doi.org/10.5194/gmd-8-631-2015, 2015.

Liu, X., Easter, R. C., Ghan, S. J., Zaveri, R., Rasch, P., Shi, X., Lamarque, J.-F., Gettelman, A., Morrison, H., Vitt, F., Conley, A., Park, S., Neale, R., Hannay, C., Ekman, A. M. L., Hess, P., Mahowald, N., Collins, W., Iacono, M. J., Bretherton, C. S., Flanner, M. G., and Mitchell, D.: Toward a minimal representation of aerosols in climate models: description and evaluation in the Community Atmosphere Model CAM5, Geosci. Model Dev., 5, 709–739, https://doi.org/10.5194/gmd-5-709-2012, 2012.

Liu, X., Ma, P.-L., Wang, H., Tilmes, S., Singh, B., Easter, R. C., Ghan, S. J., and Rasch, P. J.: Description and evaluation of a new four-mode version of the Modal Aerosol Module (MAM4) within version 5.3 of the Community Atmosphere Model, Geosci. Model Dev., 9, 505–522, https://doi.org/10.5194/gmd-9-505-2016, 2016.

Makkonen, R., Asmi, A., Korhonen, H., Kokkola, H., Järvenoja, S., Räisänen, P., Lehtinen, K. E. J., Laaksonen, A., Kerminen, V.-M., Järvinen, H., Lohmann, U., Bennartz, R., Feichter, J., and Kulmala, M.: Sensitivity of aerosol concentrations and cloud properties to nucleation and secondary organic distribution in ECHAM5-HAM global circulation model, Atmos. Chem. Phys., 9, 1747–1766, https://doi.org/10.5194/acp-9-1747-2009, 2009.

Mann, G. W., Carslaw, K. S., Ridley, D. A., Spracklen, D. V., Pringle, K. J., Merikanto, J., Korhonen, H., Schwarz, J. P., Lee, L. A., Manktelow, P. T., Woodhouse, M. T., Schmidt, A., Breider, T. J., Emmerson, K. M., Reddington, C. L., Chipperfield, M. P., and Pickering, S. J.: Intercomparison of modal and sectional aerosol microphysics representations within the same 3-D global chemical transport model, Atmos. Chem. Phys., 12, 4449–4476, https://doi.org/10.5194/acp-12-4449-2012, 2012.

Matsui, H.: Development of a global aerosol model using a two-dimensional sectional method?: 1, Model design, J. Adv. Model. Earth Syst., 9, 1921–1947, https://doi.org/10.1002/2017MS000936, 2017.

McFiggans, G., Artaxo, P., Baltensperger, U., Coe, H., Facchini, M. C., Feingold, G., Fuzzi, S., Gysel, M., Laaksonen, A., Lohmann, U., Mentel, T. F., Murphy, D. M., O'Dowd, C. D., Snider, J. R., and Weingartner, E.: The effect of physical and chemical aerosol properties on warm cloud droplet activation, Atmos. Chem. Phys., 6, 2593–2649, https://doi.org/10.5194/acp-6-2593-2006, 2006.

Metzger, S., Dentener, F., Pandis, S., and Lelieveld, J.: Gas/aerosol partitioning: 1. A computationally efficient model, J. Geophys. Res.-Atmos., 107, 16-1–24, https://doi.org/10.1029/2001JD001102, 2002a.

Metzger, S., Dentener, F., Krol, M., Jeuken, A., and Lelieveld, J.: Gas/aerosol partitioning 2. Global modeling results, J. Geophys. Res.-Atmos., 107, 1–23, https://doi.org/10.1029/2001JD001103, 2002b.

Moore, R. H., Karydis, V. A., Capps, S. L., Lathem, T. L., and Nenes, A.: Droplet number uncertainties associated with CCN: an assessment using observations and a global model adjoint, Atmos. Chem. Phys., 13, 4235–4251, https://doi.org/10.5194/acp-13-4235-2013, 2013.

Morales Betancourt, R. and Nenes, A.: Characteristic updrafts for computing distribution-averaged cloud droplet number and stratocumulus cloud properties, J. Geophys. Res.-Atmos., 115, 2–9, https://doi.org/10.1029/2009JD013233, 2010.

Morales Betancourt, R. and Nenes, A.: Understanding the contributions of aerosol properties and parameterization discrepancies to droplet number variability in a global climate model, Atmos. Chem. Phys., 14, 4809–4826, https://doi.org/10.5194/acp-14-4809-2014, 2014a.

Morales Betancourt, R. and Nenes, A.: Droplet activation parameterization: the population-splitting concept revisited, Geosci. Model Dev., 7, 2345–2357, https://doi.org/10.5194/gmd-7-2345-2014, 2014b.

Myhre, G., Samset, B. H., Schulz, M., Balkanski, Y., Bauer, S., Berntsen, T. K., Bian, H., Bellouin, N., Chin, M., Diehl, T., Easter, R. C., Feichter, J., Ghan, S. J., Hauglustaine, D., Iversen, T., Kinne, S., Kirkevåg, A., Lamarque, J.-F., Lin, G., Liu, X., Lund, M. T., Luo, G., Ma, X., van Noije, T., Penner, J. E., Rasch, P. J., Ruiz, A., Seland, Ø., Skeie, R. B., Stier, P., Takemura, T., Tsigaridis, K., Wang, P., Wang, Z., Xu, L., Yu, H., Yu, F., Yoon, J.-H., Zhang, K., Zhang, H., and Zhou, C.: Radiative forcing of the direct aerosol effect from AeroCom Phase II simulations, Atmos. Chem. Phys., 13, 1853–1877, https://doi.org/10.5194/acp-13-1853-2013, 2013.

Myriokefalitakis, S., Nenes, A., Baker, A. R., Mihalopoulos, N., and Kanakidou, M.: Bioavailable atmospheric phosphorous supply to the global ocean: a 3-D global modeling study, Biogeosciences, 13, 6519–6543, https://doi.org/10.5194/bg-13-6519-2016, 2016.

Nenes, A. and Seinfeld, J. H.: Parameterization of cloud droplet formation in global climate models, J. Geophys. Res.-Atmos., 108, 4415, https://doi.org/10.1029/2002JD002911, 2003.

Ovadnevaite, J., Ceburnis, D., Leinert, S., Dall'Osto, M., Canagaratna, M., O'Doherty, S., Berresheim, H., and O'Dowd, C.: Submicron NE Atlantic marine aerosol chemical composition and abundance: Seasonal trends and air mass categorization, J. Geophys. Res.-Atmos., 119, 11850–11863, https://doi.org/10.1002/2013JD021330, 2014.

Petters, M. D. and Kreidenweis, S. M.: A single parameter representation of hygroscopic growth and cloud condensation nucleus activity, Atmos. Chem. Phys., 7, 1961–1971, https://doi.org/10.5194/acp-7-1961-2007, 2007.

Pierce, J. R., Riipinen, I., Kulmala, M., Ehn, M., Petäjä, T., Junninen, H., Worsnop, D. R., and Donahue, N. M.: Quantification of the volatility of secondary organic compounds in ultrafine particles during nucleation events, Atmos. Chem. Phys., 11, 9019–9036, https://doi.org/10.5194/acp-11-9019-2011, 2011.

Pringle, K. J., Tost, H., Pozzer, A., Pöschl, U., and Lelieveld, J.: Global distribution of the effective aerosol hygroscopicity parameter for CCN activation, Atmos. Chem. Phys., 10, 5241–5255, https://doi.org/10.5194/acp-10-5241-2010, 2010.

Pruppacher, H. R. and Klett, J. D.: Microphysics of clouds and precipitation, 2nd ed., Kluwer Academic Publishers, Dordrecht, The Netherlands, 1997.

Reutter, P., Su, H., Trentmann, J., Simmel, M., Rose, D., Gunthe, S. S., Wernli, H., Andreae, M. O., and Pöschl, U.: Aerosol- and updraft-limited regimes of cloud droplet formation: influence of particle number, size and hygroscopicity on the activation of cloud condensation nuclei (CCN), Atmos. Chem. Phys., 9, 7067–7080, https://doi.org/10.5194/acp-9-7067-2009, 2009.

Riccobono, F., Schobesberger, S., Scott, C. E., Dommen, J., Ortega, I. K., Rondo, L., Almeida, J., Amorim, A., Bianchi, F., Breitenlechner, M., David, A., Downard, A., Dunne, E. M., Duplissy, J., Ehrhart, S., Flagan, R. C., Franchin, A., Hansel, A., Junninen, H., Kajos, M., Keskinen, H., Kupc, A., Kürten, A., Kvashin, A. N., Laaksonen, A., Lehtipalo, K., Makhmutov, V., Mathot, S., Nieminen, T., Onnela, A., Petäjä, T., Praplan, A. P., Santos, F. D., Schallhart, S., Seinfeld, J. H., Sipilä, M., Spracklen, D. V, Stozhkov, Y., Stratmann, F., Tomé, A., Tsagkogeorgas, G., Vaattovaara, P., Viisanen, Y., Vrtala, A., Wagner, P. E., Weingartner, E., Wex, H., Wimmer, D., Carslaw, K. S., Curtius, J., Donahue, N. M., Kirkby, J., Kulmala, M., Worsnop, D. R., and Baltensperger, U.: Oxidation Products of Biogenic Emissions Contribute to Nucleation of Atmospheric Particles, Science, 80, 717–721, 2014.

Rissman, T., Nenes, A., and Seinfeld, J. H.: Chemical amplification (or dampening) of the Twomey effect: Conditions derived from droplet activation theory, J. Atmos. Sci., 61, 919–930, 2004.

Schmale, J., Henning, S., Henzing, B., Keskinen, H., Sellegri, K., Ovadnevaite, J., Bougiatioti, A., Kalivitis, N., Stavroulas, I., Jefferson, A., Park, M., Schlag, P., Kristensson, A., Iwamoto, Y., Pringle, K., Reddington, C., Aalto, P., Äijälä, M., Baltensperger, U., Bialek, J., Birmili, W., Bukowiecki, N., Ehn, M., Fjæraa, A. M., Fiebig, M., Frank, G., Fröhlich, R., Frumau, A., Furuya, M., Hammer, E., Heikkinen, L., Herrmann, E., Holzinger, R., Hyono, H., Kanakidou, M., Kiendler-Scharr, A., Kinouchi, K., Kos, G., Kulmala, M., Mihalopoulos, N., Motos, G., Nenes, A., O'Dowd, C., Paramonov, M., Petäjä, T., Picard, D., Poulain, L., Prévôt, A. S. H., Slowik, J., Sonntag, A., Swietlicki, E., Svenningsson, B., Tsurumaru, H., Wiedensohler, A., Wittbom, C., Ogren, J. A., Matsuki, A., Yum, S. S., Myhre, C. L., Carslaw, K., Stratmann, F., and Gysel, M.: Collocated observations of cloud condensation nuclei, particle size distributions, and chemical composition, Sci. Data, 4, 170003, https://doi.org/10.1038/sdata.2017.3, 2017.

Schmale, J., Henning, S., Decesari, S., Henzing, B., Keskinen, H., Sellegri, K., Ovadnevaite, J., Pöhlker, M. L., Brito, J., Bougiatioti, A., Kristensson, A., Kalivitis, N., Stavroulas, I., Carbone, S., Jefferson, A., Park, M., Schlag, P., Iwamoto, Y., Aalto, P., Äijälä, M., Bukowiecki, N., Ehn, M., Frank, G., Fröhlich, R., Frumau, A., Herrmann, E., Herrmann, H., Holzinger, R., Kos, G., Kulmala, M., Mihalopoulos, N., Nenes, A., O'Dowd, C., Petäjä, T., Picard, D., Pöhlker, C., Pöschl, U., Poulain, L., Prévôt, A. S. H., Swietlicki, E., Andreae, M. O., Artaxo, P., Wiedensohler, A., Ogren, J., Matsuki, A., Yum, S. S., Stratmann, F., Baltensperger, U., and Gysel, M.: Long-term cloud condensation nuclei number concentration, particle number size distribution and chemical composition measurements at regionally representative observatories, Atmos. Chem. Phys., 18, 2853–2881, https://doi.org/10.5194/acp-18-2853-2018, 2018.

Schutgens, N. A. J., Gryspeerdt, E., Weigum, N., Tsyro, S., Goto, D., Schulz, M., and Stier, P.: Will a perfect model agree with perfect observations? The impact of spatial sampling, Atmos. Chem. Phys., 16, 6335–6353, https://doi.org/10.5194/acp-16-6335-2016, 2016.

Seinfeld, J. and Pandis, S.: Atmospheric Chemistry and Physics: From Air Pollution to Climate Change, J. Wiley, New York, 2006.

Seinfeld, J. H., Bretherton, C., Carslaw, K. S., Coe, H., DeMott, P. J., Dunlea, E. J., Feingold, G., Ghan, S., Guenther, A. B.,

Kahn, R., Kraucunas, I., Kreidenweis, S. M., Molina, M. J., Nenes, A., Penner, J. E., Prather, K. A., Ramanathan, V., Ramaswamy, V., Rasch, P. J., Ravishankara, A. R., Rosenfeld, D., Stephens, G., and Wood, R.: Improving our fundamental understanding of the role of aerosol−cloud interactions in the climate system, P. Natl. Acad. Sci. USA, 113, 5781–5790, https://doi.org/10.1073/pnas.1514043113, 2016.

Sotiropoulou, R.-E. P., Medina, J., and Nenes, A.: CCN predictions: Is theory sufficient for assessments of the indirect effect?, Geophys. Res. Lett., 33, L05816, https://doi.org/10.1029/2005GL025148, 2006.

Sotiropoulou, R. E. P., Nenes, A., Adams, P. J., and Seinfeld, J. H.: Cloud condensation nuclei prediction error from application of Köhler theory: Importance for the aerosol indirect effect, J. Geophys. Res.-Atmos., 112, D12202, https://doi.org/10.1029/2006JD007834, 2007.

Spracklen, D. V., Bonn, B., and Carslaw, K. S.: Boreal forests, aerosols and the impacts on clouds and climate, Philos. Trans. A. Math. Phys. Eng. Sci., 366, 4613–26, https://doi.org/10.1098/rsta.2008.0201, 2008.

Spracklen, D. V., Carslaw, K. S., Pöschl, U., Rap, A., and Forster, P. M.: Global cloud condensation nuclei influenced by carbonaceous combustion aerosol, Atmos. Chem. Phys., 11, 9067–9087, https://doi.org/10.5194/acp-11-9067-2011, 2011.

Spracklen, D. V., Carslaw, K. S., Merikanto, J., Mann, G. W., Reddington, C. L., Pickering, S., Ogren, J. A., Andrews, E., Baltensperger, U., Weingartner, E., Boy, M., Kulmala, M., Laakso, L., Lihavainen, H., Kivekäs, N., Komppula, M., Mihalopoulos, N., Kouvarakis, G., Jennings, S. G., O'Dowd, C., Birmili, W., Wiedensohler, A., Weller, R., Gras, J., Laj, P., Sellegri, K., Bonn, B., Krejci, R., Laaksonen, A., Hamed, A., Minikin, A., Harrison, R. M., Talbot, R., and Sun, J.: Explaining global surface aerosol number concentrations in terms of primary emissions and particle formation, Atmos. Chem. Phys., 10, 4775–4793, https://doi.org/10.5194/acp-10-4775-2010, 2010.

Sullivan, R. C., Moore, M. J. K., Petters, M. D., Kreidenweis, S. M., Roberts, G. C., and Prather, K. A.: Effect of chemical mixing state on the hygroscopicity and cloud nucleation properties of calcium mineral dust particles, Atmos. Chem. Phys., 9, 3303–3316, https://doi.org/10.5194/acp-9-3303-2009, 2009.

Sullivan, S. C., Lee, D., Oreopoulos, L., and Nenes, A.: Role of updraft velocity in temporal variability of global cloud hydrometeor number, P. Natl. Acad. Sci. USA, 113, 5791–5796, https://doi.org/10.1073/pnas.1514039113, 2016.

Tegen, I., Neubauer, D., Ferrachat, S., Siegenthaler-Le Drian, C., Bey, I., Schutgens, N., Stier, P., Watson-Parris, D., Stanelle, T., Schmidt, H., Rast, S., Kokkola, H., Schultz, M., Schroeder, S., Daskalakis, N., Barthel, S., Heinold, B., and Lohmann, U.: The global aerosol–climate model ECHAM6.3–HAM2.3 – Part 1: Aerosol evaluation, Geosci. Model Dev., 12, 1643–1677, https://doi.org/10.5194/gmd-12-1643-2019, 2019.

Textor, C., Schulz, M., Guibert, S., Kinne, S., Balkanski, Y., Bauer, S., Berntsen, T., Berglen, T., Boucher, O., Chin, M., Dentener, F., Diehl, T., Easter, R., Feichter, H., Fillmore, D., Ghan, S., Ginoux, P., Gong, S., Grini, A., Hendricks, J., Horowitz, L., Huang, P., Isaksen, I., Iversen, I., Kloster, S., Koch, D., Kirkevåg, A., Kristjansson, J. E., Krol, M., Lauer, A., Lamarque, J. F., Liu, X., Montanaro, V., Myhre, G., Penner, J., Pitari, G., Reddy, S., Seland, Ø., Stier, P., Takemura, T., and Tie, X.: Analysis and quantification of the diversities of aerosol life cycles within AeroCom, Atmos. Chem. Phys., 6, 1777–1813, https://doi.org/10.5194/acp-6-1777-2006, 2006.

Tröstl, J., Chuang, W. K., Gordon, H., Heinritzi, M., Yan, C., Molteni, U., Ahlm, L., Frege, C., Bianchi, F., Wagner, R., Simon, M., Lehtipalo, K., Williamson, C., Craven, J. S., Duplissy, J., Adamov, A., Almeida, J., Bernhammer, A. K., Breitenlechner, M., Brilke, S., Dias, A., Ehrhart, S., Flagan, R. C., Franchin, A., Fuchs, C., Guida, R., Gysel, M., Hansel, A., Hoyle, C. R., Jokinen, T., Junninen, H., Kangasluoma, J., Keskinen, H., Kim, J., Krapf, M., Kürten, A., Laaksonen, A., Lawler, M., Leiminger, M., Mathot, S., Möhler, O., Nieminen, T., Onnela, A., Petäjä, T., Piel, F. M., Miettinen, P., Rissanen, M. P., Rondo, L., Sarnela, N., Schobesberger, S., Sengupta, K., Sipilä, M., Smith, J. N., Steiner, G., Tomè, A., Virtanen, A., Wagner, A. C., Weingartner, E., Wimmer, D., Winkler, P. M., Ye, P., Carslaw, K. S., Curtius, J., Dommen, J., Kirkby, J., Kulmala, M., Riipinen, I., Worsnop, D. R., Donahue, N. M., and Baltensperger, U.: The role of low-volatility organic compounds in initial particle growth in the atmosphere, Nature, 533, 527–531, https://doi.org/10.1038/nature18271, 2016.

Tsigaridis, K., Koch, D., and Menon, S.: Uncertainties and importance of sea spray composition on aerosol direct and indirect effects, J. Geophys. Res.-Atmos., 118, 220–235, https://doi.org/10.1029/2012JD018165, 2013.

Tsigaridis, K., Daskalakis, N., Kanakidou, M., Adams, P. J., Artaxo, P., Bahadur, R., Balkanski, Y., Bauer, S. E., Bellouin, N., Benedetti, A., Bergman, T., Berntsen, T. K., Beukes, J. P., Bian, H., Carslaw, K. S., Chin, M., Curci, G., Diehl, T., Easter, R. C., Ghan, S. J., Gong, S. L., Hodzic, A., Hoyle, C. R., Iversen, T., Jathar, S., Jimenez, J. L., Kaiser, J. W., Kirkevåg, A., Koch, D., Kokkola, H., Lee, Y. H., Lin, G., Liu, X., Luo, G., Ma, X., Mann, G. W., Mihalopoulos, N., Morcrette, J.-J., Müller, J.-F., Myhre, G., Myriokefalitakis, S., Ng, N. L., O'Donnell, D., Penner, J. E., Pozzoli, L., Pringle, K. J., Russell, L. M., Schulz, M., Sciare, J., Seland, Ø., Shindell, D. T., Sillman, S., Skeie, R. B., Spracklen, D., Stavrakou, T., Steenrod, S. D., Takemura, T., Tiitta, P., Tilmes, S., Tost, H., van Noije, T., van Zyl, P. G., von Salzen, K., Yu, F., Wang, Z., Wang, Z., Zaveri, R. A., Zhang, H., Zhang, K., Zhang, Q., and Zhang, X.: The AeroCom evaluation and intercomparison of organic aerosol in global models, Atmos. Chem. Phys., 14, 10845–10895, https://doi.org/10.5194/acp-14-10845-2014, 2014.

Twomey, S.: The nuclei of natural cloud formation. II The supersaturation in natural clouds and the variation of cloud droplet concentration, Geofis. Pura Appl., 43, 243–249, 1959.

Twomey, S.: The Influence of Pollution on the Shortwave Albedo of Clouds, J. Atmos. Sci., 34, 1149—1152, https://doi.org/10.1175/1520-0469(1977)034<1149:TIOPOT>2.0.CO;2, 1977.

Vehkamäki, H.: An improved parameterization for sulfuric acid–water nucleation rates for tropospheric and stratospheric conditions, J. Geophys. Res., 107, 4622, https://doi.org/10.1029/2002JD002184, 2002.

Vignati, E., Wilson, J., and Stier, P.: M7: An efficient size-resolved aerosol microphysics module for large-scale aerosol transport models, J. Geophys. Res.-Atmos., 109, D22202, https://doi.org/10.1029/2003JD004485, 2004.

Wang, H., Easter, R. C., Rasch, P. J., Wang, M., Liu, X., Ghan, S. J., Qian, Y., Yoon, J.-H., Ma, P.-L., and Vinoj, V.: Sensitivity of remote aerosol distributions to representation of cloud–aerosol interactions in a global climate model, Geosci. Model Dev., 6, 765–782, https://doi.org/10.5194/gmd-6-765-2013, 2013.

Yoshioka, M., Regayre, L. A., Pringle, K. J., Johnson, J. S., Mann, G. W., Partridge, D. G., Sexton, D. M. H., Lister, G. M. S., Schutgens, N.,Stier, P., Kipling, Z., Bellouin, N., Browse, J., Booth, B. B. B., Johnson, C. E.,Johnson, B., Mollard, J. D. P., Lee, L., and Carslaw, K. S.: Ensembles of Global Climate Model Variants Designed for the Quantification and Constraint of Uncertainty in Aerosols and their Radiative Forcing, J. Adv. Model. Earth Syst., under review, 2019.

Yu, F.: A secondary organic aerosol formation model considering successive oxidation aging and kinetic condensation of organic compounds: global scale implications, Atmos. Chem. Phys., 11, 1083–1099, https://doi.org/10.5194/acp-11-1083-2011, 2011.

Yu, F. and Luo, G.: Simulation of particle size distribution with a global aerosol model: contribution of nucleation to aerosol and CCN number concentrations, Atmos. Chem. Phys., 9, 7691–7710, https://doi.org/10.5194/acp-9-7691-2009, 2009.

Yu, F., Nadykto, A. B., Herb, J., Luo, G., Nazarenko, K. M., and Uvarova, L. A.: $H_2SO_4-H_2O-NH_3$ ternary ion-mediated nucleation (TIMN): kinetic-based model and comparison with CLOUD measurements, Atmos. Chem. Phys., 18, 17451–17474, https://doi.org/10.5194/acp-18-17451-2018, 2018.

Supplement of Atmos. Chem. Phys., 19, 8591–8617, 2019
https://doi.org/10.5194/acp-19-8591-2019-supplement


Atmospheric Chemistry and Physics
Open Access
EGU

*Supplement of*

# Evaluation of global simulations of aerosol particle and cloud condensation nuclei number, with implications for cloud droplet formation

**George S. Fanourgakis et al.**

*Correspondence to:* Maria Kanakidou (mariak@uoc.gr) and Athanasios Nenes (athanasios.nenes@epfl.ch)

Table of Contents

## Appendix S1. Models and measurements description

## Details on aerosol microphysics representation in the participating models (Tables S1, S2, S3):

The original M7 scheme (Vignati et al., 2004) uses seven log-normal distributions to represent aerosol populations. Four of them are describing mixed (water-soluble) particles, in the nucleation, Aitken, accumulation and coarse modes, while the remaining three modes include insoluble particles in the Aitken, accumulation and coarse modes. Each mode is represented by the total number concentration of particles and the mass mixing ratio of each aerosol component. Soluble particles are formed from insoluble ones by coagulation and condensation.

With respect to the original M7 scheme, ECHAM5.5-HAM2-ELVOC_UH and TM4-ECPL are using an improved numerical scheme (Kokkola et al., 2009) to compute the formation of sulfuric acid by oxidation of $SO_2$, and its removal by nucleation and condensation on pre-existing particles. The EMAC model uses the Global Modal-aerosol eXtension (GMXe) microphysics model (Pringle et al., 2010a), which is also based on M7 and allows the treatment of additional aerosol species (sodium, chloride, magnesium, calcium, and potassium).

The ECHAM5.5-HAM2-ELVOC_UH, ECHAM6-HAM2-AP and ECHAM6-HAM2 models are using the same aerosol module HAM2 (Zhang et al., 2012; Tegen et al, 2018). Secondary organic aerosols (SOA) produced by oxidation of isoprene, monoterpene, and anthropogenic precursors and primary organic aerosols (POA) are treated as different tracers within the HAM2-ELVOC-UH module, while in ECHAM6-HAM2 and ECHAM6-HAM2-AP SOA is added to POA (see Tables S2 and S3). ECHAM6-HAM2-AP is identical to ECHAM6-HAM2 with the difference that the aerosol processing (AP) scheme in stratiform clouds by Neubauer et al. (2014) is used, which is adapted from Hoose et al. (2008a, 2008b). In addition to the seven modes in ECHAM6-HAM2, ECHAM6-HAM2-AP has an explicit representation of aerosol particles in cloud droplets and ice crystals in stratiform clouds, which are represented by 5 tracers (sulphate – SO4, black carbon - BC, organic aerosol - OA, dust- DU and sea-salt- SS). Nucleation and impaction scavenging of aerosols, freezing and evaporation of cloud droplets, and melting and sublimation of ice crystals are treated explicitly. Aerosol particles from evaporating precipitation are released to modes, which correspond to their size and can therefore act as CCN or INP again.

The TM4-ECPL model also treats POA and SOA separately. The latter are produced from semi-volatile organics formed by oxidation of isoprene, terpene (a- and b- pinenes) and aromatic (benzene, toluene and xylene) compounds (Tsigaridis and Kanakidou, 2003; Tsigaridis and Kanakidou, 2007) as well as by aqueous phase chemistry (Myriokefalitakis et al., 2011). For this study, although TM4-ECPL uses ISORROPIA II thermodynamic model (Fountoukis and Nenes, 2007) to calculate the partitioning between $HNO_3$ and $NO_3^-$, the contribution of particulate $NO_3^-$ to aerosol formation and growth is not taken into account.

TM5 uses a similar host model as TM4-ECPL. TM5 considers SOA formation from isoprene and monoterpenes. SOA formation mechanism is implemented according to Jokinen et al. (2015). Both monoterpenes and isoprene produce extremely low volatility organic compounds (ELVOCs) and semi-volatile products with prescribed yields (from Jokinen et al., 2015). Oxidation by OH and $O_3$ is considered. The ELVOCs participate in aerosol nucleation, which is parameterized

according to Riccobono et al. (2014) accounting for sulfuric acid and organic vapors. In addition, ELVOCs in TM5 provide early growth for nucleation mode particles, as they are distributed to particle phase according to condensation sink. The semi-volatile products are distributed to particle phase according to particle-phase organic mass, as in Jokinen et al. (2015). Hence, after oxidation, no SOA products remain in the gas-phase, but immediate condensation to aerosol-phase is assumed. The approach provides dynamics for aerosol mass and number formation, but does not consider e.g. particle-phase reactions, evaporation of organic material, or aqueous-phase SOA formation. More detailed description can be found in Bergman et al. (in prep.)

CAM5-MAM3 employs the three-mode modal aerosol module MAM3 (Liu et al., 2012). Within each of the three modes (Aitken, accumulation, and coarse mode) all types of aerosols are internally mixed, while particles between different modes are externally mixed. SO4, BC, POA, SOA, SS, DU are the aerosol components considered using a total of 15 aerosol tracers. CAM5-MAM4 has an extra primary-carbon mode to treat freshly emitted POA and BC, amounting to in total 18 aerosol tracers (Liu et al., 2016). The MAM3 and MAM4 aerosol modules describe the following microphysical processes: nucleation, condensation, coagulation, ageing, dry (gravitational and turbulent) deposition, wet (in-cloud and below-cloud scavenging) deposition, in-cloud activation, and release from the evaporation of clouds and raindrops.

Two of the global models (GEOS-Chem-APM and CAM5-Chem-APM) are using the sectional Advanced Particle Microphysics (APM) package (Yu and Luo, 2009). The APM package is optimized to accurately simulate secondary particles (composed of SO4, NO3, NH4, and SOA) formation and their growth to CCN sizes, with a higher size resolution for the size range of importance (1.2–120 nm: 30 bins, 10 additional bins for 120 nm–12 μm). 20 sectional bins represent sea salt, covering dry diameters from 0.012 to 12 μm, and 15 sectional bins represent dust for 0.03–50 μm. Two modes (Aitken mode and accumulation mode) are used in this study to represent hydrophobic and hydrophilic BC and POC in the model. APM also considers the aging of BC and OA that turns the hydrophobic BC and OA to hydrophilic. Coating of SO4 and other secondary aerosols on primary particles such as BC, OA, SS, and DU are considered. The contribution of nitrate, ammonium, and SOA to SO4 particle growth are considered. Via the coating process caused by coagulation, condensation, and in-cloud oxidation, some secondary species attach to primary particles and are transported and scavenged with these primary particles. The kinetic condensation of low volatile secondary organic gas (LV-SOG) in addition to sulfuric acid on nucleated particles is calculated based on a scheme that considers the SOG volatility changes arising from the oxidation aging (Yu, 2011).

TwO-Moment Aerosol Sectional (TOMAS) microphysics package (Adams and Seinfeld, 2002; Lee and Adams, 2012) was used by the GISS-E2-TOMAS (Lee et al., 2015) and GEOS-Chem-TOMAS (Kodros et al., 2016) global models. Both models simulate SO4, SS, OA, BC and DU. In GEOS-Chem-TOMAS, TOMAS tracks two independent moments (number and mass) within each of 15 size sections for size-resolved condensation, coagulation, nucleation, dry deposition, wet deposition, emissions, and aqueous chemistry. Condensation includes sulfuric acid and SOA (including both biogenic SOA and anthropogenically enhanced SOA as described in D'Andrea et al., 2013). GEOS-Chem-TOMAS accounts for binary (Vehkamaki et al., 2002) and ammonia ternary (Napari et al., 2002) nucleation, where ternary nucleation rates are scaled

down by a factor of 105 to match observed nucleation rates (Westervelt et al., 2013). TOMAS has also been integrated into GISS-E2 (Lee et al., 2015), a fully coupled Earth System Model with interactive atmosphere, land, ocean, and sea ice components (Schmidt et al., 2014). TOMAS in GISS-E2 consists of 15 size sections covering 3 nm to 10 μm. Condensation in GISS-E2-TOMAS includes both sulfuric acid and a simpler treatment of SOA than is present in GEOS-Chem-TOMAS, in which 10% of terpene emissions are condensed as hydrophilic organic aerosol, resulting in a production rate of 17.1 Tg $a^{-1}$. GISS-E2-TOMAS uses a physically-based aerosol-cloud activation parameterization from Nenes and Seinfeld (2003), using both modeled large-scale and sub-grid updraft velocity.

The Multiconfiguration Aerosol TRacker of mIXing state (MATRIX) module (Bauer et al., 2008; 2010; Bauer and Menon, 2012) is used by GISS-E2.1-MATRIX. MATRIX is an aerosol microphysics scheme based on the quadrature method of moments (QMOM; McGraw, 1997). MATRIX represents new particle formation (binary and ternary nucleation), particle emissions, gas-particle mass transfer, aerosol phase chemistry, condensational growth, and coagulation within and between particle populations. Condensational growth is calculated for the sulphate-ammonium-nitrate-water system. Unique to MATRIX is the ability to explicitly simulate aerosol mixing state (Bauer et al., 2013). For this study MATRIX is set up with 16 aerosol populations, as defined by their mixing state. The tracked variables vary by population but can include number concentration and mass concentration of SO4, NO3, NH4, aerosol water, BC, OA, mineral dust, and SS. MATRIX is coupled to the NASA GISS climate model, GISS-E2.1, an updated version of GISS-E2 model (Schmidt et al., 2014). Sea-salt, dust and isoprene emission fluxes are calculated interactively, and additional natural and anthropogenic fluxes are from the CMIP6 inventory (Hoesly et al., 2017; van Marle et al., 2017).

The CAM5-chem-ATRAS2 is using the Aerosol Two-dimensional bin module for foRmation and Aging Simulation version 2 (ATRAS2) (Matsui, 2017; Matsui and Mahowald, 2017). The ATRAS2 model uses 12 size bins from 0.001 to 10 μm in aerosol dry diameter. BC mixing state is resolved with 8, 3, or 1 bins for each size bin. In this study, we perform simulations with a single mixing state representation. Mass concentrations of eight aerosol species (SO4, NO3, NH4, DU, SS, OA (POA+SOA), BC, and water) and number concentrations are calculated for each bin in the model. The number of advected species (chemistry and aerosol) is 215 in this study. The CAM5-chem-ATRAS2 model considers emissions, gas-phase chemistry, condensation and evaporation of SO4, NO3, NH4, and OA, coagulation, nucleation, activation of aerosol and evaporation from cloud, aerosol formation in clouds, dry and wet deposition, aerosol optical properties, aerosol-radiation interactions, and aerosol-cloud interactions. OA formation is calculated by a volatility basis-set approach which considers oxidations of POA (gas-phase), alkanes, alkenes, aromatics, isoprene, and monoterpene (Matsui et al., 2014; Matsui, 2017). Nucleation is calculated by the activation-type theory (Kulmala et al., 2006) within the planetary boundary layer and by a binary homogeneous nucleation scheme (Vehkamäki et al., 2002) within the free troposphere.

CAM5.3-Oslo (Kirkevåg et al., 2018; Karset et al., 2018) includes a “production tagged” aerosol life-cycle module (OsloAero5.3), and comes with an offline microphysics scheme (AeroTab5.3), which is used to make look-up tables for aerosol optics and dry sizes. In AeroTab5.3, the size distributions of number and mass concentrations are estimated by solving the respective continuity equations, using 44 size bins with radii ranging from 0.001 to 20 μm. The size modes are

assumed to be log-normally distributed at the point of emission or nucleation, but are modified by condensation, coagulation, and cloud processing. The term “production-tagged” is used since the tracers that change the aerosol size distributions are tagged according to their production pathway (e.g., condensation). In the aerosol life-cycle module, scavenging and dry deposition also change the total size distribution, but not the shape/radius-dependence of each of the size modes. The size modes are here assumed to be log-normal, either with prescribed typical sizes, or with log-normal fits (through look-up tables, for use in the CCN activation) to the respective size distributions calculated offline. In total 21 aerosol tracers are taken into account, distributed onto 10 internally mixed and 2 externally mixed (except with water through hygroscopic growth) size-modes, consisting of SO4, SS, OC, BC, and DU.

HadGEM3-UKCA includes the GLOMAP modal aerosol scheme, which is a two-moment scheme representing seven (7) lognormal modes; soluble nucleation, Aitken, accumulation and coarse modes and insoluble Aitken, accumulation and coarse modes. Each of these modes carries particle numbers and masses for 5 aerosol components; SO4, BC, OC (including both primary and secondary aerosols), DU and SS. Insoluble mode particles can be aged and become soluble when soluble secondary aerosol materials condense on them and form coating. In the lowermost atmosphere particles are subject to dry deposition. All particles are also subject to impaction scavenging by rainfall, while soluble particles are in addition subject to nucleation scavenging in large scale and convective rainfall.

**Table S1. Host model description**

| Model | Horizontal resolution (latitude × longitude) | Vertical resolution | Host Model | Meteorology | Model references |
|---|---|---|---|---|---|
| CAM5-Chem-APM | 1.875° × 2.5° | 32 | GCM | Online, Nudged with MERRA2 | (Luo and Yu, 2018 in prep.) |
| CAM5-Chem-ATRAS2 | 1.875° × 2.5° | 30 up to 3.6 hPa | GCM (nudged) | MERRA U and V (6h) | (Matsui, 2017) (Matsui and Mahowald, 2017) |
| CAM5_MAM3 | 1.875° × 2.5° | 30 up to 3.6 hPa | GCM (nudg) | MERRA U and V (6h) | (Neale et al., 2012) (Wang et al., 2013), (Yang et al., 2017) |
| CAM5_MAM4 | 1.875° × 2.5° | 56 up to 40 Km | GCM (nudged) | MERRA | (Neale et al., 2012) (Wang et al., 2013), (Yang et al., 2017) |
| CAM5.3-Oslo | 0.938° × 1.25° | 30 up to 3.6 hPa | GCM (nudg) | ERA-interim U, V and PS (6h) | (Kirkevåg et al., 2018); (Karset et al., 2018) |
| ECHAM5.5-HAM2-ELVOC_UH | 1.875° × 1.875° | 31 (hybrid sigma) | GCM (nudg) | ERA-Interim, U, V, PS | (Zhang et al., 2012); (Jokinen et al., 2015) |
| ECHAM6-HAM2 | 1.875° × 1.875° | 31 (hybrid sigma) to 10 hPa | GCM (nudg) | ERA-interim DIV (48h), VOR (6h) and PS (24h) | (Stevens et al., 2013), (Tegen et al., 2019), (Lohman and Neubauer , 2018) |
| ECHAM6-HAM2-AP | 1.875° × 1.875° | 31 (hybrid sigma) to 10hPa | GCM (nudg) | ERA-interim DIV (48h), VOR (6h) and PS (24h) | (Stevens et al., 2013); (Tegen et al., 2019); (Neubauer et al., 2018) |
| EMAC | 1.875° × 1.875° | 31 (hybrid sigma) | GCM (nudg) | ERA-interim DIV (48h), VOR (6h) and PS (24h) | (Jöckel et al., 2010); (Karydis et al., 2017) |
| GEOS-Chem-APM | 2° × 2.5° | 38 | CTM | MERRA2 | (Yu and Luo, 2009), (Yu, 2011) |
| GEOS-Chem-TOMAS | 4.0° × 5.0° | 25 | CTM | MERRA | (Bey et al., 2001a) (http://acmg.seas.harvard.edu/geos/) |
| GISS-E2.1-MATRIX | 2° x 2.5° | 40 | GCM (nudg) | NCEP | (Bauer et al., 2008) |
| GISS-E2-Tomas | 2° x 2.5° | 40 | GISS GCM (free-running) | Online | (Lee et al., 2015) |
| TM4-ECPL and TM4-ECPL/v | 2° x 3° | 34 (hybrid sigma) to 0.1 hPa | TM4, CTM | ECMWF ERA-interim | (Kanakidou et al., 2012), (Daskalakis et al., 2015) |
| TM5 | 2° x 3° | 34 (hybrid sigma) to 0.1 hPa | TM5, CTM | ECMWF ERA-Interim | (Van Noije et al., 2014), (Huijnen et al., 2010); (Bergman et al., 2018, in prep.) |

## Table S2. Details about the microphysics schemes employed by the models.

| MODEL | Microphysics Scheme | Scheme Type | Number of bins or modes | Reference | Aerosol components | Nucleation Scheme |
|---|---|---|---|---|---|---|
| **CAM5-chem-APM** | APM | Sectional (2m) | 40 | To be published | SO4, NO3, NH4, SOA, SS, DU, BC, POA | Ternary ion-mediated nucleation (Yu et al., 2018) |
| **CAM5-chem-ATRAS2** | ATRAS2 | Sectional (2m) | 12 (47 in maximum) | (Matsui, 2017) (Matsui and Mahowald, 2017) | SO4, NO3, NH4, OA (POA, SOA), SS, DU, BC | (Kulmala et al., 2006) within the planetary boundary later (Vehkamäki et al. 2002) within the free troposphere |
| **CAM5_MAM3** | MAM3 | Modal (2m) | 3 | (Liu et al., 2012) | SO4, BC, DU, SS, OA (POA+SOA) | (Vehkamäki, 2002) |
| **CAM5_MAM4** | MAM4 | Modal (2m) | 4 | (Liu et al., 2012) (Liu et al., 2016) | SO4, BC, DU, SS, POA+SOA | (Vehkamäki, 2002) . The boundary layer parameterization, (only applied in PBL), uses the empirical first order (in $H_2SO_4$) nucleation rate from (Sihto et al., 2006) |
| **CAM5.3-Oslo** | OsloAero5.3 with look-up tables from AeroTab5.3 (offline) | Production-tagged (linked to an offline 2m Sectional scheme) | 44 (offline) | {Kirkevåg et al., 2018} | SO4, BC, DU, SS, OA (POA+SOA), distributed over 12 external and internal mixtures (size-modes) | (Vehkamäki, 2002), (Paasonen et al., 2010) |
| **ECHAM5.5-HAM2-ELVOC_UH** | HAM2 | Modal (2m) | 7 | (Zhang et al., 2012) | SO4, BC, DU, SS, OA (POA+SOA) SOA as in (Joniken et al., 2015) | (Vehkamäki, 2002) (Paasonen et al., 2010) |
| **ECHAM6-HAM2** | HAM2 | Modal (2m) | 7 | (Tegen et al. 2019); (Neubauer et al, 2018), (Zhang et al., 2012) | SO4, BC, DU, SS, OA (POA+SOA) SOA: approximated as 15% of monoterpene emissions at the surface. SOA is assumed to condense immediately on existing aerosol particles and to have identical properties to primary organic aerosols | (Kazil et al., 2010); |
| **ECHAM6-HAM2-AP** | AP | Modal (2m) | 7+2 | (Tegen et al., 2019) ; (Neubauer et al., 2014) based on (Hoose et al., 2008a, 2008b) | SO4, BC, DU, SS, OA (POA+SOA) SOA: as in ECHAM6-HAM2 | (Kazil and Lovejoy, 2007); (Kazil et al., 2010); (Kulmala et al., 2006) |
| **EMAC** | GMXe | Modal (2m) | 7 | (Pringle et al., 2010a) (Pringle et al., 2010b) | Thermodynamic equilibrium using ISORROPIA-II (Fountoukis and Nenes, 2007) Species considered: $K^+$-$Ca^{2+}$-$Mg^{2+}$-$NH_4^+$-$Na^+$-$SO_4^{-2}$-$NO_3^-$-$Cl^-$-$H_2O$-BC-OA-DU-SS | (Vehkamäki, 2002) |
| **GEOS-Chem-APM** | APM | Sectional (1m) | 40 bins for inorganic aerosols & 2 modes for BC and OA | (Yu and Luo, 2009) | SO4, NO3, NH4, SOA, SS, DU, BC, POA | Ternary ion-mediated nucleation (Yu et al., 2018) |
| **GEOS-Chem-TOMAS** | TOMAS | Sectional (2m) | 15 | (Trivitayanurak et al., 2008), | SO4, NH4, BC, DU, SS, POA, SOA | Ternary (+ammonia) (Napari et al., 2002) scaled by 1E-5 |

| | | | | | | |
|---|---|---|---|---|---|---|
| | | | | (Kodros et al., 2016) | | If no ammonia (Vehkamäki, 2002) |
| **GISS-E2.1-MATRIX** | MATRIX | Modal (2m) | 16 mixing states | (Bauer et al., 2008) | SO4, NO3, NH4, H2O, OA, BC, DU, SS | NAPARI ternary nucleation scheme (Napari et al., 2002) |
| **GISS-E2-Tomas** | TOMAS | Sectional (2m) | 15 | (Lee et al., 2015) | SO4, BC (hydrophilic), BC (hydrophobic), OC (hydrophilic), OC (hydrophobic), DU, SS, NH4, water | Binary (Vehkamäki, 2002) |
| **TM4-ECPL** | M7 | Modal (2m) | 7 | (Vignati et al., 2004) | SO4. BC, DU, SS, OA (POA+SOA) SOA: Produced from oxidation of pinene, isoprene and aromatics (xylene, benzene and toluene) with $O_3$, OH, $NO_3$. | Binary (Vehkamäki, 2002) with (Kokkola et al., 2009) scheme for the treatment of the sulfuric acid gas |
| **TM5** | M7 | Modal (2m) | 7 | (Vignati et al., 2004) | SO4, BC, DU, SS, POA, SOA, NO3, NH4, MSA | Organic+ sulfuric acid nucleation (Riccobono et al., 2014); binary homogeneous nucleation (Vehkamäki, 2002) |

## Table S3. Emission inventories and schemes used in the models.

Anthropogenic emissions are given for the year 2011. For interactive emissions, the references are for the model used to calculate the emissions.

| **Model** | **SOx ($SO_2$+SO4) SOx (total)** Tg $a^{-1}$ | | **SO4 (emitted)** Tg $a^{-1}$ | **BC** (Tg $a^{-1}$) | | **POA** (Tg $a^{-1}$) | | **VOC** (Tg $a^{-1}$) | | **SS** (Tg $a^{-1}$) | | **DUST** (Tg $a^{-1}$) | |
|---|---|---|---|---|---|---|---|---|---|---|---|---|---|
| **CAM5-chem-APM** | (Keller et al., 2014) | 55 Tg S $a^{-1}$ | 0 | (Keller et al., 2014) | 7 | (Keller et al., 2014) | 41 TgC $a^{-1}$ | (Lamarque et al., 2012) | Isoprene & monoterpenes 500 TgC $a^{-1}$ | (Gong, 2003) | 11100 | (Mahowald et al., 2006) | 3620 |
| **CAM5-chem-ATRAS2** | (Lamarque et al., 2010) | 64.8 | 1.66 | (Lamarque et al., 2010) | 7.8 | (Lamarque et al., 2010) | 50.3 | NMVOC derived from MOZART emissions for year 2000. | 115 (SOA) | Calculated on line (Mårtensson et al., 2003) (Monahan et al., 1986) | 5039 (wind dependent flux) | Calculated online (Zender et al., 2003) (Albani et al., 2014) | 2677 (wind dependent flux) |
| **CAM5_MAM3** | CMIP6 (Hoesly et al., 2017), (van Marle et al., 2017) | 70.17 | 1.75 | CMIP6 (Hoesly et al., 2017), (van Marle et al., 2017) | 9.32 | CMIP6 (Hoesly et al., 2017), (van Marle et al., 2017) | 44.66 | CMIP6 (Hoesly et al., 2017), (van Marle et al., 2017) MOZART-2 (Horowitz et al., 2003) | 75.36 (SOAg) | Calculated on line (Mårtensson et al., 2003) (Monahan et al., 1986) | 2581.4 | Calculated online (Zender et al., 2003) | 3117.7 |
| **CAM5_MAM4** | $SO_2$: ACCMIP (Lamarque et al., 2013) SO4: 2.5% of $SO_2$ | 64.8 | 1.62 | ACCMIP (Lamarque et al., 2013) | 7.76 | ACCMIP (Lamarque et al., 2013) | 50.2 | NMVOC derived from MOZART emissions for year 2000. | SOA created=103.3 | Calculated on line (Mårtensson et al., 2003) for aerosols with geometric diameter < 2.8 µm (Monahan et al., 1986) for aerosols with geometric diameter > 2.8 µm | Wind dependent flux | Online (Scanza et al., 2015), (Albani et al., 2014) | Wind dependent flux |
| **CAM5.3-Oslo** | (Lamarque et al., 2010) | 66.70 | 1.67 | (Lamarque et al., 2010) | 7.93 | Kirkevåg et al.. (2018) | 87.03 | (Guenther et al., 2006) | 499.5 (isoprene and monoterpene only, i.e. not including MSA contribution) | Calculated online (Salter et al., 2015; Kirkevåg et al., 2018)) | 1956 | Calculated online (Zender et al., 2003) | 3117 |
| **ECHAM6-HAM2** | (Lamarque et al., 2010) | 69.7 Tg-S $a^{-1}$ | 1.7 Tg S a-1 (only direct emitted SO4; SO4 | (Lamarque et al., 2010) | 8.0 | (Lamarque et al., 2010) | 66.7 Tg $a^{-1}$ | (Dentener et al., 2006) | Included in POA | (Long et al., 2011); (Sofiev et al., 2011) | Wind dependent flux | (Tegen et al., 2002); (Cheng et al., 2008); (Heinold et al., 2016) | Wind dependent flux |

| | | | | | | | | | | | | | |
|---|---|---|---|---|---|---|---|---|---|---|---|---|---|
| | | | pro-duced in clouds by wet chemis-try: 51.9 Tg S a-1 is not includ-ed) | | | | | | | | | | |
| **ECHAM5.5-HAM2-ELVOC_UH** | (Lamarque et al., 2010) | 53.9 Tg S $a^{-1}$ | 1.3 Tg S $a^{-1}$ | (Lamarque et al., 2010) | 7.24 | (Lamarque et al., 2010) | 49.3 Tg C $a^{-1}$ | (Guenther et al., 2006) | 27 | (Schultz et al., 2002) | 5032 | (Tegen et al., 2002), (Cheng et al., 2008) | 931 |
| **ECHAM6-HAM2-AP** | (Lamarque et al., 2010) | 70.1 Tg S $a^{-1}$ | 1.7 Tg S a-1 (only direct emitted SO4; SO4 pro-duced in clouds by wet chemis-try: 51.9 Tg S a-1 is not includ-ed) | (Lamarque et al., 2010) | 8.1 | (Lamarque et al., 2010) | 47.9 Tg C $a^{-1}$= 67.0 Tg OA $a^{-1}$ | (Dentener et al., 2006) | Included in POA | Calculated online (Long et al., 2011); (Sofiev et al., 2011) | 1161 | Calculated online (Cheng et al., 2008); (Heinold et al., 2016) | 926 |
| **EMAC** | RCP 8.5 (Riahi et al., 2007) | 63.6 Tg S $a^{-1}$ | 1.6 Tg S $a^{-1}$ | RCP 8.5 (Riahi et al., 2007) | 6.7 | RCP 8.5 (Riahi et al., 2007) | 41.1 Tg C $a^{-1}$ | RCP 8.5 (Riahi et al., 2007) | Included in POA | Total Sea salt: (Dentener et al., 2006) chemical Composition of sea salt: (Seinfeld and Pandis, 2006) | 7889 | Total dust emissions: (Astitha et al., 2012) Chemical composi-tion of dust: (Karydis et al., 2016); (Klingmüller et al., 2018) | 4760 |
| **GEOS-Chem-APM** | (Keller et al., 2014) | 55 Tg S $a^{-1}$ | 0 | (Keller et al., 2014) | 7 | (Keller et al., 2014) | 41 Tg C $a^{-1}$ | (Keller et al., 2014) | Isoprene & monoter-penes 760 TgC $a^{-1}$ | (Gong, 2003) | 10800 | Calculated online (Zender et al., 2003) (Mahowald et al., 2006) | 1180 |
| **GEOS-Chem-TOMAS** | Mixture of global and regional inventories (described in Kodros et al., | 395.36 | 0.27 Tg S a-1 | Anthropogen-ic: Bond et al. (2007) Bio-mass burning: (Wiedinmyer et al., 2011) | 6.97 | Anthropo-genic: (Bond et al. 2007) Biomass burning: | 44.72 | Biogenic VOC emissions from (Guenther et al., 2006), Anthro-pogenically-influenced VOCs | Biogenic SOA creat-ed=19 Tg C a-1 Anthropo-genically- | Calculated online (Jaeglé et al., 2011) | Wind depend-ent flux | Calculated online (Zender et al., 2003) | Wind depend-ent flux |

| | | | | | | | | | | | | | |
|---|---|---|---|---|---|---|---|---|---|---|---|---|---|
| | 2016; Keller et al., 2014) | | | | | (Wiedinmyer et al. 2011) | | from (D'Andrea et al., 2013) | enhanced SOA created=100 Tg $a^{-1}$ | | | | |
| **GISS-E2.1-MATRIX** | (Lamarque et al., 2010) | 191.82(SO2) | 5.27 | (Lamarque et al., 2010) | 9.35 | (Lamarque et al., 2010) | 61.73 | Isoprene: (Guenther et al., 1995). Monoterpenes and ORVOC: (Lathiere et al., 2005) | Isoprene: 524 Terpenes + ORVOC: 193 SOA production 17.1 | (Schmidt et al., 2014) | 2662.69 | (Schmidt et al., 2014) | 1275.60 |
| **GISS-E2-Tomas** | 1 % of $SO_2$ ACCMIP (Lamarque et al., 2013) | 65.6 | 0.66 | ACCMIP and GFEDv3 for biomass burning | 7.4 | ACCMIP and GFEDv3 for biomass burning | 43.7 | ACCMIP (Lamarque et al., 2013) | SOA production rate of 17 | (Gong, 2003) | 3231.9 | (Ginoux et al., 2001) | 705.8 |
| **TM4-ECPL and TM4-ECPL/v** | 2.5% of SO2 ACCMIP (Lamarque et al., 2013) | 121.25($SO_2$) | 4.66 (SO4) | ACCMIP (Lamarque et al., 2013) | 8.02 | ACCMIP (Lamarque et al., 2013) | 35.12 Tg C $a^{-1}$ | Emissions of Biogenic VOCs are taken from (Sindelarova et al., 2014) Anthropogenic VOC ACCMIP, Ocean emissions POET | Isoprene: 525 monoterpenes: 104.3 other VOC: 572.3 SOA production: 32.6 | (Vignati et al., 2010) | 8521 | (Dentener et al., 2006) | 1169.5 |
| **TM5** | CMIP6 (Hoesly et al., 2018); (van Marle et al., 2017); GEIA (Andres and Kasgnoc, 1998) | 62.04 | 1.59 | CMIP6 (Hoesly et al., 2018); (van Marle et al., 2017) | 9.49 | CMIP6 (Hoesly et al., 2018); (van Marle et al., 2017) | 52.02 | CMIP6 (Hoesly et al., 2018); (van Marle et al., 2017); MEGAN-MACC (Sinderalova et al., 2014) | 109.32 | Calculated online (Gong et al., 2000); (Salisbury et al., 2013) | 5497.08 | Calculated online (Tegen et al., 2002) | 978.88 |

**Table S4. Biomass burning emission's injection height and dry and wet deposition parameterization in the models.**

| Model | Biomass Burning Emissions injection height | Dry and Wet Deposition |
|---|---|---|
| **CAM-chem-APM** | Emission data are produced from OC forest fire and grass fire emissions from the file IPCC_GriddedBiomassBurningEmissions_OC_decadalmonthly mean by NCAR. In January forest fire emissions extent up to 4 km in the tropics and extratropical mid-latitudes of the south hemisphere and in June they extend to 6 km at around 60 N Lamarque et al. (2010) | **Dry deposition**: Gases (Wesely, 1989) "functions of solar radiation and/or time of day", Aerosols (Zhang et al., 2001) "Dry (gravitational and turbulent) deposition velocity"<br>**Wet deposition:** Scheme from Neu and Prather (2012) for gases "Washout of highly soluble gases by rain in ambient air is modeled as an impact scavenging process, while scavenging of moderately soluble gases from the ambient air is limited by Henry's Law equilibrium with the falling precipitation. Washout of gases from interstitial and ambient air takes place in the Mixed Cloud (MC) and Ambient (AM) fractions. We assume a constant rate of evaporation in AM, which releases gases to the environment along with any large-scale evaporation" and the scheme from Rasch et al. (2000) for aerosols "Many aerosols act as cloud condensation nuclei. That is, water vapour condenses preferentially on soluble or wettable particles to form cloud drops subsequently removed via in-cloud scavenging. Aerosols can also be taken up directly on falling precipitate through a number of collection mechanisms. Larger aerosols are taken up by collision associated with their inertia. Smaller particles are collected by Brownian motion." Washout of size resolved aerosols (Henzing et al., 2006) "A size dependent parameterization for the removal of aerosol particles by falling rain droplets has been developed. For below-cloud scavenging a source for sea salt aerosol has been adopted. or particles with diameter larger than 1μm, below-cloud scavenging is as important as the removal in convective updrafts and that below-cloud scavenging accounts for 12% of the total yearly average removal. At mid-latitudes of both hemispheres the fractional contribution of below-cloud scavenging to the total removal is about 30% with regional maxima exceeding 50%. The maxima in relative importance of below-cloud scavenging coincide with maxima in emissions. Excluding the below-cloud scavenging process would result in an increase of global average aerosol lifetime from 2.16 days to2.47 days." |
| **CAM5-chem-ATRAS2** | Injection height profiles for forest fire and grass fire emissions are derived from the corresponding AeroCom profiles (Dentener et al., 2006), which give emissions in 6 altitude ranges (0-0.1, 0.1-0.5, 0.5-1, 1-2, 2-3, and 3-6 km). | **Dry deposition** velocity (gravitational and turbulent) (Zhang et al., 2001)<br>**Wet deposition** is both in-cloud scavenging of cloud-borne aerosol and the below cloud scavenging of interstitial aerosol. Reference for deposition processes (Liu et al., 2012)*. The CAM5_MAM3 model here includes additional improved treatments of convective transport and wet removal of aerosols developed by Wang et al. (2013). |
| **CAM5_MAM3** | | |
| **CAM5_MAM4** | | |
| **CAM5.3-Oslo** | Dentener et al. (2006) | **Dry deposition:** Liu et al. (2012)*<br>**Wet deposition:** Below-cloud scavenging, using below-cloud collection efficiencies as in Seland et al. (2008), and in-cloud scavenging (Liu et al., 2012)*. |
| **ECHAM5.5-HAM2-ELVOC_UH** | Dentener et al. (2006) | **Dry deposition:** big leaf approach, a function of aerodynamic resistance, quasi-laminar boundary layer resistance, and surface resistance (Ganzeveld and Lelieveld,1995; Ganzeveld et al.,1998). Turbulent dry deposition of aerosols (Ganzeveld et al., 1998).<br>**Wet deposition:** Below-cloud scavenging (Seinfeld and Pandis, 1998; Stier et al., 2005). In-cloud and below-cloud scavenging of precursor gases: Henry's law (Seinfeld and Pandis, 1998) |

| | | |
|---|---|---|
| | | Reference for deposition processes Zhang et al. (2012) |
| **ECHAM6-HAM2** | Injection heights of biomass burning emissions follow the recommendations of Val Martin et al. (2010). 75% of the emissions are evenly distributed within the planetary boundary layer (PBL), 17% in the first level and 8% in the second level above the PBL (Tegen et al., 2019) | Tegen et al. (2018)<br>The aerosol **dry deposition** flux is computed as the product of tracer concentration, air density and deposition velocity, depending on the aerodynamic and surface resistances for each surface type considered by ECHAM6.3, and subsequently added up for the fractional surface areas.<br>Sedimentation of aerosol particles is computed for accumulation and coarse modes (i.e. large particles) using Stokes velocity and the Cunningham slip correction factor. To ensure numerical stability the sedimentation velocity is limited by the ratio of layer thickness to model timestep.<br>Dry deposition is computed for all modes except the nucleation mode<br>For **wet deposition** the in-cloud scavenging scheme from Croft et al. (2010) dependent on the wet particle size is used. The in-cloud scavenging scheme takes into account scavenging by droplet activation and impaction scavenging in different cloud types, distinguishing between stratiform and convective clouds and warm, cold, and mixed-phase clouds. Below clouds particles are scavenged by rain and snow using a size-dependent below-cloud scavenging scheme (Croft et al., 2009).<br>In-cloud (Croft et al., 2010) and below-cloud (Croft et al., 2009) wet scavenging depends on the size of the aerosol particles. |
| **ECHAM6-HAM2-AP** | Injection heights of biomass burning emissions follow the recommendations of Val Martin et al. (2010). 75% of the emissions are evenly distributed within the planetary boundary layer (PBL), 17% in the first level and 8% in the second level above the PBL (Tegen et al., 2019) | Tegen et al. (2018)<br>The aerosol **dry deposition** flux is computed as the product of tracer concentration, air density and deposition velocity, depending on the aerodynamic and surface resistances for each surface type considered by ECHAM6.3, and subsequently added up for the fractional surface areas.<br>Sedimentation of aerosol particles is computed for accumulation and coarse modes (i.e. large particles) using Stokes velocity and the Cunningham slip correction factor. To ensure numerical stability the sedimentation velocity is limited by the ratio of layer thickness to model timestep.<br>Dry deposition is computed for all modes except the nucleation mode<br>For **wet deposition** the aerosol processing scheme by Hoose et al. (2008a, 2008b) is used for in-cloud wet scavenging. The aerosol processing scheme explicitly tracks the aerosol mass within cloud droplets and ice crystals and computes online the processes which add (nucleation, impaction) and remove (evaporation, rain formation) aerosol mass inside cloud droplets and ice crystals. Below clouds particles are scavenged by rain and snow using a size-dependent below-cloud scavenging scheme (Croft et al., 2009). |
| **EMAC** | Injection height is 140 m | **Dry deposition:** DRYDEP submodel (Kerkweg et al., 2006) based on the big leaf approach (only one receptor surface is present in the model and that turbulent exchange within the forest canopy is neglected).<br>**Wet deposition:** SCAV submodel (Tost et al., 2006); The SCAV submodel is highly structured, and all calculations are performed in the smallest meaningful entity. For the physico-chemical process 'scavenging' this is a vertical column since the chemical composition of the rainwater that enters a grid box from above affects the scavenging in that particular layer as well as the layers below. Within the column, the scavenging process starts in the uppermost layer where a cloud occurs (Nucleation Scavenging - NS). In the |

| | | |
|---|---|---|
| | | layer below, the Impaction Scavenging (IS) by the incoming precipitation flux is calculated first, followed by NS in that particular layer. If there are no clouds in this layer, the NS is neglected and only IS is calculated. |
| **GEOS-Chem-APM** | Well mixed within the planetary boundary layer | **Dry deposition**: Gases (Wesely, 1989) "functions of solar radiation and/or time of day", Aerosols (Zhang et al., 2001) "Dry (gravitational and turbulent) deposition velocity"<br>**Wet deposition** (Jacob at al., 2000) "wet convective mass fluxes and precipitation fluxes. We use this information to implement two types of scavenging: (1) scavenging in subgrid wet convective updrafts, and (2) first-order rainout and washout in precipitating columns. The scavenging is applied to aerosols and to soluble gases of interest to tropospheric O3chemistry including HNO3,H2O2,CH3OOH, and CH2O.The methodology is readily extendable to other soluble gases" and (Wang et al., 2011) "Liu et al. (2001) includes scavenging in convective updrafts, as well as in-cloud and below-cloud scavenging from convective and large-scale precipitation. However, it does not distinguish between rain and snow. Wang et al. introduce such a distinction as well as other improvements to the scavenging scheme." Washout of size resolved aerosols (Henzing et al., 2006) |
| **GEOS-Chem-TOMAS** | Evenly distributed throughout the boundary layer | Size-resolved dry and wet deposition (Trivitayanurak et al., 2008). Dry deposition follows a resistance in series scheme. Wet deposition considers in cloud and below cloud scavenging separately for stratiform and convective anvils. |
| **GISS-E2.1-MATRIX** | Evenly distributed throughout the boundary layer | **Dry deposition**: Turbulent dry deposition is based on the resistence-in- series scheme described in Koch et al. (1999) and Chin et al. (1996). The scheme is coupled to the model boundary layer scheme of the GCM and depends on the mean diameter of the aerosol population. Gravitational settling depends on the aerosol population mean diameter and density and accounts for the effects of RH on density and size.<br>**Wet deposition**: The wet deposition schemes of the GISS modelE are described in Koch et al. (1999, 2006) and Bauer et al (2008). The model treats two types of clouds, convective and stratiform clouds. Tracer treatment in clouds follows the cloud processes, so that tracers are transported, dissolved, evaporated, and scavenged (with cloud-water autoconversion and by raindrop impaction beneath clouds). This parameterization requires information about aerosol size and solubility, which are calculated for each aerosol population by MATRIX. The averaged solubility per aerosol population is calculated by using a volume weighted approach, depending on the chemical composition of the aerosol particles. Number and mass concentrations are both treated in the model's advection and deposition schemes. |
| **GISS-E2-Tomas** | Evenly distributed throughout the boundary layer | The dry deposition scheme is based on a resistance-in-series method derived from the Harvard GISSCTM, which is applied between the surface layer (10 m) and the ground (Koch et al., 2006). Wet deposition is determined by several processes including rainout within clouds, washout below precipitating regions, scavenging within and below cloud updrafts, evaporation of falling precipitation, transport along with convective plumes, and detrainment and evaporation from convective plumes (Koch et al., 2006; Shindell et al., 2006). Both wet and dry deposition are fully size-resolved. For in-cloud scavenging, modified Kohler theory is used to calculate the critical supersaturation for activation of aerosols. |
| **TM4-ECPL & TM4-ECPL/v** | Dentener et al. (2006) | **Dry deposition** for all fine aerosol components is parameterized similarly to that of nss-$SO4^{-2}$, which follows Tsigaridis et al. (2006) and the resistance model by Gazenveld et al |

| | | |
|---|---|---|
| | | (1998). Gravitational settling (Seinfeld and Pandis, 1998) is applied to all aerosol components and is an important dry deposition process for coarse particles like dust and sea salt (Myriokefalitakis et al., 2015).<br>For **wet deposition**, both largescale and convective precipitation are considered. In-cloud and below-cloud scavenging is parameterized in TM4-ECPL as described in detail by Jeuken et al. (2001). In-cloud scavenging of water-soluble gases is calculated, accounting for the solubility of the gases (effective Henry law coefficients; Tsigaridis et al., 2006; Myriokefalitakis et al., 2011 and references there in) |
| **TM5** | Injection heights of biomass burning follow the recommendations of Dentener et al. (2006), as described in van Noije et al. (2014). In the current study, biomass burning emissions from the CMIP6 data set are applied, and no distinction is made between forest fires and grassland fires; all biomass burning emissions are distributed as forest fires. | Dry and wet depositions follow the description given in van Noije et al. (2014) and de Bruine et al. (2018). **Dry deposition** of gases and aerosols uses a standard resistance approach (e.g. Seinfeld and Pandis, 2006). For gases the deposition velocities are calculated as the inverse of the sum of an aerodynamic resistance, a quasi-laminar sub-layer resistance and a surface resistance, while for aerosols the velocities are determined by the aerodynamic resistance and quasi-laminar sublayer resistance, enhanced by gravitational settling.<br>The **wet deposition** of gases and aerosols by rain is calculated separately for convective and large-scale stratiform precipitation. Scavenging in convective clouds is part of the convective mass transport operator (Balkanski et al., 1993; Guelle et al. 1998). Scavenging in and below stratiform clouds is calculated following Roelofs and Lelieveld (1995) and Jeuken et al. (2001), with updated removal efficiencies for aerosols as given in de Bruine et al. (2018). |

*** Liu et al., 2012**

**Wet Removal**

Aerosol wet removal is calculated using the CAM3.5 wet removal routine (Barth et al., 2000; Rasch et al., 2000) with modifications noted below. The routine treats in-cloud scavenging (the removal of cloud-borne AP) and below-cloud scavenging (the removal of interstitial AP by precipitation particles through impaction and Brownian diffusion). For in-cloud scavenging, the precipitation production rates (kg $kg^{-1}$ $s^{-1}$) and cloud water mixing ratios (kg $kg^{-1}$ ) for the stratiform and convective clouds are used to calculate first-order loss rates ($s^{-1}$ ) for cloud water. These cloud-water first-order loss rates are multiplied by "wet removal adjustment factors" (or tuning factors) to obtain aerosol first-order loss rates, which are applied to activated aerosols within the non-ice cloudy fractions of a grid cell (i.e., cloudy fractions that contain some cloud water). The stratiform in-cloud scavenging only affects the explicitly treated stratiform-cloud-borne 12 AP, and the adjustment factor of 1.0 is currently used. It does not affect the interstitial AP. In-cloud scavenging in ice clouds (i.e., clouds with no liquid water) is not treated. For convective in-cloud scavenging of MAM aerosols, the cloud-borne aerosol mixing ratios within the convective clouds are needed. These are set to the product (lumped interstitial aerosol mixing ratio) × (convective-cloud activation fraction), and we again note that the model's lumped interstitial aerosol mixing ratios include the truly interstitial AP and the convective cloud-borne AP. The convective-cloud activation fractions are currently set to 0.0 for the primary carbon mode, 0.4 for the fine and coarse dust modes, and 0.8 for other modes. The lower values reflect lower hygroscopicity. These factors are applied to both number and mass species within each mode, with one exception. In MAM3, different activation fractions are applied to the dust and sea salt of the coarse mode (0.4 and 0.8 respectively), and a weighted average is applied to the coarse mode sulfate and number. A wet-removal adjustment factor of 0.5 is used for the convective in-cloud scavenging. The stratiform-cloud-borne AP reside in the stratiform clouds and are assumed to not interact with convective clouds. For below-cloud scavenging of the interstitial aerosol, the first-order

removal rate is equal to the product (scavenging coefficient) × (precipitation rate). The scavenging coefficient is calculated using the continuous collection equation (e.g., Equation 2 of Wang et al., 2011), in which the rate of collection of a single aerosol particle by a single precipitation particle is integrated over the aerosol and precipitation particle size distributions, at a precipitation rate of 1 mm $h^{-1}$. Collection efficiencies from Slinn (1984) and a Marshall-Palmer precipitation size distribution are assumed. The scavenging coefficient varies strongly with particle size, with lowest values for the accumulation 13 mode. The wet removal adjustment factor is currently 0.1. There is no below-cloud scavenging of stratiform-cloud-borne aerosol. Aerosol that is scavenged at one altitude can be re-suspended at a lower altitude if precipitation evaporates. A fraction of the in-cloud scavenged aerosol is re-suspended, and the re-suspended fraction is equal to the fraction of precipitation that evaporates below cloud.

**Dry Deposition**

Aerosol dry deposition velocities are calculated using the Zhang et al. (2001) parameterization with the CAM5 land-use and surface layer information. Gravitational settling velocities are calculated at all vertical layers above the surface following Seinfeld and Pandis (1998). Both velocities depend on particle wet size, so average values for aerosol mass and number are calculated for each mode. The velocities for cloud-borne aerosols are calculated based on droplet sizes. Aerosol mixing ratio changes and fluxes from dry deposition and sedimentation throughout a vertical column are then calculated using the CAM3 dust deposition/sedimentation routine (Zender et al., 2003).

**Table S5. Measurement sites included in this study.**

The classification and location of the stations are denoted, the supersaturation values at which CCN concentrations are measured at each site and the aerosol components for which mass is measured in the $PM_1$. The followed notation is: $CCN_x$: CCN at *x* % supersaturation, SO4: sulphate, OA: organic aerosols, SS: sea salt, NO3: Nitrates, NH4: ammonium. Details on observations, methods and data coverage can be found in Schmale et al. (2017).

| Station name | Location/type | Geoposition | Observations |
|---|---|---|---|
| **Cabauw** | Cabauw, The Netherlands near coast, rural-background | 51°58'N, 04°56'E, -1 m | $CCN_{0.1}$, $CCN_{0.2}$, $CCN_{0.3}$, $CCN_{0.5}$, $CCN_{1.0}$, SO4, OA, SS, NH4, NO3 |
| **Finokalia** | Finokalia, Crete, Greece, coastal background, Mediterranean | 35°20'N, 25°40'E, 260 m | $CCN_{0.2}$, $CCN_{0.4}$, $CCN_{0.6}$, $CCN_{0.8}$, $CCN_{1.0}$, SO4, OA, SS, NH4, NO3 |
| **Jungfraujoch** | Jungfraujoch, high alpine, background Switzerland | 46°33'N, 07°59'E, 3580 m | $CCN_{0.1}$, $CCN_{0.15}$, $CCN_{0.2}$, $CCN_{0.25}$, $CCN_{0.3}$, $CCN_{0.35}$, $CCN_{0.4}$, $CCN_{0.5}$, $CCN_{0.7}$, $CCN_{1.0}$, SO4, OA, NH4, NO3 |
| **Mace Head** | Mace Head, Ireland, coastal background | 53°19'N, -9°54'E, 5 m | $CCN_{0.1}$, $CCN_{0.25}$, $CCN_{0.35}$, $CCN_{0.5}$, $CCN_{0.75}$, $CCN_{1.0}$, SO4, OA, SS, NH4, NO3 |
| **Melpitz** | Melpitz, Germany, continental, background | 51°32'N, 12°56'E, 89 m | $CCN_{0.1}$, $CCN_{0.2}$, $CCN_{0.3}$, $CCN_{0.5}$, $CCN_{0.7}$, SO4, OA, SS, NH4, NO3 |
| **Noto Peninsula** | Noto Peninsula, Japan, coastal background | 37°45'N, 137°36'E, 0 m | $CCN_{0.1}$, $CCN_{0.2}$, $CCN_{0.5}$, $CCN_{0.8}$ |
| **Puy de Dôme** | Puy de Dôme, France, mountain continental background | 45°46'N, 2°57'E, 1465 m | $CCN_{0.2}$ |
| **Hyytiälä** | Hyytiälä, Finland, background boreal forest rural | 61°51'N, 24°17'E, 181 m | $CCN_{0.1}$, $CCN_{0.2}$, $CCN_{0.3}$, $CCN_{0.5}$, $CCN_{1.0}$, SO4, OA, SS, NH4, NO3 |
| **Vavihill** | Vavihill, Sweden, background rural | 56°01'N, 13°09'E, 172 m | $CCN_{0.1}$, $CCN_{0.15}$, $CCN_{0.2}$, $CCN_{0.25}$, $CCN_{0.3}$, $CCN_{0.35}$, $CCN_{0.4}$, $CCN_{0.5}$, $CCN_{0.7}$, $CCN_{1.0}$, $CCN_{1.4}$ |

## Appendix S2

### S2.1.Particle numbers, CCN calculations

Number concentrations of particles of various sizes ($N_{50}$, $N_{80}$ and $N_{120}$) are computed by 14 models for all observational sites. For the modal models, where lognormal distributions are used to describe internally or externally mixed particle populations, the total number of particles with dry diameters larger than a threshold diameter $D_0$ is given by

$$N(D > D_0) = \sum_{i=1}^{k} \frac{N_0^i}{2}\left(1 - \mathrm{erf}\left(\frac{\ln\left(D_0/\widetilde{D_n^i}\right)}{\sqrt{2}}\right)\right) \quad (1)$$

where $k$ is the number of modes, $N_0^i$ and $\widetilde{D}_n^i$ are the number of particles and the particle number median diameter of mode $i$, respectively, while $erf$ is the error function. In several models calculation of the CCN number concentration is based on the $\kappa$-Köhler theory as developed by (Petters et al, 2007), according to which, for a given supersaturation $s$, the critical dry diameter $D_d$ of activated particles is given by

$$s(D) = \frac{D^3 - D_d^3}{D^3 - D_d^3(1-\kappa)} \exp\left(\frac{4\sigma_{s/a} M_w}{RT\rho_w}\right) \quad (2)$$

Here $D$ and $D_d$ are the wet and dry diameters of particles, respectively, $\sigma_{s/a}$ is the surface tension of the solution/air interface, which is taken equal to 0.072 J $m^{-2}$, $\rho_w$ is the density of water, $M_w$ is the molecular weight of water, $R$ is the ideal gas constant and $T$ is the temperature. After having determined the critical dry diameter from Eq. (2), the number of CCN is calculated from Eq. (1) as the number of particles with dry diameters larger than this critical value.

The hygroscopicity, $\kappa$, for the particle as a whole, or just for the coating layer if it is sufficiently thick for models that take into account coated particles, is determined based on the volume weighted hygroscopicities of the individual components, $\kappa_j$, where $\varepsilon_i$ is the fraction of the dry aerosol volume occupied by the individual components, $j$.

$$\kappa = \sum_j \varepsilon_j \kappa_j \quad (3)$$

In the present study, different hygroscopicity parameters are used in each model as summarized in Table 1

### S2.2. Persistence – autocorrelation function

According to the mathematical definition for a stationary time series of values $Y_1$, $Y_2$, ..., $Y_N$ at the time instances $t_1$, $t_2$, ..., $t_N$, the autocorrelation function (ACF) at time lag $k$ is given by

$$r_k = \frac{\sum_{i=1}^{N-k+1}(Y_i - \bar{Y})(Y_{i+k} - \bar{Y})}{\sum_{i=1}^{N+1}(Y_i - \bar{Y})^2} \quad (4)$$

where $\bar{Y}$ is the average value of $Y_i$. The large-lag standard error is computed as the square root of the variance given by:

$$Var(r_k) = \frac{1}{N}\left(1 + 2\sum_{i \simeq 1}^{k} r_i^2\right) \quad (5)$$

where $r_i$ is the ACF at time $i$. The persistence time can then be defined as the time lag at which the ACF crosses the curve of the large-lag standard error, i.e. when the ACF is significant compared to the standard error (Schmale et al., 2018).

# Appendix S3. Results

## S3.1 CCN persistence- Individual model's behavior and sensitivity to size of the emitted particles

It is worth noting here that the number concentration of CCN is not directly related to the persistence time. For example, based on the observational data at the Melpitz station, the persistence time of $CCN_{0.2}$ during winter is 3.5 times longer than during summer (7 days and 2 days respectively; Fig. 7), although the $CCN_{0.2}$ number concentration during winter (~1500 $cm^{-3}$) is only 25% higher than during summer (1200 $cm^{-3}$) (Fig. 3). This is because the ACF and the subsequently computed persistence are related to the rate of change of the CCN number concentration due to the various formation, transport and removal processes, and not to the absolute level of CCN. As such, when the CCN population remains almost unchanged for a long time period, the persistence is high, independent of the CCN concentrations.

For the Vavihill station, in contrast to the observations, all models (except EMAC) calculate somewhat longer persistence during winter. However, the observed ratio at this station has been assumed to reflect a peculiarity of the observation period during 2013 and 2014 (Schmale et al., 2018). The same behavior is also observed at the Noto Peninsula station. Most of the models, in agreement with observations, simulate persistence of ~ 2 days during summer, but none of them is able to simulate the longer persistence observed during winter.

For the remaining stations, the comparisons show similar performances for all models in terms of the winter/summer persistence. For Melpitz, Cabauw and Hyytiälä, longer persistence is observed during winter and can be ascribed to the more stable weather conditions during this season. For these stations, it appears that only four out of the 14 models (GEOS-Chem-APM, CAM5-MAM3, CAM5-MAM4, and CAM5-chem-ATRAS2) correctly simulate the winter/summer relative order of persistence, although the model persistence is smaller than the observationally derived values. These models also all use MERRA, rather than ERA which is used in the other models. At Finokalia, the longer persistence observed during summer is attributed to the more stable weather conditions during summer. This behavior is reproduced by all models but five (CAM5-Chem-APM, CAM5.3-Oslo, EMAC, GISSE2.1-MATRIX, TM4-ECPL).

Analyzing the reasons that affect the persistence and then attributing the differences between the observed and the model-derived values to the underlying physical and/or chemical process parameterizations in each model is a demanding

task which most probably is model dependent. Here a first attempt is made by examining the sensitivity of the persistence to the size of the emitted OA and BC particles. For that, we first focus on the Finokalia station and we examine the results obtained from two different simulations using the TM4-ECPL model. The setups of the two simulations are almost identical differing only in the size of the emitted OA and BC particles (details in the caption of Figure S5). Since the total OA and BC emitted masses are kept constant, changing the emitted particle sizes affects the number of emitted particles. Overall, in the new sensitivity simulation larger but fewer particles are emitted compared to the base simulation. The $CCN_{0.2}$ persistences computed from the results of the two simulations are compared with the observations in Figure S5a. In the sensitivity simulation (green bars, larger particles) an increase of the persistence during summer by a factor > 2 is seen compared to the base simulation (red bars). This increase leads to an inversion of the winter/summer ratio of persistence since during winter the persistence time remained almost unchanged. The results of the sensitivity simulation are in better agreement with observations and demonstrate the importance of the size distribution of the emitted particles for the CCN simulations and also suggest that the size is probably underestimated in the base case simulation of TM4-ECPL.

In order to identify the factors that caused this change in the relative order of the persistence at Finokalia, we have calculated the ACF of the $CCN_{0.2}$ number concentrations (Figures S5b, S5c). The black lines show the observational data during summer (solid line) and winter (dashed line) and the red lines show the results of the base simulation with TM4-ECPL, obtained for the same time-periods with the observations (Fig. S5b), while the green lines show the results of the sensitivity simulation (Fig. S5c). It is seen that for short time-periods (<15 h) both the observational and model derived ACF (denoted as $ACF^{obs}$ and $ACF^{model}$, respectively) smoothly decrease. Since the $ACF^{model} > ACF^{obs}$ during that time ($t < 15$ h) the simulated CCN population varies less than the observed one. The fact that both $ACF^{model}$ in the base simulation and $ACF^{obs}$ vary less during winter than during summer, suggests that both model- and observationally-computed persistence are higher in winter. However, during summer, after the first ~24 hours a local maximum is present in both $ACF^{model}$ and $ACF^{obs}$ that shows a periodicity of 24 hours. This peak indicates a daily periodic phenomenon and can be attributed to the almost constant weather conditions during summer that drive a diurnal cycle in the photochemical formation of $H_2SO_4$ in the gas phase in the Finokalia region (Mihalopoulos et al., 2007). During summer a significant difference between the $ACF^{model}$ from the base simulations and $ACF^{obs}$ is found at longer correlation times ($t > 15$ h), when the $ACF^{obs}$ decays much slower than the $ACF^{model}$ leading to larger observed than modeled persistence. This can be attributed to the different production/loss rates ratio of the $CCN_{0.2}$ particles. Possible explanations are related to the aerosol aging, wet deposition and sedimentation removal, long-range transport, or model resolution that affect the lifetime of aerosols in the atmosphere.

Figure S5c depicts the ACFs of the sensitivity simulation (green lines) and the observations. Comparing the results of the two simulations (panels b and c), it is seen that during winter the two $ACF^{model}$ are similar, while large differences are found between the two $ACF^{model}$ during summer. This is due to the slower decay of $ACF^{model}$ in the sensitivity simulation leading to a higher persistence time, similar to the observed one. For Cabauw station (Fig. S5d) that is affected by fresh primary emissions, the sensitivity simulation shows better agreement in persistence time with the observationally derived values; while for Mace Head station (Fig. S5f) that is received air masses transported over the ocean the two simulations

provide similar results. For Hyytiälä (Fig. S5e), the adopted change in the size of emitted particles is not sufficient to reconcile model-derived and observationally-derived persistence times, indicating that other factors might be also important for this discrepancy.

## S3.2. Statistics for the comparisons between model results and observations

The following statistical variables have been computed here to quantify the agreement of model results with the observations.

Mean Error (ME)

$$\mathrm{ME} = \frac{1}{N}\sum_{i=1}^{N}(P_i - O_i)$$

Normalized Mean Bias (NMB)

$$\mathrm{NMB} = \frac{\sum_{i=1}^{N}(P_i - O_i)}{\sum_{i=1}^{N} O_i} \times 100\%$$

Normalized Mean Error (NME)

$$\mathrm{NME} = \frac{\sum_{i=1}^{N}|P_i - O_i|}{\sum_{i=1}^{N} O_i} \times 100\%$$

Root Mean Square Error (RMSE)

$$\mathrm{RMSE} = \sqrt{\frac{1}{N}\sum_{i=1}^{N}(P_i - O_i)^2}$$

Index of agreement

$$\mathrm{IOA} = 1 - \frac{\sum_{i=1}^{N}(P_i - O_i)^2}{\sum_{i=1}^{N}(|O_i - \bar{O}| + |P_i - \bar{O}|)^2}$$

Mean absolute Error (MAE)

$$\mathrm{MAE} = \frac{1}{N}\sum_{i=1}^{N}|P_i - O_i|$$

The results are shown in Table S6 (separate file).

## S3.3. Surface PM1 composition - Global distributions

The global surface distributions of the multi-model mean of the various chemical compounds (SO4, BC, OA, SS and DU) concentrations that contribute to $PM_1$ as the median of the 15 models are shown in supplementary Figure S15 (left columns)

together with the corresponding model diversities (right column); while Figures S6-S14 show the results of individual models. Note that all simulated $PM_1$ component diversities maximize south of 60°S and north of 60°N, which reflects the challenges of the models in simulating atmospheric circulation and chemistry close to the poles. Since sulphate is formed by oxidation of sulfur dioxide ($SO_2$), which is mainly produced from anthropogenic activities, high concentrations of sulphate are observed in industrialized regions. In Eastern China, where the highest annual concentration of SO4 is computed, the concentration reaches 12.5 μg $m^{-3}$, in India 7.0 μg $m^{-3}$, around the Mediterranean basin 5.0 μg $m^{-3}$ and in the eastern United States 3.0 μg $m^{-3}$. In marine regions, where $SO_2$ is formed predominantly through oxidation of dimethyl sulfide (DMS), the sulphate concentrations are significantly lower and do not exceed 1.0 μg.$m^{-3}$ in the Northern Hemisphere and 0.6 μg $m^{-3}$ in the Southern Hemisphere. The highest diversities are calculated for the high latitude oceanic regions in both hemispheres. In continental regions the highest diversities of 5 to 10 are found far from the main $SO_2$ production sources, in South America, Central Africa and Indonesia. Mann et al. (2014) pointed out that the model diversities are higher in northern Europe than in southern Europe, while in Figure 12b the opposite is seen for the present study.

BC is entirely produced by combustion of fossil fuel and biomass, including wild-fires, and volcanoes (Bycenkiene et al., 2013). Therefore, BC is observed in high amounts over continents and in significantly lower amounts over the ocean. Mass concentrations reach a maximum in Eastern China (~4.5 μgC $m^{-3}$) and in India (~2.0 μgC $m^{-3}$), while in other continental regions the annual average concentrations do not exceed 1.0 μg $m^{-3}$ and over the ocean 0.1 μg $m^{-3}$. Besides polar and high-latitude regions, high diversities are also observed over the ocean and in continental regions away from the sources. Model differences can be attributed to the emissions used in the models, which differ in strength, spatial distribution, and the assumed size of the emitted particles, as well as to the removal processes, such as wet and dry deposition. Indeed, high diversity is computed over biomass burning regions in tropical South America, Africa and Indonesia but also in Saudi Arabia where oil extraction plants exist. Differences in the assumed organic mass to organic carbon ratio in the models could explain some of this model diversity. High diversities over the tropical oceans in the outflow of biomass burning regions are also associated with very low BC concentrations, differences in the transport and in the deposition patterns. The highest diversities are, however, computed close to the poles where BC levels are very low. These results are in agreement with Mann et al. (2014) who attributed model differences mainly to removal processes.

Modeling OA is more challenging than SO4 and BC, since it involves the treatment of both primary emissions as well as the secondary formation of organics from precursor gases. Model diversities are largest over the tropical oceans as well as the southern oceans suggesting that differences in the marine source of OA (or lack of such source) are the major contributors to this diversity. Similar to BC, smaller diversities are found over and downwind of biomass burning regions and in the Arabian Peninsula where oil combustion emissions prevail. Tsigaridis et al. (2014) also revealed large differences between the models in the organics source strength and formation of SOA, which reached almost an order of magnitude. That study also investigated the models' treatment of the removal of OA and found large inter-model differences especially in the strength of the wet deposition. They also found that the diversity between the models has maxima over oceanic regions south of 30°S; part of this diversity can be attributed to the marine source representation of OA in the models. In the present

study, the model diversity is slightly higher than in the earlier study over these regions, while the global surface distribution of OA shows a similar pattern.

The SS concentration (Fig. S15g), which is driven by wind speed and temperature, has maxima over the Southern Ocean. It also reveals some advection of SS over land. However, due to differences in the source parameterization and strength as well as in the deposition, large diversities (>10) between models (Fig. S15h) are computed for the Southern Ocean as well as at the Polar regions. Similarly high diversity is found over the Caspian Sea, which most probably is not properly resolved by many models, as well as over the northern part of South America where sea salt concentrations are low resulting from little inland transport of SS.

In line with these remarks, submicron dust aerosol (Fig. 15i), which is a minor contributor to the total dust emissions, has maxima over source regions with the highest concentrations over the Sahara and Gobi deserts. However, emissions from South African, Australian, Patagonia, Arizona and Great Basin deserts are also clearly seen in the DU distribution. The largest model diversities (Fig. S10j) are found to be associated with long-range transport and deposition towards the poles and in the tropical Pacific, as well as with emissions from the Patagonia desert, which seem not to be well represented in all models.

# References


Adams, P. J. and Seinfeld, J. H.: Predicting global aerosol size distributions in general circulation models, J. Geophys. Res. Atmos., 107(19), 1–23, doi:10.1029/2001JD001010, 2002.

Albani, S., Mahowald, N. M., Perry, A. T., Scanza, R. A., Zender, C. S., Heavens, N. G., Maggi, V., Kok, J. F. and Otto-Bliesner, B. L.: Improved dust representation in the Community Atmosphere Model, J. Adv. Model. Earth Syst., 6(3), 541–570, doi:10.1002/2013MS000279, 2014.

Andres, R. J., and Kasgnoc, A. D.: A time-averaged inventory of subaerial volcanic sulfur emissions, J. Geophys. Res., 103(D19), 25251–25261, doi: 10.1029/98JD02091, 1998.

Astitha, M., Lelieveld, J., Abdel Kader, M., Pozzer, A. and De Meij, A.: Parameterization of dust emissions in the global atmospheric chemistry-climate model EMAC: Impact of nudging and soil properties, Atmos. Chem. Phys., 12(22), 11057–11083, doi:10.5194/acp-12-11057-2012, 2012.

Balkanski, Y. J., Jacob, D. J., Gardner, G. M., Graustein, W. C., and Turekian, K. K.: Transport and residence times of tropospheric aerosols inferred from a global three-dimensional simulation of 210Pb, J. Geophys. Res., 98, 20573–20586, 1993.

Bauer, S. E., Wright, D. L., Koch, D., Lewis, E. R., McGraw, R., Chang, L.-S., Schwartz, S. E. and Ruedy, R.: MATRIX (Multiconfiguration Aerosol TRacker of mIXing state): an aerosol microphysical module for global atmospheric models, Atmos. Chem. Phys., 8(20), 6003–6035, doi:10.5194/acp-8-6003-2008, 2008.

Bauer, S. E., & Menon, S.: Aerosol direct, indirect, semidirect, and surface albedo effects from sector contributions based on the IPCC AR5 emissions for preindustrial and present-day conditions. Journal of Geophysical Research Atmospheres, 117(1), 1–15. http://doi.org/10.1029/2011JD016816, 2012.

Bauer, S. E., Ault, A., & Prather, K. A.: Evaluation of aerosol mixing state classes in the GISS modelE-MATRIX climate model using single-particle mass spectrometry measurements. Journal of Geophysical Research Atmospheres, 118(17), 9834–9844. http://doi.org/10.1002/jgrd.50700, 2013.

Bey, I., D. J. Jacob, R. M. Yantosca, J. A. Logan, B. Field, A. M. Fiore, Q. Li, H. Liu, L. J. Mickley, and M. Schultz, Global modeling of tropospheric chemistry with assimilated meteorology: Model description and evaluation, J. Geophys. Res., 106, 23,073-23,096, 2001a.

Bergman, T., Makkonen, R., Schrödner, R., van Noije, T., et al.: Evaluation of a secondary organic aerosol scheme in TM5, in prep.

Bond, T. C., Bhardwaj, E., Dong, R., Jogani, R., Jung, S., Roden, C., … Trautmann, N. M.: Historical emissions of black and organic carbon aerosol from energy-related combustion, 1850-2000. Global Biogeochemical Cycles, 21(2). https://doi.org/10.1029/2006GB00284, 2007.

Cheng, T., Peng, Y., Feichter, J. and Tegen, I.: An improvement on the dust emission scheme in the global aerosol-climate model ECHAM5-HAM, Atmos. Chem. Phys., 8, https://doi.org/10.5194/acp-8-1105-2008, 1105– 1117, 2008.

Chin, M., M., D. J. J., Gardner, G. M., Foreman-Fowler, M. S., Spiro, P. A., and Savoie, D. L.: A global three-dimensional model of tropospheric sufate, J. Geophys. Res., 101, 18667– 18 690, 1996.

Croft, B., Lohmann, U., Martin, R. V., Stier, P., Wurzler, S., Feichter, J., Posselt, R., and Ferrachat, S.: Aerosol size-dependent below-cloud scavenging by rain and snow in the ECHAM5-HAM, Atmospheric Chemistry and Physics, 9, 4653–4675, 2009.

Croft, B., Lohmann, U., Martin, R. V., Stier, P., Wurzler, S., Feichter, J., Hoose, C., Heikkilä, U., van Donkelaar, A., and Ferrachat, S.: Influences of in-cloud aerosol scavenging parameterizations on aerosol concentrations and wet deposition in ECHAM5-HAM, Atmospheric Chemistry and Physics, 10, 1511–1543, 2010.

D'Andrea, S. D., Häkkinen, S. A. K., Westervelt, D. M., Kuang, C., Levin, E. J. T., Kanawade, V. P., Leaitch, W. R., Spracklen, D. V., Riipinen, I. and Pierce, J. R.: Understanding global secondary organic aerosol amount and size-resolved condensational behavior, Atmos. Chem. Phys., 13(22), 11519–11534, doi:10.5194/acp-13-11519-2013, 2013.

De Bruine, M., Krol, M., van Noije, T., Le Sager, P., and Röckmann, T.: The impact of precipitation evaporation on the atmospheric aerosol distribution in EC-Earth v3.2.0, Geosci. Model Dev., 11, 1443-1465, https://doi.org/10.5194/gmd-11-1443-2018, 2018.

Daskalakis, N., Myriokefalitakis, S. and Kanakidou, M.: Sensitivity of tropospheric loads and lifetimes of short lived pollutants to fire emissions, Atmos. Chem. Phys., 15(6), 3543–3563, doi:10.5194/acp-15-3543-2015, 2015.

Dentener, F., Kinne, S., Bond, T., Boucher, O., Cofala, J., Generoso, S., Ginoux, P., Gong, S., Hoelzemann, J. J., Ito, A., Marelli, L., Penner, J. E., Putaud, J. P., Textor, C., Schulz, M., Van Der Werf, G. R. and Wilson, J.: Emissions of primary aerosol and precursor gases in the years 2000 and 1750 prescribed data-sets for AeroCom, Atmos. Chem. Phys., 6(12), 4321–4344, doi:10.5194/acp-6-4321-2006, 2006.

Fountoukis, C. and Nenes, A.: ISORROPIA II: a computationally efficient thermodynamic equilibrium model for K+–Ca2+–Mg2+–NH4+–Na+–SO42−–NO3, Atmos. Chem. Phys., 7(17), 4639–4659, doi:10.5194/acp-7-4639-2007, 2007.

Ganzeveld, L., and Lelieveld J.: Dry deposition parameterization in a chemistry general circulation model and its influence on the distributionof reactive trace gases,J. Geophys. Res.,100, 20,999–21,012, 1995.

Ganzeveld, L., Lelieveld, J., and Roelofs, G. J.: Dry deposition parameterization of sulfur oxides in a chemistry and general circulation, J. Geophys. Res., 103, 5679–5694, doi:10.1029/97JD03077, 1998.

Ginoux, P., Chin, M., Tegen, I., Prospero, J. M., Holben, B., Dubovik, O. and Lin, S.-J.: Sources and distributions of dust aerosols simulated with the GOCART model, J. Geophys. Res. Atmos., 106(D17), 20255–20273, doi:10.1029/2000JD000053, 2001.

Gong, S. L.: A parameterization of sea-salt aerosol source function for sub- and super-micron particles, Global Biogeochem. Cycles, 17(4), n/a-n/a, doi:10.1029/2003GB002079, 2003.

Guelle, W., Balkanski, Y. J., Schulz, M., Dulac, F., and Monfray, P.: Wet deposition in a global size-dependent aerosol transport model: 1. Comparison of a 1 year 210Pb simulation with ground measurements, J. Geophys. Res., 103, 11429–11445, 1998.

Guenther, A., Karl, T., Harley, P., Wiedinmyer, C., Palmer, P. I. and C., G.: Estimates of global terrestrial isoprene emissions using MEGAN, Atmos. Chem. Phys., 6(1), 107–173, doi:10.5194/acpd-6-107-2006, 2006.

Heinold, B., Tegen, I., Schepanski, K. and Banks, J. R.: New developments in the representation of Saharan dust sources in the aerosol-climate model ECHAM6-HAM2, Geosci. Model Dev., 9(2), 765–777, doi:10.5194/gmd-9-765-2016, 2016.

Henzing, J. S., Olivi´e, D. J. L., and van Velthoven, P. F. J., A parameterization of size resolved below cloud scavenging of aerosol by rain, Atmos. Chem. Phys., 6, 3363–3375, doi:10.5194/acp-6-3363-2006, 2006.

Hoesly, R. M., Smith, S. J., Feng, L., Klimont, Z., Janssens-Maenhout, G., Pitkanen, T., Seibert, J. J., Vu, L., Andres, R. J., Bolt, R. M., Bond, T. C., Dawidowski, L., Kholod, N., Kurokawa, J.-I., Li, M., Liu, L., Lu, Z., Moura, M. C. P., O'Rourke, P. R. and Zhang, Q.: Historical (1750–2014) anthropogenic emissions of reactive gases and aerosols from the

Community Emissions Data System (CEDS), Geosci. Model Dev., 369-408, doi:10.5194/gmd-11-369-2018, 2018.

Hoose, C., Lohmann, U., Stier, P., Verheggen, B. and Weingartner, E.: Aerosol processing in mixed-phase clouds in ECHAM5-HAM: Model description and comparison to observations, J. Geophys. Res., 113(D7), D07210, doi:10.1029/2007JD009251, 2008a.

Hoose, C., Lohmann, U., Bennartz, R., Croft, B. and Lesins, G.: Global simulations of aerosol processing in clouds, Atmos. Chem. Phys., 8(23), 6939–6963, doi:10.5194/acp-8-6939-2008, 2008b.

Horowitz, L. W., Walters, S., Mauzerall, D. L., Emmons, L. K., Rasch, P. J., Granier, C., Tie, X., Lamarque, J.-F., Schultz, M. G., Tyndall, G. S., Orlando, J. J. and Brasseur, G. P.: A global simulation of tropospheric ozone and related tracers: Description and evaluation of MOZART, version 2, J. Geophys. Res. Atmos., 108(D24), n/a-n/a, doi:10.1029/2002JD002853, 2003.

Huijnen, V., Williams, J., Van Weele, M., Van Noije, T., Krol, M., Dentener, F., Segers, a., Houweling, S., Peters, W., De Laat, J., Boersma, F., Bergamaschi, P., Van Velthoven, P., Le Sager, P., Eskes, H., Alkemade, F., Scheele, R., Nédélec, P. and Pätz, H. W.: The global chemistry transport model TM5: Description and evaluation of the tropospheric chemistry version 3.0, Geosci. Model Dev., 3(2), 445–473, doi:10.5194/gmd-3-445-2010, 2010.

Jacob, D. J., Liu, H., Mari, C., and Yantosca, B. M.: Harvard wet deposition scheme for GMI, acmg.seas.harvard.edu/geos/wiki_docs/deposition/wetdep.jacob_etal_2000.pdf, 2000.

Jaeglé, L., Quinn, P. K., Bates, T. S., Alexander, B., & Lin, J.-T.: Global distribution of sea salt aerosols: new constraints from in situ and remote sensing observations. Atmospheric Chemistry and Physics, 11(7), 3137–3157. https://doi.org/10.5194/acp-11-3137-2011, 2011.

Jeuken, A., Veefkind, J. P., Dentener, F., Metzger, S., and Gonzalez, C. R.: Simulation of the aerosol optical depth over Europe for August 1997 and a comparison with observations, J. Geophys. Res., 106, 28295–28311, 2001.

Jöckel, P., Kerkweg, A., Pozzer, A., Sander, R., Tost, H., Riede, H., Baumgaertner, A., Gromov, S. and Kern, B.: Development cycle 2 of the Modular Earth Submodel System (MESSy2), Geosci. Model Dev., 3(2), 717–752, doi:10.5194/gmd-3-717-2010, 2010.

Jokinen T., Berndt T., Makkonen R., Kerminen V.-M., Junninen H., Paasonen P., Stratmann F., Herrmann H., Guenther A.B., Worsnop D.R., Kulmala M., Ehn M., Sipilä M., Production of extremely low volatile organic compounds from biogenic emissions: Measured yields and atmospheric implications, PNAS, 112 (23) 7123-7128, 2015

Kanakidou, M., Duce, R. A., Prospero, J. M., Baker, A. R., Benitez-Nelson, C., Dentener, F. J., Hunter, K. A., Liss, P. S., Mahowald, N., Okin, G. S., Sarin, M., Tsigaridis, K., Uematsu, M., Zamora, L. M. and Zhu, T.: Atmospheric fluxes of organic N and P to the global ocean, Global Biogeochem. Cycles, 26(3), 1–12, doi:10.1029/2011GB004277, 2012.

Karset, I. H. H., Berntsen, T. K., Storelvmo, T., Alterskjær, K., Grini, A., Olivié, D., Kirkevåg, A., Seland, Ø., Iversen, T., and Schulz, M.: Strong impacts on aerosol indirect effects from historical oxidant changes, Atmos. Chem. Phys., 18, 7669–7690, https://doi.org/10.5194/acp-18-7669-2018, 2018.

Karydis, V. A., Tsimpidi, A. P., Pozzer, A., Astitha, M. and Lelieveld, J.: Effects of mineral dust on global atmospheric nitrate concentrations, Atmos. Chem. Phys., 16(3), 1491–1509, doi:10.5194/acp-16-1491-2016, 2016.

Karydis, V. A., Tsimpidi, A. P., Bacer, S., Pozzer, A., Nenes, A., & Lelieveld, J. : Global impact of mineral dust on cloud droplet number concentration. Atmospheric Chemistry and Physics, 17(9), 5601–5621. http://doi.org/10.5194/acp-17-5601-2017, 2017.

Kazil, J. and Lovejoy, E. R.: A semi-analytical method for calculating rates of new sulphate aerosol formation from the gas phase, Atmos. Chem. Phys., 7(13), 3447–3459, doi:10.5194/acp-7-3447-2007, 2007.

Kazil, J., Stier, P., Zhang, K., Quaas, J., Kinne, S., O'Donnell, D., Rast, S., Esch, M., Ferrachat, S., Lohmann, U. and Feichter, J.: Aerosol nucleation and its role for clouds and Earth's radiative forcing in the aerosol-climate model ECHAM5-HAM, Atmos. Chem. Phys., 10(22), 10733–10752, doi:10.5194/acp-10-10733-2010, 2010.

Keller, C. A., Long, M. S., Yantosca, R. M., Da Silva, A. M., Pawson, S. and Jacob, D. J.: HEMCO v1.0: a versatile, ESMF-compliant component for calculating emissions in atmospheric models, Geosci. Model Dev., 7(4), 1409–1417, doi:10.5194/gmd-7-1409-2014, 2014.

Kerkweg, A., Buchholz, J., Ganzeveld, L., Pozzer, A., Tost, H., and Jöckel, P.: Technical Note: An implementation of the dry removal processes DRY DEPosition and SEDImentation in the Modular Earth Submodel System (MESSy), Atmos. Chem. Phys., 6, 4617-4632, https://doi.org/10.5194/acp-6-4617-2006, 2006.

Kirkevåg, A., A. Grini, D. Olivié, Ø. Seland, K. Alterskjær, M. Hummel, I. H. H. Karset, A. Lewinschal, X. Liu, R.

Makkonen, I. Bethke, J. Griesfeller, M. Schulz, T. Iversen: A production-tagged aerosol module for Earth system models, OsloAero5.3 – extensions and updates for CAM5.3-Oslo, Geosci. Model Dev., 11, 3945-3982, https://doi.org/10.5194/gmd-11-3945-2018, 2018.

Klingmüller, K., Metzger, S., Abdelkader, M., Karydis, V. A., Stenchikov, G. L., Pozzer, A. and Lelieveld, J.: Revised mineral dust emissions in the atmospheric chemistry-climate model EMAC (based on MESSy 2.52), Geosci. Model Dev., 11, 989-1008, doi:10.5194/gmd-11-989-2018, 2018.

Koch, D., Jacob, D., Tegen, I., Rind, D., and Chin, M.: Tro- pospheric sulfur simulation and sulfate direct radiative forcing in the Goddard Institute for Space Studies general circulation model, J. Geophys. Res., 104, 23 799–23 822, 1999.

Koch, D., Schmidt, G., and Field, C.: Sulfur, sea salt and ra- dionuclide aerosols in the GISS modelE, J. Geophys. Res., 111, D06206, doi:10.1029/2004JD005550, 2006.

Kodros, J. K., Cucinotta, R., Ridley, D. A., Wiedinmyer, C., & Pierce, J. R. (2016). The aerosol radiative effects of uncontrolled combustion of domestic waste. Atmospheric Chemistry and Physics, 16(11), 6771–6784. http://doi.org/10.5194/acp-16-6771-2016

Kokkola, H., Hommel, R., Kazil, J., Niemeier, U., Partanen, A.-I., Feichter, J. and Timmreck, C.: Aerosol microphysics modules in the framework of the ECHAM5 climate model – intercomparison under stratospheric conditions, Geosci. Model Dev., 2(2), 97–112, doi:10.5194/gmd-2-97-2009, 2009.

Kulmala, M., Lehtinen, K. E. J. and Laaksonen, A.: Cluster activation theory as an explanation of the linear dependence between formation rate of 3nm particles and sulphuric acid concentration, Atmos. Chem. Phys., 6(3), 787–793, doi:10.5194/acp-6-787-2006, 2006.

Lamarque, J.-F., Emmons, L. K., Hess, P. G., Kinnison, D. E., Tilmes, S., Vitt, F., Heald, C. L., Holland, E. A., Lauritzen, P. H., Neu, J., Orlando, J. J., Rasch, P. J. and Tyndall, G. K.: CAM-chem: description and evaluation of interactive atmospheric chemistry in the Community Earth System Model, Geosci. Model Dev., 5(2), 369–411, doi:10.5194/gmd-5-369-2012, 2012.

Lamarque, J. F., Bond, T. C., Eyring, V., Granier, C., Heil, A., Klimont, Z., Lee, D., Liousse, C., Mieville, A., Owen, B., Schultz, M. G., Shindell, D., Smith, S. J., Stehfest, E., Van Aardenne, J., Cooper, O. R., Kainuma, M., Mahowald, N., McConnell, J. R., Naik, V., Riahi, K. and Van Vuuren, D. P.: Historical (1850-2000) gridded anthropogenic and biomass burning emissions of reactive gases and aerosols: Methodology and application, Atmos. Chem. Phys., 10(15), 7017–7039, doi:10.5194/acp-10-7017-2010, 2010.

Lamarque, J. F., Shindell, D. T., Josse, B., Young, P. J., Cionni, I., Eyring, V., Bergmann, D., Cameron-Smith, P., Collins, W. J., Doherty, R., Dalsoren, S., Faluvegi, G., Folberth, G., Ghan, S. J., Horowitz, L. W., Lee, Y. H., MacKenzie, I. A., Nagashima, T., Naik, V., Plummer, D., Righi, M., Rumbold, S. T., Schulz, M., Skeie, R. B., Stevenson, D. S., Strode, S., Sudo, K., Szopa, S., Voulgarakis, A. and Zeng, G.: The atmospheric chemistry and climate model intercomparison Project (ACCMIP): Overview and description of models, simulations and climate diagnostics, Geosci. Model Dev., 6(1), 179–206, doi:10.5194/gmd-6-179-2013, 2013.

Lee, Y. H. and Adams, P. J.: A Fast and Efficient Version of the TwO-Moment Aerosol Sectional (TOMAS) Global Aerosol Microphysics Model, Aerosol Sci. Technol., 46(6), 678–689, doi:10.1080/02786826.2011.643259, 2012.

Lee, Y. H., Adams, P. J. and Shindell, D. T.: Evaluation of the global aerosol microphysical ModelE2-TOMAS model against satellite and ground-based observations, Geosci. Model Dev., 8(3), 631–667, doi:10.5194/gmd-8-631-2015, 2015.

Liu, X., Easter, R. C. C., Ghan, S. J. J., Zaveri, R., Rasch, P., Shi, X., Lamarque, J.-F. F., Gettelman, A., Morrison, H., Vitt, F., Conley, A., Park, S., Neale, R., Hannay, C., Ekman, A. M. L. M. L., Hess, P., Mahowald, N., Collins, W., Iacono, M. J. J., Bretherton, C. S. S., Flanner, M. G. G. and Mitchell, D.: Toward a minimal representation of aerosols in climate models: Description and evaluation in the Community Atmosphere Model CAM5, Geosci. Model Dev., 5(3), 709–739, doi:10.5194/gmd-5-709-2012, 2012.

Liu, X., Ma, P.-L. L., Wang, H., Tilmes, S., Singh, B., Easter, R. C., Ghan, S. J. and Rasch, P. J.: Description and evaluation of a new four-mode version of the Modal Aerosol Module (MAM4) within version 5.3 of the Community Atmosphere Model, Geosci. Model Dev., 9(2), 505–522, doi:10.5194/gmd-9-505-2016, 2016.

Lohmann, U., & Neubauer, D.: The importance of mixed-phase and ice clouds for climate sensitivity in the global aerosol-climate model ECHAM6-HAM2. Atmospheric Chemistry and Physics, 18(12), 8807–8828. http://doi.org/10.5194/acp-18-8807-2018, 2018.

Long, M. S., Keene, W. C., Kieber, D. J., Erickson, D. J. and Maring, H.: A sea-state based source function for size- and

composition-resolved marine aerosol production, Atmos. Chem. Phys., 11(3), 1203–1216, doi:10.5194/acp-11-1203-2011, 2011.

Luo, G., and F. Yu, Representation of cloud droplet number concentration in the Community Atmosphere Model with Chemistry and the Advanced Particle Microphysics (CAM-Chem/APM), in preparation.

Mahowald, N. M., Muhs, D. R., Levis, S., Rasch, P. J., Yoshioka, M., Zender, C. S. and Luo, C.: Change in atmospheric mineral aerosols in response to climate: Last glacial period, preindustrial, modern, and doubled carbon dioxide climates, J. Geophys. Res. Atmos., 111(D10), n/a-n/a, doi:10.1029/2005JD006653, 2006.

Mann, G. W., Carslaw, K. S., Reddington, C. L., Pringle, K. J., Schulz, M., Asmi, A., Spracklen, D. V., Ridley, D. A., Woodhouse, M. T., Lee, L. A., Zhang, K., Ghan, S. J., Easter, R. C., Liu, X., Stier, P., Lee, Y. H., Adams, P. J., Tost, H., Lelieveld, J., Bauer, S. E., Tsigaridis, K., Van Noije, T. P. C., Strunk, A., Vignati, E., Bellouin, N., Dalvi, M., Johnson, C. E., Bergman, T., Kokkola, H., Von Salzen, K., Yu, F., Luo, G., Petzold, A., Heintzenberg, J., Clarke, A., Ogren, J. A., Gras, J., Baltensperger, U., Kaminski, U., Jennings, S. G., O'Dowd, C. D., Harrison, R. M., Beddows, D. C. S., Kulmala, M., Viisanen, Y., Ulevicius, V., Mihalopoulos, N., Zdimal, V., Fiebig, M., Hansson, H. C., Swietlicki, E. and Henzing, J. S.: Intercomparison and evaluation of global aerosol microphysical properties among AeroCom models of a range of complexity, Atmos. Chem. Phys., 14(9), 4679–4713, doi:10.5194/acp-14-4679-2014, 2014.

Mårtensson, E. M., Nilsson, E. D., de Leeuw, G., Cohen, L. H. and Hansson, H.-C.: Laboratory simulations and parameterization of the primary marine aerosol production, J. Geophys. Res. Atmos., 108(D9), n/a-n/a, doi:10.1029/2002JD002263, 2003.

Matsui, H., Koike, M., Kondo, Y., Takami, A., Fast, J. D., Kanaya, Y., & Takigawa, M.: Volatility basis-set approach simulation of organic aerosol formation in East Asia: Implications for anthropogenic-biogenic interaction and controllable amounts. Atmospheric Chemistry and Physics, 14(18), 9513–9535. http://doi.org/10.5194/acp-14-9513-2014, 2014.

Matsui, H.: Development of a global aerosol model using a two-dimensional sectional method : 1 . Model design, J. Adv. Model. Earth Syst., 9, 1921–1947, doi:10.1002/2017MS000936, 2017.

Matsui, H. and Mahowald, N.: Development of a global aerosol model using a two-dimensional sectional method: 2. Evaluation and sensitivity simulations, J. Adv. Model. Earth Syst., 9(4), 1887–1920, doi:10.1002/2017MS000937, 2017.

Mihalopoulos, N., Kerminen, V. M., Kanakidou, M., Berresheim, H. and Sciare, J.: Formation of particulate sulfur species (sulphate and methanesulfonate) during summer over the Eastern Mediterranean: A modelling approach, Atmos. Environ., 41(32), 6860–6871, doi:10.1016/j.atmosenv.2007.04.039, 2007.

Monahan, E. C., Spiel, D. E. and Davidson, K. L.: A Model of Marine Aerosol Generation Via Whitecaps and Wave Disruption, pp. 167–174, Springer Netherlands., 1986.

Myriokefalitakis, S., Tsigaridis, K., Mihalopoulos, N., Sciare, J., Nenes, A., Kawamura, K., Segers, A. and Kanakidou, M.: In-cloud oxalate formation in the global troposphere: A 3-D modeling study. *Atmos. Chem. Phys.*, 11, 5761-5782, doi:10.5194/acp-11-5761, 2011.

Myriokefalitakis, S., Daskalakis, N., Mihalopoulos, N., Baker, A. R., Nenes, A., and Kanakidou, M.: Changes in dissolved iron deposition to the oceans driven by human activity: a 3-D global modelling study, Biogeosciences, 12, 3973-3992, https://doi.org/10.5194/bg-12-3973-2015, 2015.

Napari, I., Kulmala, M. and Vehkamäki, H.: Ternary nucleation of inorganic acids, ammonia, and water, J. Chem. Phys., 117(18), 8418–8425, doi:10.1063/1.1511722, 2002.

Neale, R. B., Gettelman, A., Park, S., Chen, C.-C., Lauritzen, P. H., Williamson, D. L., Conley, A. J., Kinnison, D., Marsh, D., Smith, A. K., Vitt, F., Garcia, R., Lamarque, J.-F., Mills, M., Tilmes, S., Morrison, H., Cameron-smith, P., Collins, W. D., Iacono, M. J., Easter, R. C., Liu, X., Ghan, S. J., Rasch, P. J. and Taylor, M. A.: Description of the NCAR Community Atmosphere Model (CAM 5.0). NCAR Technical Notes., NCAR/Tn-464+Str, 214, doi:10.5065/D6N877R0., 2012.

Nenes, A. and Seinfeld, J. H.: Parameterization of cloud droplet formation in global climate models, J. Geophys. Res. Atmos., 108(D14), 4415, doi:10.1029/2002JD002911, 2003.

Neu, J. L. and Prather, M. J.: Toward a more physical representation of precipitation scavenging in global chemistry models: cloud overlap and ice physics and their impact on tropospheric ozone, Atmos. Chem. Phys., 12, 3289-3310, doi:10.5194/acp-12-3289-2012, 2012.

Neubauer, D., Lohmann, U., Hoose, C. and Frontoso, M. G.: Impact of the representation of marine stratocumulus clouds on

the anthropogenic aerosol effect, Atmos. Chem. Phys., 14(21), 11997–12022, doi:10.5194/acp-14-11997-2014, 2014.

Neubauer, D., Ferrachat, S., Siegenthaler-Le Drian, C., Stier, P., Partridge, P. D., Tegen, I., Bey, I., Stanelle, T., Kokkola, H., and Lohmann, U.: Cloud evaluation, aerosol radiative forcing and climate sensitivity in the global aerosol-climate model ECHAM6.3-HAM2.3, submitted to ACPD 2018.

Paasonen, P., Nieminen, T., Asmi, E., Manninen, H. E., Petäjä, T., Plass-Dülmer, C., Flentje, H., Birmili, W., Wiedensohler, A., Hõrrak, U., Metzger, A., Hamed, A., Laaksonen, A., Facchini, M. C., Kerminen, V.-M. and Kulmala, M.: On the roles of sulphuric acid and low-volatility organic vapours in the initial steps of atmospheric new particle formation, Atmos. Chem. Phys., 10(22), 11223–11242, doi:10.5194/acp-10-11223-2010, 2010.

Petters, M. D. and Kreidenweis, S. M.: A single parameter representation of hygroscopic growth and cloud\ncondensation nucleus activity, Atmos. Chem. Phys., 1961–1971, doi:10.5194/acp-7-1961-2007, 2007.

Petters, M. D., Kreidenweis, S. M., Sandu, A., Verwer, J. G., van Loon, M., Carmichael, G. R., Potra, F. A., Dabdub, D. and Seinfeld, J. H.: A single parameter representation of hygroscopic growth and cloud condensation nucleus activity, Atmos. Chem. Phys., 7(8), 1961–1971, doi:10.5194/acp-7-1961-2007, 2007.

Pringle, K. J., Tost, H., Message, S., Steil, B., Giannadaki, D., Nenes, A., Fountoukis, C., Stier, P., Vignati, E. and Lelieveld, J.: Description and evaluation of GMXe: A new aerosol submodel for global simulations (v1), Geosci. Model Dev., 3(2), 391–412, doi:10.5194/gmd-3-391-2010, 2010a.

Pringle, K. J., Tost, H., Pozzer, A., Pöschl, U. and Lelieveld, J.: Global distribution of the effective aerosol hygroscopicity parameter for CCN activation, Atmos. Chem. Phys., 10(12), 5241–5255, doi:10.5194/acp-10-5241-2010, 2010b.

Rasch, P. J., Feichter, J., and Law, K.: A comparison of scavenging and deposition processes in global models: results from the WCRP Cambridge Workshop of 1995, Tellus, 52B, 1025–1056, 2000.

Riahi, K., Grübler, A. and Nakicenovic, N.: Scenarios of long-term socio-economic and environmental development under climate stabilization, Technol. Forecast. Soc. Change, 74(7), 887–935, doi:10.1016/j.techfore.2006.05.026, 2007.

Riccobono, F., Schobesberger, S., Scott, C. E., Dommen, J., Ortega, I. K., Rondo, L., Almeida, J., Amorim, A., Bianchi, F., Breitenlechner, M., David, A., Downard, A., Dunne, E. M., Duplissy, J., Ehrhart, S., Flagan, R. C., Franchin, A., Hansel, A., Junninen, H., Kajos, M., Keskinen, H., Kupc, A., Kürten, A., Kvashin, A. N., Laaksonen, A., Lehtipalo, K., Makhmutov, V., Mathot, S., Nieminen, T., Onnela, A., Petäjä, T., Praplan, A. P., Santos, F. D., Schallhart, S., Seinfeld, J. H., Sipilä, M., Spracklen, D. V., Stozhkov, Y., Stratmann, F., Tomé, A., Tsagkogeorgas, G., Vaattovaara, P., Viisanen, Y., Vrtala, A., Wagner, P. E., Weingartner, E., Wex, H., Wimmer, D., Carslaw, K. S., Curtius, J., Donahue, N. M., Kirkby, J., Kulmala, M., Worsnop, D. R. and Baltensperger, U.: Oxidation products of biogenic emissions contribute to nucleation of atmospheric particles, Science., 344, 717–721, doi:10.1126/science.1243527, 2014a.

Roelofs, G.-J. and Lelieveld, J.: Distribution and budget of O3 in the troposphere calculated with a chemistry general circulation model, J. Geophys. Res., 100, 20983–20998, 1995.

Salisbury, D. J., Anguelova, M. D., and Brooks, I. M.: On the vari-ability of whitecap fraction using satellite-basedobservations, J. Geophys. Res., 118, 6201–6222, doi:10.1002/2013JC008797, 2013

Salter, M. E., Zieger, P., Acosta Navarro, J. C., Grythe, H., Kirkevåg, A., Rosati, B., Riipinen, I., and Nilsson, E. D.: An empirically derived inorganic sea spray source function incorpo- rating sea surface temperature, Atmos. Chem. Phys., 15, 11047–11066, doi:10.5194/acp-15-11047-2015, 2015.

Scanza, R. A., Mahowald, N., Ghan, S., Zender, C. S., Kok, J. F., Liu, X., Zhang, Y. and Albani, S.: Modeling dust as component minerals in the Community Atmosphere Model: development of framework and impact on radiative forcing, Atmos. Chem. Phys., 15(1), 537–561, doi:10.5194/acp-15-537-2015, 2015.

Schmale, J., Henning, S., Henzing, B., Keskinen, H., Sellegri, K., Ovadnevaite, J., Schlag, P.: Data Descriptor : Collocated observations of cloud condensation nuclei , particle size distributions , and chemical composition, 1–26, 2017.

Schmale, J., Henning, S., Decesari, S., Henzing, B., Keskinen, H., Sellegri, K., Gysel, M.: Long-term cloud condensation nuclei number concentration, particle number size distribution and chemical composition measurements at regionally representative observatories. Atmospheric Chemistry and Physics, 18(4), 2853–2881. http://doi.org/10.5194/acp-18-2853-2018, 2018.

Schmidt, G. A., Kelley, M., Nazarenko, L., Ruedy, R., Russell, G. L., Aleinov, I., Bauer, M., Bauer, S. E., Bhat, M. K., Bleck, R., Canuto, V., Chen, Y.-H., Cheng, Y., Clune, T. L., Del Genio, A., de Fainchtein, R., Faluvegi, G., Hansen, J. E., Healy, R. J., Kiang, N. Y., Koch, D., Lacis, A. A., LeGrande, A. N., Lerner, J., Lo, K. K., Matthews, E. E., Menon, S., Miller, R. L., Oinas, V., Oloso, A. O., Perlwitz, J. P., Puma, M. J., Putman, W. M., Rind, D., Romanou, A., Sato, M.,

Shindell, D. T., Sun, S., Syed, R. A., Tausnev, N., Tsigaridis, K., Unger, N., Voulgarakis, A., Yao, M.-S. and Zhang, J.: Configuration and assessment of the GISS ModelE2 contributions to the CMIP5 archive, J. Adv. Model. Earth Syst., 6(1), 141–184, doi:10.1002/2013MS000265, 2014.

Seinfeld, J. H. and Pandis, S. N.: Atmospheric Chemistry and Physics: From Air Pollution to Climate Change, 1st edition, J. Wiley, New York. 1998.

Seinfeld, J. and Pandis, S.: Atmospheric Chemistry and Physics: From Air Pollution to Climate Change., J Wiley, New York, 2006.

Seland, Ø., Iversen, T., Kirkevåg, A., and Storelvmo, T.: Aerosol - climate interactions in the CAM-Oslo atmospheric GCM and investigations of associated shortcomings, Tellus A, 60, 459–491, 2008

Shindell, D. T., Faluvegi, G., Unger, N., Aguilar, E., Schmidt, G. A., Koch, D. M., Bauer, S. E., and Miller, R. L.: Simulations of preindustrial, present-day, and 2100 conditions in the NASA GISS composition and climate model G-PUCCINI, Atmos. Chem. Phys., 6, 4427-4459, https://doi.org/10.5194/acp-6-4427-2006, 2006.

Sindelarova, K., Granier, C., Bouarar, I., Guenther, A., Tilmes, S., Stavrakou, T., Müller, J.-F., Kuhn, U., Stefani, P., and Knorr, W.: Global data set of biogenic VOC emissions calculated by the MEGAN model over the last 30 years, Atmos. Chem. Phys., 14, 9317–9341, http://doi.org/10.5194/acp-14-9317-2014, 2014.

Sofiev, M., Soares, J., Prank, M., De Leeuw, G. and Kukkonen, J.: A regional-to-global model of emission and transport of sea salt particles in the atmosphere, J. Geophys. Res. Atmos., 116(21), doi:10.1029/2010JD014713, 2011.

Stier, P., Feichter, J., Kinne, S., Kloster, S., Vignati, E., Wilson,J., Ganzeveld, L., Tegen, I., Werner, M., Schulz, M., Balkanski, Y., Boucher, O., Minikin, A., and Petzold, A.: The aerosol-climate model ECHAM5-HAM, Atmos. Chem. Phys., 5, 1125–1165, 2005.

Stevens, B., Giorgetta, M., Esch, M., Mauritsen, T., Crueger, T., Rast, S., Salzmann, M., Schmidt, H., Bader, J., Block, K., Brokopf, R., Fast, I., Kinne, S., Kornblueh, L., Lohmann, U., Pincus, R., Reichler, T. and Roeckner, E.: Atmospheric component of the MPI-M earth system model: ECHAM6, J. Adv. Model. Earth Syst., 5(2), 146–172, doi:10.1002/jame.20015, 2013.

Tegen, I., Harrison, S. P., Kohfeld, K., Prentice, I. C., Coe, M. and Heimann, M.: Impact of vegetation and preferential source areas on global dust aerosol: Results from a model study, J. Geophys. Res. Atmos., 107(21), doi:10.1029/2001JD000963, 2002.

Tegen, I., Neubauer, D., Ferrachat, S., Siegenthaler-Le Drian, C., Bey, I., Schutgens, N., Stier, P., Watson-Parris, D., Stanelle, T., Schmidt, H., Rast, S., Kokkola, H., Schultz, M., Schroeder, S., Daskalakis, N., Barthel, S., Heinold, B., and Lohmann, U.: The global aerosol–climate model ECHAM6.3–HAM2.3 – Part 1: Aerosol evaluation, Geosci. Model Dev., 12, 1643-1677, https://doi.org/10.5194/gmd-12-1643-2019, 2019.

Tost, H., Jöckel, P., Kerkweg, A., Sander, R., and Lelieveld, J.: Technical note: A new comprehensive SCAVenging submodel for global atmospheric chemistry modelling, Atmos. Chem. Phys., 6, 565-574, https://doi.org/10.5194/acp-6-565-2006, 2006.

Trivitayanurak, W., Adams, P. J., Spracklen, D. V., & Carslaw, K. S. : Tropospheric aerosol microphysics simulation with assimilated meteorology: Model description and intermodel comparison. Atmospheric Chemistry and Physics, 8(12), 3149–3168. http://doi.org/10.5194/acp-8-3149-2008, 2008.

Tsigaridis, K. and Kanakidou, M.: Global modelling of secondary organic aerosol in the troposphere: a sensitivity analysis, Atmos. Chem. Phys., 3(5), 1849–1869, doi:10.5194/acp-3-1849-2003, 2003.

Tsigaridis, K. and Kanakidou, M.: Secondary organic aerosol importance in the future atmosphere, Atmos. Environ., 41(22), 4682–4692, doi:http://dx.doi.org/10.1016/j.atmosenv.2007.03.045, 2007.

Tsigaridis, K., Krol, M., Dentener, F.J., Balkanski, Y., Lathière, J., Metzger, S., Hauglustaine, D.A. and Kanakidou, M.: Change in global aerosol composition since preindustrial times. Atmos. Chem. Phys., 6, 5143-5162, doi:10.5194/acp-6-5143, 2006.

Tsigaridis, K., Daskalakis, N., Kanakidou, M., Adams, P. J., Artaxo, P., Bahadur, R., Balkanski, Y., Bauer, S. E., Bellouin, N., Benedetti, A., Bergman, T., Berntsen, T. K., Beukes, J. P., Bian, H., Carslaw, K. S., Chin, M., Curci, G., Diehl, T., Easter, R. C., Ghan, S. J., Gong, S. L., Hodzic, A., Hoyle, C. R., Iversen, T., Jathar, S., Jimenez, J. L., Kaiser, J. W., Kirkevåg, A., Koch, D., Kokkola, H., Lee, Y. H., Lin, G., Liu, X., Luo, G., Ma, X., Mann, G. W., Mihalopoulos, N., Morcrette, J.-J., Müller, J.-F., Myhre, G., Myriokefalitakis, S., Ng, N. L., O'Donnell, D., Penner, J. E., Pozzoli, L., Pringle, K. J., Russell, L. M., Schulz, M., Sciare, J., Seland, Ø., Shindell, D. T., Sillman, S., Skeie, R. B., Spracklen, D.,

Stavrakou, T., Steenrod, S. D., Takemura, T., Tiitta, P., Tilmes, S., Tost, H., van Noije, T., van Zyl, P. G., von Salzen, K., Yu, F., Wang, Z., Wang, Z., Zaveri, R. A., Zhang, H., Zhang, K., Zhang, Q. and Zhang, X.: The AeroCom evaluation and intercomparison of organic aerosol in global models, Atmos. Chem. Phys., 14(19), 10845–10895, doi:10.5194/acp-14-10845-2014, 2014.

Van Marle, M. J. E., Kloster, S., Magi, B. I., Marlon, J. R., Daniau, A.-L., Field, R. D., Arneth, A., Forrest, M., Hantson, S., Kehrwald, N. M., Knorr, W., Lasslop, G., Li, F., Mangeon, S., Yue, C., Kaiser, J. W. and van der Werf, G. R.: Historic global biomass burning emissions based on merging satellite observations with proxies and fire models (1750–2015), Geosci. Model Dev., 3329-3357, doi:10.5194/gmd-10-3329-2017, 2017.

Val Martin, M., Logan, J. A., Kahn, R. A., Leung, F.-Y., Nelson, D. L., and Diner, D. J.: Smoke injection heights from fires in North America: analysis of 5 years of satellite observations, Atmospheric Chemistry and Physics, 10, 1491–1510, 2010.

Van Noije, T. P. C., Le Sager, P., Segers, A. J., Van Velthoven, P. F. J., Krol, M. C., Hazeleger, W., Williams, A. G. and Chambers, S. D.: Simulation of tropospheric chemistry and aerosols with the climate model EC-Earth, Geosci. Model Dev., 7, 2435–2475, doi:10.5194/gmd-7-2435-2014, 2014.

Vehkamäki, H.: An improved parameterization for sulfuric acid–water nucleation rates for tropospheric and stratospheric conditions, J. Geophys. Res., 107(D22), 4622, doi:10.1029/2002JD002184, 2002.

Vignati, E., Wilson, J. and Stier, P.: M7: An efficient size-resolved aerosol microphysics module for large-scale aerosol transport models, J. Geophys. Res. Atmos., 109(D22), n/a-n/a, doi:10.1029/2003JD004485, 2004.

Vignati, E., Facchini, M. C., Rinaldi, M., Scannell, C., Ceburnis, D., Sciare, J., Kanakidou, M., Myriokefalitakis, S., Dentener, F. and O'Dowd, C. D.: Global scale emission and distribution of sea-spray aerosol: Sea-salt and organic enrichment, Atmos. Environ., 44(5), 670–677, doi:10.1016/j.atmosenv.2009.11.013, 2010.

Wang, Q., D.J. Jacob, J.A. Fisher, J. Mao, E.M. Leibensperger, C.C. Carouge, P. Le Sager, Y. Kondo, J.L. Jimenez, M.J. Cubison, and S.J. Doherty, Sources of carbonaceous aerosols and deposited black carbon in the Arctic in winter-spring: implications for radiative forcing, Atmos. Chem. Phys., 11, 12,453-12,473, 2011.

Wang, H., Easter, R. C., Rasch, P. J., Wang, M., Liu, X., Ghan, S. J., Qian, Y., Yoon, J.-H., Ma, P.-L. and Vinoj, V.: Sensitivity of remote aerosol distributions to representation of cloud–aerosol interactions in a global climate model, Geosci. Model Dev., 6(3), 765–782, doi:10.5194/gmd-6-765-2013, 2013.

Wiedinmyer, C., Akagi, S. K., Yokelson, R. J., Emmons, L. K., Al-Saadi, J. A., Orlando, J. J., & Soja, A. J.: The Fire INventory from NCAR (FINN): a high resolution global model to estimate the emissions from open burning. Geoscientific Model Development, 4(3), 625–641. https://doi.org/10.5194/gmd-4-625-2011, 2011.

Wesely, M. L.: Parameterization of surface resistances to gaseous dry deposition in regional-scale numerical models, Atmos. Env-iron., 23, 1293–1304, 1989

Westervelt, D. M., Pierce, J. R., Riipinen, I., Trivitayanurak, W., Hamed, A., Kulmala, M., Laaksonen, A., Decesari, S., and Adams, P. J.: Formation and growth of nucleated particles into cloud condensation nuclei: model-measurement comparison, Atmospheric Chemistry and Physics, 13, 7645-7663, doi:10.5194/acp-13-7645-2013, 2013.

Yang, Y., Wang, H., Smith, S. J., Ma, P.-L. and Rasch, P. J.: Source attribution of black carbon and its direct radiative forcing in China, Atmos. Chem. Phys., 17(6), 4319–4336, doi:10.5194/acp-17-4319-2017, 2017.

Yu, F.: A secondary organic aerosol formation model considering successive oxidation aging and kinetic condensation of organic compounds: Global scale implications, Atmos. Chem. Phys., 11(3), 1083–1099, doi:10.5194/acp-11-1083-2011, 2011.

Yu, F. and Luo, G.: Simulation of particle size distribution with a global aerosol model: contribution of nucleation to aerosol and CCN number concentrations, Atmos. Chem. Phys. 9, 7691-7710, https://doi.org/10.5194/acp-9-7691-2009, 2009.

Yu, F., Nadykto, A. B., Herb, J., Luo, G., Nazarenko, K. M., and Uvarova, L. A.: H2SO4-H2O-NH3 ternary ion-mediated nucleation (TIMN): Kinetic-based model and comparison with CLOUD measurements, Atmos. Chem. Phys. Discuss., https://doi.org/10.5194/acp-2018-396, in review, 2018.

Zender, C. S., Bian, H. and Newman, D.: Mineral Dust Entrainment and Deposition (DEAD) model: Description and 1990s dust climatology, J. Geophys. Res., 108(D14), 4416, doi:10.1029/2002JD002775, 2003.

Zhang, L. M., Gong, S. L., Padro, J., and Barrie, L.: A size-segregated particle dry deposition scheme for an atmospheric aerosol module, Atmos. Environ., 35(3), 549-560, doi:10.1016/s1352-2310(00)00326-5, 2001.

Zhang, K., O'Donnell, D., Kazil, J., Stier, P., Kinne, S., Lohmann, U., Ferrachat, S., Croft, B., Quaas, J., Wan, H., Rast, S.

and Feichter, J.: The global aerosol-climate model ECHAM-HAM, version 2: Sensitivity to improvements in process representations, Atmos. Chem. Phys., 12(19), 8911–8949, doi:10.5194/acp-12-8911-2012, 2012.

# Supplementary figures captions

The following figures can be found in a separate file:

**Fig. S1.** Monthly averages of the mass concentration of sulphate ($SO_4$), organics (OA), dust (DU) and sea-salt (SS) of $PM_1$ particles for the period 2011-2015. The median of all models is shown with blue bold line, while the shaded areas depict the 25%/75 % quartiles of all data. The green-dashed lines show the min/max values of all models. Available observational data are also shown with black dashed-lines and dots. Observations are from Schmale et al. (2017). Note that SS is here derived from $Cl^-$ $PM_1$ measurements that underestimate the SS levels.

**Fig. S2.** Comparisons of the monthly mean observations of CCN at various supersaturation ratios, $N_{50}$, $N_{80}$, $N_{120}$ particle number concentrations, and sulphate ($SO_4$) and organic aerosol (OA) mass concentrations with the corresponding results of each model. Models are plotted with different colours as indicated in the figure legend. Observations (black circles) are from Schmale et al. (2017).

**Fig. S3.** Comparison between monthly averages of the cloud droplet properties from observations (black circles) and from the individual models (see figure legend for model identification). Figures are drawn per station and for two different updraft velocities (w=0.3 $ms^{-1}$ and w=0.6 $ms^{-1}$) marked on the y-axis. For each station and updraft velocity the five graphs show (as indicated in the *y*-axis label), the total number of particles Nt, the number of cloud droplets, $N_d$, the maximum supersaturation, $s_{max}$ (in %), the sensitivity of the $N_d$ to the total number of aerosol particles, $(\partial N_d/\partial N_a)$, and the sensitivity of the $N_d$ to the wind speed, $(\partial N_d/\partial w)$.

**Fig. S4.** Comparison between the persistence times derived from the observations (in black bars) and from the model results of $CCN_{0.2}$ during winter and summer for each station. Each pair of bars that follows corresponds to the predictions of each model for winter (left bar) and summer (right shaded bar), respectively. The white bars show the persistence times of the MMM. The persistence times derived from model simulations have been computed at the same time periods as those derived from the observations.

**Fig. S5.** (a) Comparison of the winter and summer persistence times of $CCN_{0.2}$ for Finokalia station calculated using observational data (black bars) and the results of TM4-ECPL model for the base simulation (red bars) and the sensitivity simulation assuming the same emission of carbonaceous aerosols with the base case but fewer particles of larger size (green bars). The pairs of columns show persistences first for winter and second for summer. In both simulations a log-normal distribution

for the size distribution of emitted particles with a geometric standard deviation σ=1.59 has been assumed/used. In the base simulation, the dry median diameters of the emitted particles coming from fossil fuel combustion and from vegetation fires are 30 nm and 80 nm, respectively, while in the sensitivity simulations all particles are emitted at 60 nm. Left bars are for winter and right shaded bars are for summer. (b) Autocorrelation function (ACF) of the $CCN_{0.2}$ for Finokalia station calculated for summer (continuous lines) and for winter (dashed lines). Lines in colors are for the bars. The large-lag standard deviation curves are also shown in the graphs. The persistence time is defined as the time that the large-lag standard error crosses the ACF curve (Schmale et al., 2018). (c) same as panel-b using the results of the sensitivity simulation. (d)-(f) same as the panel-a for Cabauw, Hyytiälä and Mace Head stations, respectively.

**Fig. S6.** Global surface distribution for the year 2011 of the $N_3$ number concentrations as computed by the fifteen models that participated in this study. At the top of each panel the maximum value of the $N_3$ simulated by the model is denoted. Units are number of particles.$cm^{-3}$.

**Fig. S7.** Same as Figure-S6 for $N_{50}$ number concentrations. Units are number of particles.$cm^{-3}$.

**Fig. S8.** Same as Figure-S6 for $N_{120}$ number concentrations. Units are number of particles.$cm^{-3}$.

**Fig. S9.** Same as Figure-S6 for $CCN_{0.2}$ number concentrations. Units are number of particles.$cm^{-3}$.

**Fig. S10.** Global surface distribution of the mass concentration of sulphate (SO4) of $PM_1$ particles as computed by all models. At the top of each map the maximum value of the SO4 is denoted. Units are μg-SO4.$m^{-3}$

**Fig. S11.** Same as Figure-S10 for OA. Units are μg-OA.$m^{-3}$

**Fig. S12.** Same as Figure-S10 for BC. Units are μg.$m^{-3}$.

**Fig. S13.** Same as Figure-S10 for SS. Units are μg.$m^{-3}$

**Fig. S14.** Same as Figure-S10 for DU. Units are μg.$m^{-3}$

**Fig. S15.** Global distributions of the annual multi-model median concentrations of the SO4, OA, BC, DU and SS (from top to bottom) for the year 2011 (left column) and the corresponding diversities (right column). Model diversities are calculated as the ratio of the standard deviation to the mean of the models.

**Fig. S16.** Monthly ensembles for the years 2011-2015 of the CCN number concentration for supersaturation 0.2 % ($CCN_{0.2}$), 0.1% ($CCN_{0.1}$), 0.7% ($CCN_{0.7}$) and 1.0% ($CCN_{1.0}$) when observational data are available for Finokalia, Cabauw and Vavihill.

**Fig. S17.** Mean $CCN_{0.2}$ as calculated from the observations and as computed from the daily MMM for the days with available observations. The stations have been ranked based on CCN0.2 observations in decreasing levels.

**Fig. S18**. Ratio of the model diversity of $N_3$ (Figure 10b) to that of $CCN_{0.2}$ (Figure 10f).